2017

Thermophilic Ferritin: Versatile Nanohost

Katherine Pulsipher
University of Pennsylvania, kpuls@sas.upenn.edu

Thermophilic Ferritin: Versatile Nanohost

Abstract
Thermophilic ferritin from Archaeoglobus fulgidus (AfFtn) is a 24meric, hollow, cage-like protein, whose native function is the oxidation, mineralization, and storage of iron. Unique among ferritins, its self-assembly is dependent on high ionic strength, reflecting the deep sea thermal vent environment where A. fulgidus is found. This ionic strength dependence can be used to encapsulate charged cargo within the AfFtn cavity. Its subunits self-assemble into tetrahedral symmetry, resulting in four, large (4.5 nm), triangular pores, not found in other ferritins. Due to its size (12 nm outer diameter, 8 nm inner diameter), self-assembly properties, and potential for both genetic and chemical modification, AfFtn is an ideal nanocontainer for a variety of cargo, including inorganic nanoparticles and proteins.

We have sought to better understand the self-assembly of AfFtn and its encapsulation of various cargo. Guided by computational analysis and through mutagenesis, we have investigated the role of electrostatics along the AfFtn trimeric interface in self-assembly. We have developed a series of single point mutants with increasingly favorable cage assembly. One specific mutation, E65R, has a dramatic effect on AfFtn, almost entirely preventing disassembly and enhancing thermal stability by 14 C. By using a novel graphene-based microelectrode, we have determined that AfFtn maintains its quaternary structure upon encapsulation of a gold nanoparticle, developing a new tool for investigating protein-nanomaterial interactions. We have also shown that AfFtn can be used to template seeded gold nanoparticle growth and have explored two often neglected factors in ferritin-nanoparticle templating: the charge of the gold salt used, and the size of the protein pores. Our results demonstrate that the open, porous structure of AfFtn allows more efficient particle growth than typical closed-pore ferritins. Finally, we have expanded the cargo uptake of AfFtn beyond nanoparticles to include proteins, encapsulating supercharged GFP. The AfFtn-cargo complexes developed here have application in catalysis, nanomaterials synthesis, and targeted delivery.

Degree Type
Dissertation

Degree Name
Doctor of Philosophy (PhD)

Graduate Group
Chemistry

First Advisor
Ivan J. Dmochowski

Keywords
Ferritin, Nano-bio interface, Self-assembly

Subject Categories
Chemistry

THERMOPHILIC FERRITIN: VERSATILE NANOHOST

Katherine W. Pulsipher

A DISSERTATION

in

Chemistry

Presented to the Faculties of the University of Pennsylvania

in

Partial Fulfillment of the Requirements for the

Degree of Doctor of Philosophy

2017

Supervisor of Dissertation

_____

Ivan J. Dmochowski

Professor of Chemistry

Graduate Group Chairperson

_____

Gary A. Molander, Hirschmann-Makineni Professor of Chemistry

Dissertation Committee

Christopher B. Murray, Richard Perry University Professor of Chemistry and Materials Science and Engineering
Donald H. Berry, Professor of Chemistry
Jeffery G. Saven, Professor of Chemistry

THERMOPHILIC FERRITIN: VERSATILE NANOHOST

To my dad, who 26 years ago dedicated his thesis in chemistry to two-year-old me.

ACKNOWLEDGMENTS

Looking back on the past nearly six years of my Ph.D., I am overwhelmed with gratitude for the many people who have helped me get to this point. First, I would like to thank my advisor, Professor Ivan J. Dmochowski for his mentoring and training throughout my graduate school experience. His advice and ideas have been essential in moving my projects forward and in helping me become a better scientist. I am also thankful for his help beyond the lab, in figuring out what to do post-graduate school and advocating for me professionally.

I would also like to thank my committee members, Professor Christopher Murray, Professor Jeffery Saven, and Professor Donald Berry. They have been a source of invaluable advice and suggestions throughout my Ph.D. training, and I have greatly appreciated their feedback. Because of their different scientific backgrounds and research expertise, they have helped me examine my research from different points of view, which has been extremely helpful.

I have been lucky to have great lab members throughout the duration of my Ph.D. I am grateful to all current members of the Dmochowski lab for their friendship and help, both scientific and personal: Teresa Rapp, Sean Yeldell, Benjamin Roose, Serge Zemerov, Linlin Yang, Joshua Bulos, Yannan Lin, and Zhuangyu Zhao. Benjamin did all of the crystallographic work in Chapter 2, which greatly strengthened that project. I am also grateful to many former members of the lab: Yanfei Wang, Jasmina Cheung-Lau, Brittany Riggle, and Katie Liao. Teresa and Yanfei have been especially good friends and provided much needed support throughout my Ph.D. I am also particularly grateful to Brittany for

her pep talks and advice near the end of graduate school. Jasmina was the graduate student who made me want to join the lab in the first place, and she was the one who taught me everything I know about ferritin. I will always be grateful for her mentoring and her way of making me feel instantly welcomed in lab. I am also grateful to other members of Team Ferritin: Joe Swift, whom I have never met but whose papers I have practically memorized as he did much of the foundational work for my project, and Jennifer Yoon who contributed greatly in refining our ferroxidase assay in Chapter 2.

I have been lucky to work with many talented undergrads. I am thankful to Tacey Hicks, who only spent one summer on Team Ferritin as part of an REU, but who made major progress in getting the mutant ferritins project off the ground, which forms a large part of my thesis. Stephanie Honig was on Team Ferritin for most of her undergraduate career, and she was immensely helpful in doing everything and anything I asked of her. I wish them both the best of luck in their future endeavors.

I am lucky to have had many wonderful collaborators. I am especially thankful to Jose Villegas from Dr. Jeffery Saven's lab from Penn Chemistry, for his computational support on the mutant ferritins project. Without him, this project would not exist. It has been a joy to work with Dr. Jinglei Ping from Dr. Charlie Johnson's lab in Penn Physics. I have loved working with Dr. Makan Khoshnejad and Dr. Vladimir Shuvaev from Dr. Vladimir Muzykantov's lab in Penn Medicine. Working with them has given me a chance to learn more about targeted delivery and the biology of inflammation. I am grateful to Yaoting Wu and Dr. Matteo Cargnello from Dr. Christopher Murray's lab in Penn Chemistry who have provided me with many high-quality nanomaterial samples over the years.

My entire Ph.D. I have been involved with Women in Chemistry and the Women in Chemistry Professional Advancement Committee. It has been a great experience, and I am thankful to everyone who has participated with me: Teresa Rapp, Yanfei Wang, Stan Najmr, Stella Chen, Benjamin Partridge, Dee Mukherjee, Katie Elbert, and Becky Wiles. I am especially grateful to Judith Currano, who has provided faculty support and invaluable connections and ideas for events. I am also thankful to instrumental members of Women in Chemistry who have helped me become a better leader myself and who have made significant contributions to the Chemistry Department: Lyndsay Leal, Claire Gober, Jessica Levin, and Kelsey VanGelder.

There are a number of people who keep things running in the Chemistry Department, and I am grateful to all of them for their help at various points in my graduate school experience: Dan Burke, Yvonne Kline, Candice Adams, Kristen Muscat, Andre Korchynsky, Cuong Nguyen, Ryan Kubanoff, and Jason Seta. I am grateful to the staff in the Penn Electron Microscopy Resource Laboratory for years of help and advice: Dewight Williams, Ray Meade, and Biao Zhu. Finally, I am thankful to Nano/Bio Interface Director of Programs Kristin Field, for all of her work in running the major outreach event NanoDay@Penn, which I have had the pleasure of participating in every year and running monthly professional development events that I have greatly enjoyed and have significantly enhanced my Ph.D. experience.

I want to thank the female science role models in my life who have helped me see this path as a possibility. My high school chemistry teacher Wendy Snow-with her bright lipstick in just about every shade of red-taught me that you can be unabashedly feminine and passionate about science. My college organic chemistry professor Dr. Jennifer Nielson

helped me see graduate school as a possibility, and it is because of her influence that I decided to get a Ph.D. I am grateful for her continued mentoring and friendship.

I am thankful to my family and friends for all the support they have given me. My parents have been a wonderful source of support my entire life, and I am especially grateful for their help during graduate school. They have always encouraged me to get as much education as possible and have continually supported me in my efforts to do so. I am grateful to my siblings Becky, Jeff, Jenny, and Abby for their friendship and support as well.

Finally, I am thankful to my husband, Aaron. He has borne the brunt of bad weeks (sometimes months) in the lab. He has always been there for me, and I could not have done it without him.

ABSTRACT

THERMOPHILIC FERRITIN: VERSATILE NANO HOST

Katherine W. Pulsipher

Ivan J. Dmochowski

Thermophilic ferritin from *Archaeoglobus fulgidus* (AfFtn) is a 24meric, hollow, cage-like protein, whose native function is the oxidation, mineralization, and storage of iron. Unique among ferritins, its self-assembly is dependent on high ionic strength, reflecting the deep sea thermal vent environment where *A. fulgidus* is found. This ionic strength dependence can be used to encapsulate charged cargo within the AfFtn cavity. Its subunits self-assemble into tetrahedral symmetry, resulting in four, large (4.5 nm), triangular pores, not found in other ferritins. Due to its size (12 nm outer diameter, 8 nm inner diameter), self-assembly properties, and potential for both genetic and chemical modification, AfFtn is an ideal nanocontainer for a variety of cargo, including inorganic nanoparticles and proteins.

We have sought to better understand the self-assembly of AfFtn and its encapsulation of various cargo. Guided by computational analysis and through mutagenesis, we have investigated the role of electrostatics along the AfFtn trimeric interface in self-assembly. We have developed a series of single point mutants with increasingly favorable cage assembly. One specific mutation, E65R, has a dramatic effect on AfFtn, almost entirely preventing disassembly and enhancing thermal stability by 14 °C. By using a novel graphene-based microelectrode, we have determined that AfFtn

maintains its quaternary structure upon encapsulation of a gold nanoparticle, developing a new tool for investigating protein-nanomaterial interactions. We have also shown that AfFtn can be used to template seeded gold nanoparticle growth and have explored two often neglected factors in ferritin-nanoparticle templating: the charge of the gold salt used, and the size of the protein pores. Our results demonstrate that the open, porous structure of AfFtn allows more efficient particle growth than typical closed-pore ferritins. Finally, we have expanded the cargo uptake of AfFtn beyond nanoparticles to include proteins, encapsulating supercharged GFP. The AfFtn-cargo complexes developed here have application in catalysis, nanomaterials synthesis, and targeted delivery.

TABLE OF CONTENTS

LIST OF TABLES

LIST OF ILLUSTRATIONS

CHAPTER 1: INTRODUCTION

CHAPTER 2: THERMOPHILIC FERRITIN 24MER ASSEMBLY AND NANOPARTICLE ENCAPSULATION MODULATED BY INTERDIMER ELECTROSTATIC REPULSION

CHAPTER 4: CONTROLLING GOLD NANOPARTICLE SEEDED GROWTH IN THERMOPHILIC FERRITIN PROTEIN TEMPLATES

CHAPTER 5: THERMOPHILIC FERRITIN ENCAPSULATION OF SUPERCHARGED GFP

CHAPTER 6: FUTURE DIRECTIONS AND FINAL REMARKS

APPENDIX: FERRITIN ENCAPSULATION OF QUANTUM DOTS

CHAPTER 1: INTRODUCTION

Material in this chapter was originally published in the *Israel Journal of Chemistry*. It has been adapted here with permission from the publisher:

Reprinted with permission from Pulsipher, K.W.; Dmochowski, I.J. Ferritin: Versatile Host, Nanoreactor, and Delivery Agent. *Isr. J. Chem.* **2016**, *56*, 660–670.

1.1 Protein Nanocontainers

Biology is replete with small compartments, from whole cells to organelles, membrane vesicles, biomolecular complexes and active sites comprised of DNA, RNA or protein. Compartmentalization allows many chemical reactions necessary for life to occur simultaneously, without interference from other compounds. In addition to sequestering reagents for specific reactions, multi-subunit protein assemblies are capable of encapsulating useful cargo. The most well-studied examples of protein nanocontainers are viruses, which consist of a protein capsid shell and a nucleic acid cargo. Other examples include chaperone and heat shock proteins, which form hollow cages and play a role in protein folding. Ferritins are other natural compartments, whose hollow cavities can be filled with iron oxide (i.e., rust) and are responsible for helping maintain iron homeostasis.

Natural protein nanocontainers can be re-purposed and filled with unnatural cargo for a variety of applications. Virus capsids have been shown to self-assemble around gold,[1–5] iron oxide,[6] and semiconducting[7] nanoparticles (NPs) of various sizes, replacing DNA or RNA. Different final capsid geometries can form depending on the size of the NP used.[2] Proteins themselves can also be encapsulated within a protein container. One example is the cage-like lumazine synthase from *Aquifex aeolicus* (AaLS). Directed evolution was used to generate an AaLS variant with a highly negatively charged cavity interior, capable of self- assembling around highly positively charged cargo.[8] This mutant AaLS has been shown to encapsulate mutant superpositively charged GFP[9,10] and other proteins with a deca-arginine tag,[8,11] driven by electrostatic interactions. Functional enzymes can also be encapsulated such as carbonic anhydrase fused with a supercharged GFP analogue,[12] a supercharged variant of ferritin,[13] and a retro-aldolase fused with supercharged GFP.[14]

Ferritins, with outer diameter of 9-12 nm, are much smaller than viruses ($D \approx$ 30-50 nm) and AaLS ($D \approx$ 30 nm). Because of their natural role to interface with inorganic materials, ferritins have found wide use encasing inorganic NP cargos. The NP can be generated *in situ* in the ferritin cage, or the protein can be disassembled and reassembled around a NP of appropriate size and shape. Ferritins have also served as nanocontainers for a variety of small molecules,[15] including drugs[16–18] and fluorescent dyes.[19] Due to the relative ease of functionalizing proteins through genetic or chemical means, ferritin is an excellent delivery vehicle once a cargo is encapsulated. Their smaller size and lack of immunogenicity provide useful alternatives to virus capsids and AaLS.

1.2 The Ferritin Family of Proteins

Ferritins consist of multi-subunit, hollow, cage-like protein assemblies whose primary function is the oxidation and storage of iron. Ferric ion in water is scarcely soluble ($[Fe^{3+}] = 10^{-18}$ M at pH 7), whereas iron oxide can be encapsulated within the ferritin shell at molar concentrations. The importance of ferritins is highlighted by their ubiquity; all living organisms save for a handful of archaea express some form of the protein.[20] Ferritins can be split into two categories: 1) 24-subunit maxi-ferritins, found in prokaryotes and eukaryotes, and 2) 12-subunit mini-ferritins (DNA binding protein from starved cells, Dps), found only in prokaryotes. Maxi-ferritins can be further split into two groups: those that contain heme (found only in bacteria and known as bacterioferritins), and those that do not. Several examples of different ferritins are shown in Figure 1.1. Although sequence homology is low for most species of ferritin, their subunit structure is highly conserved: four α-helix bundles with an additional short fifth α-helix. Even without high sequence

homology, ferritin subunits of different species are sufficiently compatible to assemble and form heterocages similar to single-species cages.[21] With an outer diameter of approximately 12 nm and an inner diameter of 8 nm, maxi-ferritins can hold up to ~4500 Fe atoms.[20,22,23] Ferritin with an iron core is known as holoferritin, while ferritin with its core removed is known as apoferritin. Mammalian ferritins, such as human ferritin (HuFtn) and horse spleen ferritin (HSF), have two different subunits called H (heavy) and L (light), owing to the different weights of their monomers (21 vs 19 kDa). The two different chains are compatible and can self-assemble to form a heterocage. HSF (or its apo form, HSAF) is one of the most widely used ferritins because it is commercially available and relatively inexpensive. It is comprised of mostly L ferritin.[24] *Pyrococcus furiosus* ferritin (PfFtn) has received much attention due to its extremely high melting temperature,[25] since its preliminary structural analysis[26] in 2005 and complete crystal structure[27] was published in 2007. Most maxi-ferritins have a melting temperature of approximately 80 °C, while PfFtn has a T_m of over 120 °C. This makes it amenable for use in high-temperature reactions or experiments, which can be useful for preparing nanomaterials within the ferritin cavity.

Mini-ferritins have 12 subunits,[28,29] arranged in tetrahedral (32) symmetry with an outer diameter of 9 nm and inner diameter of 4.5 nm. While Dps can hold up to ~500 Fe atoms, it finds additional function in protecting organisms from oxidative damage.[29] It is

overexpressed in cells under oxidative or nutritional stress and binds DNA non-specifically to protect it.[30,31]

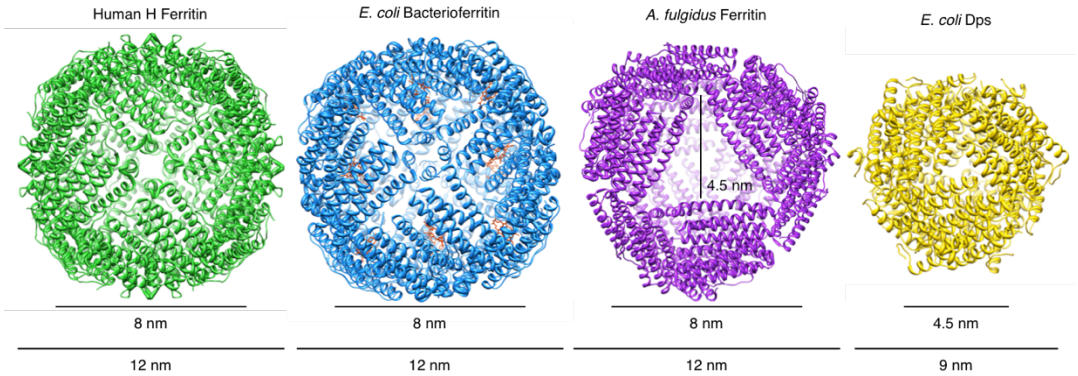

Figure 1.1. Representative examples of different types of ferritins. PDB codes (L to R): 2FHA, 1BFR, 1SQ3, 1DPS. The first three on the left are maxi-ferritins, of eukaryotic, bacterial, and archaeal origin. The heme groups of bacterioferritin are shown in orange. Mini-ferritin Dps is on the far right. Inner and outer diameters are listed below each ferritin. *A. fulgidus* ferritin and Dps have tetrahedral symmetry, with one of the 3-fold axes shown. *A. fulgidus* also features uniquely large triangular pores, not yet observed in any other ferritin. Human H ferritin and bacterioferritin have octahedral symmetry, with one of the 4-fold axes shown. Reproduced with permission from Ref. 32.

1.3 Ferritin Self-Assembly

Several studies have attempted to understand the ferritin self-assembly process from monomers into the 24mer cage. An early report using covalent crosslinking experiments suggested assembly intermediates of dimers (largest population), trimers, hexamers (smallest population), and dodecamers, with the assembly rate dependent on the protein concentration.[32] The proposed mechanism is shown in Equation 1.1:

$$24m_1 \rightarrow 24M_1 \rightleftharpoons 8M_1 + 8M_2 \rightleftharpoons 8M_3 \rightleftharpoons 4M_6 \rightleftharpoons 2M_{12} \rightarrow M_{24} \qquad (1.1)$$

where m_1 and M_1 denote the unfolded and folded monomers, respectively, and other subscripts denote the number of subunits per oligomer. Further studies using reversible dissociation with 2,3-dimethylmaleic anhydride showed that the trimer is less stable than the dimer in solution and that the hexamer rapidly forms the dodecamer.[33]

More recently, ferritin self-assembly has recently been probed using time-resolved small angle X-ray scattering (TR-SAXS).[34] Starting with *E. coli* ferritin A at low pH, assembly was induced by raising the solution pH and monitored by TR-SAXS. The data were mostly consistent with the second-order assembly mechanism proposed above, with multiple intermediates including a large population of dimers, hexamers, and dodecamers, and a small population of tetramers. Rather than a sequential addition of individual subunits up to the assembled 24mer, individual subunits form dimers, which then form higher order oligomers that associate with each other (Figure 1.2). This mechanism avoids falling into a kinetic trap where assembly is started too many times and therefore not enough single subunits are available to complete the 24mers. Ferritin assembly thus differs from assembly of viral capsids, which follow a nucleation growth mechanism.[35,36]

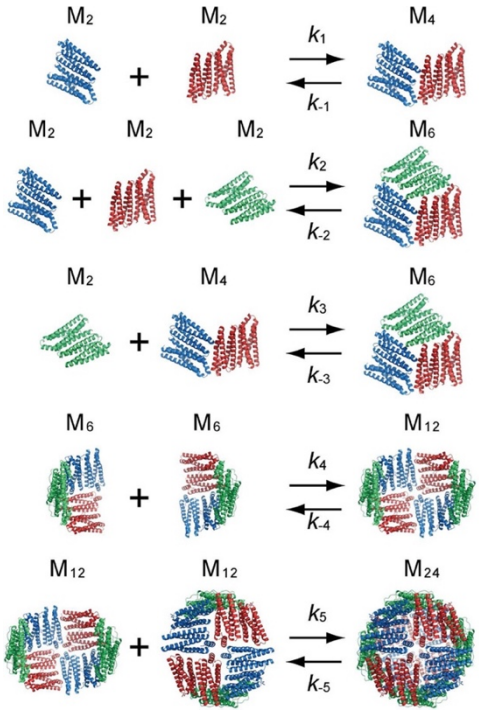

Figure 1.2. Ferritin self-assembly mechanism following association of oligomers. Reproduced with permission from Ref. 35. This is an unofficial adaptation of an article that appeared in an ACS publication. ACS has not endorsed the content of this adaptation or the context of its use.

Mutagenesis studies have explored what structural features are important for ferritin self-assembly. Orner et al. identified several "hot spot" residues in Dps and *E. coli* bacterioferritin whose mutation either shut down assembly entirely[37,38] or stabilized it.[39,40] They accomplished this by modulating hydrophobic interactions, either by plugging water pockets with aromatic amino acids,[39,40] by disrupting electrostatics along the dimer interface,[38] or by replacing amino acids with alanine.[37,41] In *E. coli* ferritin A, single point muations to alanine at the 3-fold axes decreased 24mer cage stability.[42] Similarly, Theil et al. prevented assembly of bullfrog ferritin cages by inserting positively charged amino acids in the loop region of each subunit, leading to repulsion of like charges.[43] More extensive modification involving cleavage of the last 23 amino acids in the monomer polypeptide chain enabled changes in the pH-dependent self-assembly of human H ferritin.[44]

1.4 Ferritin Encapsulation Strategies

Because of their size and robust self-assembly, ferritins are an excellent choice as a natural nano-sized container. The pores leading through the protein shell in most ferritins are quite small (<1 nm), so loading cargo within the apoprotein often requires disassembly and reassembly with the desired cargo in solution. Several methods for triggering self-assembly are shown in Figure 1.3. Maxi-ferritin self-assembly is typically governed by pH.[15,45] Certain species of Dps have also been reported with pH-sensitive assembly, including *Listeria innocua*[46] and *Mycobacterium smegmatis*.[47] While relatively simple, this assembly mechanism requires repeated transitions through the pI of ferritin, which can be damaging.[45]

Another assembly strategy involves a redesigned human ferritin that assembles only in the presence of copper ions.[48] By altering the *C2* interface between subunits to accommodate Cu(II) coordination, followed by destruction of native assembly stabilization contacts, Huard et al. formed a ferritin cage whose assembly is dependent on metal ions. Interestingly, the cage remained assembled, even after removal of copper, demonstrating the cooperative and stable nature of the protein quaternary structure.

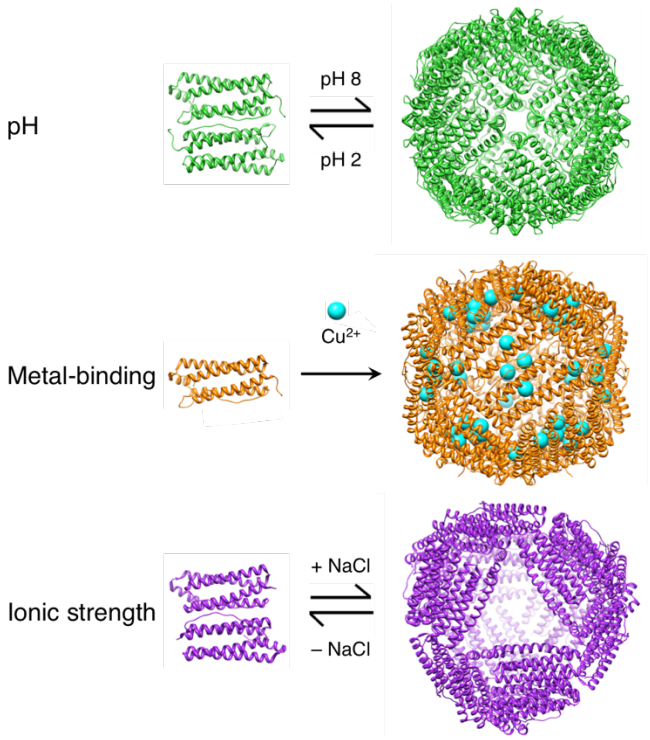

Figure 1.3. Methods for triggering ferritin self-assembly. From top to bottom (PDB): HuHFtn (2FHA), redesigned Cu-binding HuHFtn (4DYY), and AfFtn (1SQ3). Most mammalian ferritins, including HuHFtn shown, will disassemble and reassemble reversibly at acidic and mildly basic pH, respectively. HuHFtn was redesigned to only assemble in the presence of copper (blue spheres). The assembly was found to be irreversible, even when Cu^{2+} was removed. In AfFtn, assembly can be induced by increased ionic strength, and reversed by decreased ionic strength. Reproduced with permission from Ref. 32.

One species of ferritin exhibits unique ionic strength-dependent self-assembly, in addition to pH-mediated assembly. Thermophilic ferritin from the hyperthermophilic archaeon *Archaeoglobus fulgidus* (AfFtn) disassembles in solutions of low ionic strength,

and reassembles in solutions of high ionic strength.[49] This is presumably due to negatively charged residues residing at subunit interfaces, with electrostatic repulsion preventing assembly unless there are ions to screen the charges. Structurally, AfFtn is also unique because it has tetrahedral symmetry rather than the octahedral symmetry typical of other maxi-ferritins. Because of the tetrahedral arrangement of its subunits, there are four large (4.5 nm tip to opposite side) triangular pores in the 24mer cage, which have not been observed for other ferritins. Encapsulating a highly charged cargo, such as a gold nanoparticle (AuNP), can be done without adjusting the ionic strength of the solution.[50–52] This enables specific assembly induced by the cargo itself, leading to much higher encapsulation yields compared to other methods, which rely on serendipitously catching a cargo within the cavity.

1.5 Properties of Gold Nanoparticles

AuNPs are particles made of gold atoms with dimensions 1-100 nm. Although scientific interest in their preparation and properties has only been widespread within the last 50 years, AuNPs have been made for centuries, dating back to the Lycurgus cup in 4th century Rome,[53] and in medieval times when $AuCl_3$ salt was mixed with molten silica to form red cathedral stained glass windows. Michael Faraday was the first to scientifically investigate colloidal gold in the late 1800s,[54] and his remarkably stable AuNP samples can be seen today in the Faraday Museum at the Royal Institution in London. Because of their high surface energy caused by dangling surface bonds, NPs are prone to aggregation. To stabilize NPs in aqueous solution, "ligands" are adsorbed to the surface. These can be bulky polymers which stabilize against aggregation by sterics, or charged small molecules, which

stabilize particles through electrostatic repulsion. When gold particles are on the nanoscale, their optical properties change dramatically, with size, shape, surface ligand and assembly state playing significant roles.[55] Their optical properties can be attributed to surface plasmon resonance, the collective oscillation of electrons in the conduction band.[55] The frequency of this oscillation is usually in the visible range, giving AuNPs their brilliant red to purple color. The enhanced electromagnetic field on the surface of the NPs can lead to enhancement of Raman signal or fluorescence of molecules adsorbed on the surface,[56,57] making AuNPs highly useful in sensing[58] and imaging.[59] AuNPs are also capable of converting energy from incident NIR light into heat, which can be applied in photothermal therapy.[60] In addition to their many applications, AuNP synthesis is well-established and samples of high monodispersity can be made reproducibly. Thus, much of the work throughout this thesis will focus on AuNPs.

1.6 The Protein-Nanoparticle Corona

Because of their unique optical, magnetic, and chemical properties, NPs can be highly useful in medicine and biology, as improved imaging agents,[61] diagnostic sensors,[62] and therapeutics.[63] Multifunctional NPs create the possibility to combine therapeutic and diagnostic capabilities within the same "theranostic" particle. However, it is problematic that when NPs enter a complex biological fluid containing many proteins, such as serum, a protein "corona" forms at the NP surface.[64,65] This is driven by the high surface energy of nanoparticles, with adsorption of proteins lowering their surface energy and helping to maintain a stable dispersion. Proteins that adsorb weakly to the surface show faster exchange kinetics, called a "soft" corona, while proteins with higher affinity bind more

tightly with slower exchange times, forming a "hard" corona. Thus, when an inorganic NP is introduced into a biological medium, its core material and surface ligands are typically masked by the adsorbed proteins on the surface. This is an extremely important consideration when designing NPs for biological applications. As the NP passes through different organs or tissues, different proteins will be adsorbed/desorbed, manifesting the history of the NP in the proteins presented on its surface. This corona can change how the NP interacts with cells and may change where it localizes.[66] Understanding how proteins and NPs interact is therefore of vital importance so that NPs can be used for their intended purpose upon introduction into a biological system.

Adsorption to a NP surface can induce conformational changes in a protein. For example, polystyrene NPs induced decreases in α-helicity in apolipoprotein, human serum albumin, and lysozyme,[67] while denatured lysozyme, chymotrypsin, and papain were all refolded after adsorption on a AuNP surface.[68] Protein unfolding on NP surfaces can have significant consequences. When incubated with 90-nm AuNPs, lysozyme unfolded upon adsorption and induced NP aggregation.[69] In the presence of AuNPs capped with poly(acrylic acid), fibrinogen has been shown to unfold, displaying a normally buried binding epitope.[70] This enabled the interaction of fibrinogen with the integrin receptor Mac-1, which promotes an inflammatory response. When comparing 5-, 10-, and 20-nm particles, fibrinogen on 20-nm AuNPs did not interact with Mac-1, highlighting the importance of NP size. Trypsin was shown to unfold upon binding to polystyrene and silica NPs, causing a major loss of enzyme activity.[71] Proteins have also been shown to help stabilize NP dispersions.[72,73] Multiple factors including NP size/surface curvature,[74] surface ligands/charge,[75] and shape/crystal facet[76,77] can affect its interactions with

proteins. In general, highly charged NPs tend to adsorb proteins more strongly, while neutral NPs, especially those capped with high-molecular weight polyethylene glycol (PEG), minimize protein corona formation.[78–80] Improved understanding and control over how NPs and proteins interact will enable their more effective use in biological applications.

1.7 Ferritin-Nanoparticle Interactions

Through ferritin disassembly and reassembly, NPs (ligand shell included) smaller than the interior diameter of ferritin can be encapsulated. This is generally done using pH control over the assembly process. One example is the encapsulation of CeO_2 NPs within pig spleen ferritin.[81] The resulting ferritin-CeO_2 "nano-truffle" exhibited significant antioxidant activity, due to electron shuttling between Ce(III) and Ce(IV). The activity of the ferritin-CeO_2 was higher than CeO_2 NPs alone, due to charge transfer between ferritin and the NP. pH disassembly/reassembly was also used to encapsulate hybrid melanin/iron NPs within HSAF for magnetic resonance and photoacoustic imaging applications.[82]

In contrast to the pH-dependent disassembly, AfFtn has been shown to disassemble in low-salt conditions and reassemble around pre-formed AuNPs, without increasing the solution ionic strength.[50–52] A thermocycling method (50 cycles of 4 to 50 °C) was used initially to encapsulate 10-nm AuNPs capped with citrate, glutathione, bis(*p*-sulfonatophenyl(phenylphosphine)) (BSPP), or 4-dimethylaminopyridine.[50] Encapsulation was found to be nearly quantitative as confirmed by transmission electron microscopy (TEM), regardless of surface ligand. However, the α-helicity of the protein was significantly decreased after the encapsulation process. The thermal unfolding of AfFtn is

not reversible, so it is unsurprising that the repeated extreme changes in temperature led to partial denaturation.

Shown in Figure 1.4, a gentler encapsulation method was presented by Cheung-Lau et al.[51] 5-nm AuNPs coated with BSPP were encapsulated after 48 h with gentle agitation at room temperature. The resulting AfFtn-NP conjugates maintained the secondary structure, stoichiometry, thermal stability, and overall diameter of the native protein. This suggests a soft, non-perturbative interaction between the protein and NP, which is very different from the hard corona discussed above. The AfFtn-NPs were more stable to salt precipitation compared to "bare" particles. The assembly was found to be reversible; upon addition of excess salt, the NPs could be precipitated, recovering AfFtn with full ferroxidase activity. The lack of significant protein denaturation is notable and opens the AfFtn-NP conjugate to further use. Because spherical NP surfaces are relatively isotropic, it is difficult to functionalize them with spatial or stoichiometric specificity. Having AfFtn self-assembled in its native state around an NP gives a specific number of amino acid side-chain functional groups in precisely defined locations. This could be useful in attaching antibodies or other targeting ligands, where control over the number and/or spacing of ligands is important. As the primary interaction between the NP and AfFtn is with the surface ligands, this encapsulation method should be generalizable to NPs of any composition, so long as a suitable ligand is chosen.

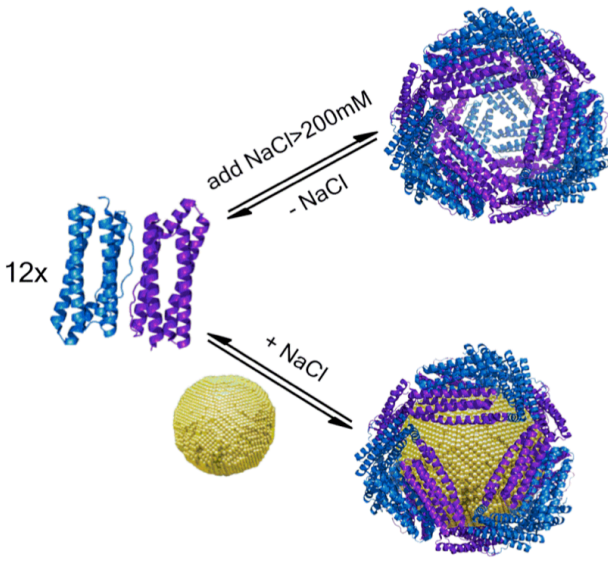

Figure 1.4. AuNP encapsulation by AfFtn. Decreasing the ionic strength of the solution causes cage disassembly. Addition of AuNPs of comparable size to the AfFtn interior diameter induces protein reassembly, with a stable conjugate formed by 48 h at room temperature with gentle rocking. The process is reversible, with addition of excess salt precipitating the NPs and leaving native protein in solution. Reproduced with permission from Ref. 52.

1.8 Targeted Ferritin Delivery

Encapsulating cargo within ferritin is useful for fundamental understanding of protein-nanoparticle interactions. However, to move beyond basic science and into biomedical applications, delivery of the ferritin-cargo conjugate is necessary. Delivery of therapeutics directly to where they are needed in the body will greatly improve drug efficacy, lower dosages, and decrease side effects, especially for toxic treatments such as chemotherapy in cancer. It can be challenging to append targeting moieties (folate, peptides, antibodies, etc.) to small molecule drugs or biologics without altering their activity. Rather than directly tagging the drug itself, drugs can be placed within a tagged carrier to direct them to a specific site. With its biocompatibility and ease of functionalization, ferritin is an excellent delivery vehicle in the oft-neglected 10-20 nm particle size range.

Different ferritins have intrinsic targeting capabilities due to their uptake by specific receptors. Human H ferritin binds transferrin receptor 1 (TfR1) and can be internalized into cells through this pathway,[83] while human L ferritin is taken up by the Scara5 receptor.[84] Uptake of HSAF in human intestinal cells was also shown to be receptor-mediated.[85] Delivery of neural drugs carbachol and atropine to treat pancreatic cancer in mice was achieved using human H ferritin.[86] Gefitinib (an epidermal growth factor receptor tyrosine kinase inhibitor) was also delivered this way,[16] as was methylene blue, a photosensitizer.[18] Inorganic nanoparticles have also been delivered through the natural targeting of ferritin. Pt NPs encapsulated within were specifically delivered to human intestinal Caco-2 cells for the purpose of decreasing oxidative stress.[87] Cells treated with the ferritin-NPs had significantly increased viability compared to controls when challenged with 5 mM H_2O_2.

It is also possible to redirect ferritin localization through conjugation of antibodies[88] or other targeting groups, such as peptides, to the ferritin surface.[89–92] Ferritin conjugated with RGD4C peptide enabled the delivery of doxorubicin to an U87MG subcutaneous tumor model, resulting in a longer circulation half-life, higher tumor uptake and tumor growth inhibition, and less cardiotoxicity than the free drug.[93] Genetic modification with an α-melanocyte-stimulating hormone peptide enabled ferritin targeting of melanoma cells.[94] Cobalt-doped magnetite NPs were encapsulated within the targeted ferritin for hyperthermia treatment. Melanoma cells exposed to the ferritin-Co/magnetite NP conjugates showed a 50% decrease in cell viability after treatment with an alternating magnetic field, while control cells remained alive.

We have recently explored targeting ferritin to the endothelium,[88] the single-cell layer lining the interior of blood and lymphatic vessels. Dysfunction in the endothelium is

linked to a number of diseases including hypertension, heart failure, diabetes, kidney failure, and atherosclerosis.[95] Problems with the pulmonary endothelium in particular are associated with acute respiratory distress syndrome, pulmonary hypertension, pulmonary embolism, and graft dysfunction after lung transplantation,[96] and targeting the pulmonary endothelium remains a challenge. The most commonly used clinical method for delivery to the lungs is inhalation, which is not always effective for therapeutics and may be especially problematic if lung activity is impaired. Recently developed strategies for pulmonary endothelium targeting include rod shaped polymeric particles,[97] spherical polymeric particles,[98] and liposomes,[99] all of which have dimensions larger than 100 nm. Delivery vehicle size can have a large effect on targeting efficiency, and less work has been done exploring pulmonary endothelium delivery with smaller particles. Ferritin provides a monodisperse, biocompatible sample with significantly smaller diameter compared to conventional delivery agents, along with relative ease of chemical or genetic modification.

To target the pulmonary endothelium, HSAF was chemically tagged with different targeting antibodies including anti-platelet cell adhesion molecule-1 (anti-PECAM-1) and anti-intercellular adhesion molecule-1 (anti-ICAM-1) through maleimide-sulfhydryl coupling. Maleimides were introduced in HSAF by use of lysine-reactive succinimidyl 4-(N-maleimidomethyl)cyclohexane-1-carboxylate (SMCC), and sulfhydryls were introduced in the antibodies using N-succinimidyl S-acetylthioacetate (SATA). Conjugation with single chain antibody fragments and whole antibodies was compared. As expected, fewer whole antibodies were attached to the ferritin surface, presumably due to greater steric hindrance compared to the fragments. The antibody-HSAF conjugates were found to bind specifically to cells expressing either ICAM-1 or PECAM-1, corresponding

to the particular antibody labeling. By conjugating HSAF with IgG, the natural TfR1 uptake pathway could be avoided, compared with unconjugated HSAF, demonstrating re-direction of ferritin's native targeting. Biodistribution studies in mice showed that the antibody-targeted ferritins localized predominantly in the lungs, at percentages equal to or higher than other commonly used polymeric NPs or liposomes (Figure 1.5). These larger delivery agents have considerably more antibodies on their surface compared to HSAF, which makes this finding all the more surprising. We suspect that the comparable targeting efficiency of HSAF is due to how the antibodies are presented on the surface, making it easier to bind their targets, compared with polymeric NPs and liposomes. Current work is ongoing in our lab to load ferritin with therapeutic molecules and demonstrate their delivery *in vivo* and *in vitro.*

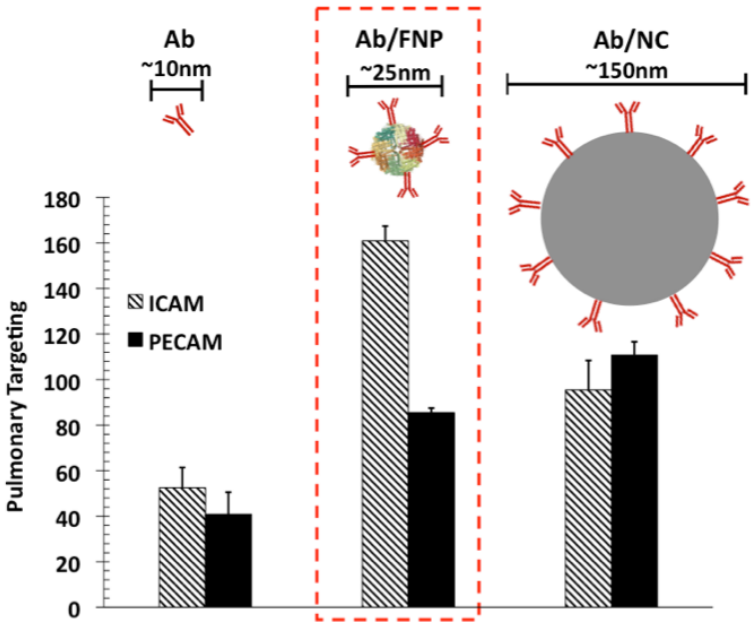

Figure 1.5. Antibody-ferritin conjugate (Ab/FNP) targeting pulmonary endothelium. Compared with free antibody (Ab) or antibody-polymeric NP (Ab/NP), Ab/FNP has greater or comparable targeting capability to either intercellular adhesion molecule (ICAM) or platelet endothelial cell adhesion molecule (PECAM). Reprinted with permission from Ref. 89. Copyright 2015 American Chemical Society.

The work presented in this thesis highlights the versatility of AfFtn in exploring its encapsulation capabilities. In Chapter 2, we report designed AfFtn mutants with altered assembly properties and how these changes affect their interactions with AuNPs. In Chapter 3, we demonstrate using both novel and conventional methods that AfFtn maintains its quaternary structure upon AuNP encapsulation, describing a new analytical technique for understanding protein-NP interactions. In Chapter 4 we explore AuNP seeded growth templating by AfFtn and the effect of the gold salt used, as well as the AfFtn pore size. In Chapter 5 we broaden AfFtn encapsulation beyond inorganic nanoparticles to proteins, using supercharged GFP(+36) as a proof-of-concept. In the Appendix we show preliminary data of AfFtn encapsulating quantum dots (QDs) and its effect on QD optical properties. From nanomaterials synthesis to therapeutic protein encapsulation, AfFtn is a highly useful nanocontainer with great potential.

CHAPTER 2: THERMOPHILIC FERRITIN 24MER ASSEMBLY AND NANOPARTICLE ENCAPSULATION MODULATED BY INTERDIMER ELECTROSTATIC REPULSION

The content of this chapter has been submitted for publication. It has been adapted here:

Reprinted with permission from Pulsipher, K.W.; Villegas, J.A.; Roose, B.W.; Hicks, T.L.; Yoon, J.; Saven, J.G.; Dmochowski, I.J. Thermophilic Ferritin 24mer Assembly and Nanoparticle Encapsulation Modulated by Interdimer Electrostatic Repulsion. **2017**. *Submitted.*

2.1 Introduction

Protein cages are large, multi-subunit structures with hollow interiors. Because of their size and unique structural properties, these cages are useful in many applications including bio-targeting,[88,100] drug delivery,[92,101] catalysis,[102,103] and nanoelectronics.[104] Ferritins make up a ubiquitous family of protein cages, important for iron storage in most organisms. Maxi-ferritins share a similar overall structure: 24 tetrahelical subunits, assembled to form a hollow, roughly spherical shape. Eukaryotic ferritins remain stably assembled as 24mers over a wide pH range.[105] Some prokaryotic ferritins exist as mixture of fully assembled 24mer and disassembled dimer.[106] The dimer is a common intermediate in ferritin self-assembly, and the 24mer/dimer distribution can be altered by single point mutations. Orner et al. identified several "hot spot" residues in *E. coli* bacterioferritin and ferritin-like DNA binding protein from starved cells (DPS) whose mutation either shut down assembly entirely[37,38] or stabilized it.[39,40] They accomplished this by modulating hydrophobic interactions, either by plugging water pockets with aromatic amino acids,[39,40] by disrupting electrostatics along the dimer interface,[38] or by replacing amino acids with alanine.[37,41] In *E. coli* ferritin A, single point mutations to alanine at the 3-fold axes decreased 24mer cage stability.[42] Similarly, Theil et al. prevented assembly of bullfrog ferritin cages by inserting positively charged amino acids in the loop region of each subunit, leading to repulsion of like charges.[43] More extensive modification involving cleavage of the last 23 amino acids in the monomer polypeptide chain enabled changes in the pH-dependent self-assembly of human H ferritin.[44] Human H ferritin was also redesigned to self-assemble only in the presence of copper ions.[48]

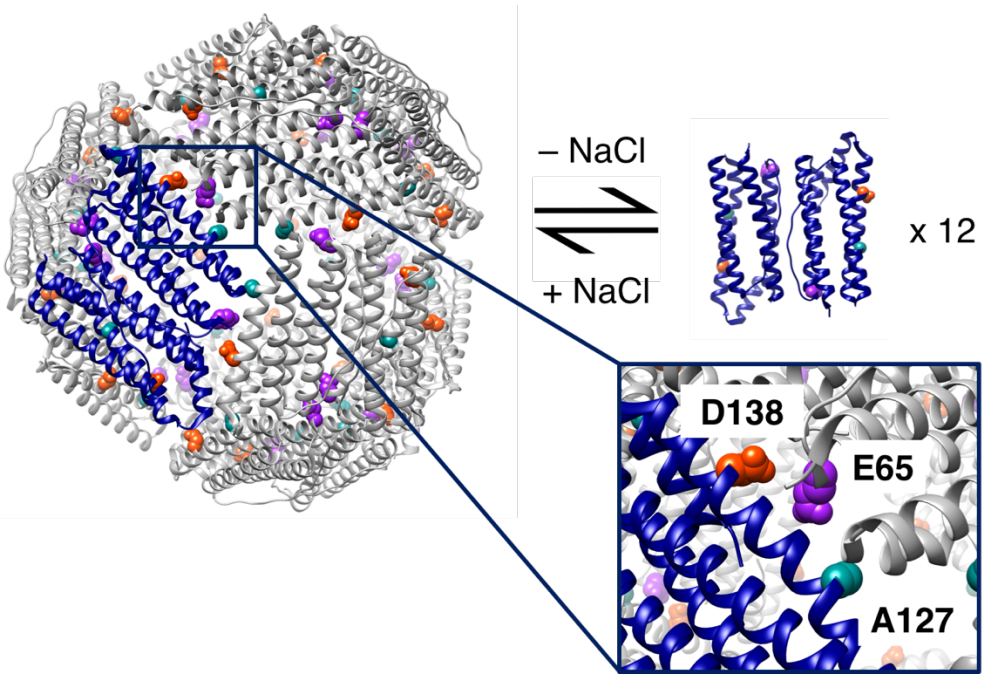

Figure 2.1. Salt-dependent assembly for wild type AfFtn. Under high-salt conditions (800 mM NaCl), the 24mer cage predominates. Under low-salt conditions (<200 mM NaCl), the protein disassembles into twelve dimers. The dimer is highlighted in blue in the 24mer cage on the left. Inset shows close up of mutation positions at the trimeric interface. The crystallographic structure of AfFtn (PDB ID: 1SQ3) was used to generate the figure.[49]

In this chapter, we investigate the self-assembly of thermophilic ferritin from the archaeon *Archaeoglobus fulgidus* (AfFtn), which has unique salt-dependent assembly, not-yet-found in other ferritins. Shown in Figure 2.1, at high ionic strength (800 mM NaCl), the 24mer is the dominant assembly state. At lower ionic strength (<200 mM NaCl), the protein disassembles into stable dimers, which we refer to herein as the protein subunits.[49,50] We have used the ionic strength-dependent self-assembly of AfFtn to encapsulate citrate- or BSPP-functionalized gold nanoparticles (AuNPs), rendering them more biocompatible and stable to salt-induced precipitation.[50–52] The encapsulation process happens under mild conditions, at room temperature with gentle agitation. The resulting AfFtn-AuNP assembly

maintains native protein secondary structure, subunit stoichiometry, melting temperature, and ferroxidase activity, thus highlighting unusual protein-AuNP complementarity.

The crystal structure of AfFtn (PDB ID: 1S3Q)[49] contains a trimeric interface rich in negatively charged residues. We hypothesized that electrostatic repulsion at this interface prevents subunit assembly at low ionic strength and neutral pH, given that the estimated pI of AfFtn is 4.7. Subunit-subunit electrostatic repulsion was found to be important in governing the rate of self-assembly of *E. coli* ferritin A, which typically exists only as a 24mer except in acidic conditions.[107] As other ferritins do not feature salt-mediated self-assembly, AfFtn provides a unique opportunity to investigate the role of subunit interface electrostatics in protein cage formation.

We hypothesized that decreasing electrostatic repulsion between anionic subunits by designed amino acid substitution should promote 24mer formation at low-salt concentrations. We tested this hypothesis by introducing positively charged groups at various positions along the dimer-dimer interface. As we have employed previously in the redesign of ferritin proteins,[108,109] a statistical computational design strategy was used to calculate theoretical amino acid probabilities at selected sites. The resulting probabilities were used to guide the selection of point mutations likely to be compatible with the overall protein structure as well as the supramolecular assembly. Three single-point mutants (shown in Figures 2.1 and 2.2) were experimentally characterized, where each mutation substituted a single negatively charged or neutral residue for a positively charged one. We investigated the thermal stability of the mutants and explored changes in the self-assembly equilibrium, kinetics, and reversibility at different salt concentrations. Finally, we tested

the capability of each mutant to encapsulate and stabilize AuNPs, as well as template further AuNP growth. We conclude that altering electrostatic interactions between ferritin subunits provides a versatile approach to modulating protein cage assembly.

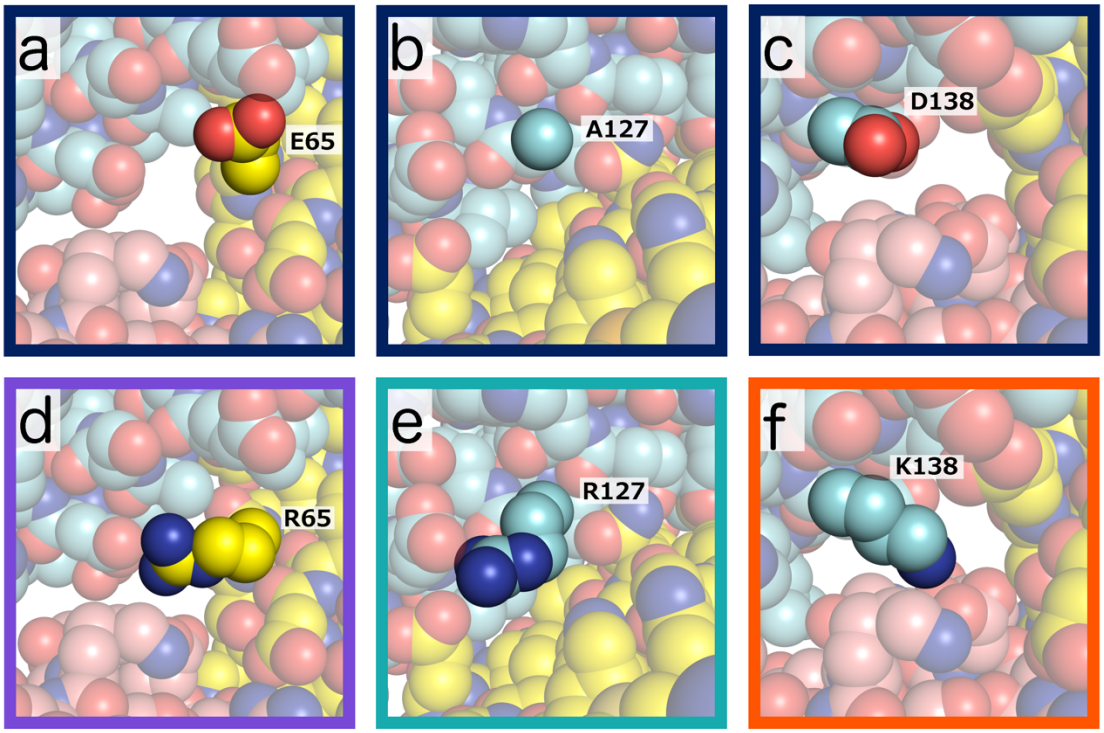

Figure 2.2. Computationally designed mutations along the trimeric interface. Wild-type residues (dark blue border): (a) E65, (b) A127, and (c) D138. Single-point mutations: (d) A127R (violet border), (e) D138K (teal border), and (f) E65R (orange border). Different protomers (chains) are rendered distinct colors: cyan, yellow and pink.

2.2 Results

Computational Design of AfFtn Mutants

In the design calculations, we sought to identify mutations that both introduce a positively charged residue and span the interface between adjacent protamers. We focused on the probabilities of amino acid type (a) at each site i, $P_i(a)$, or the ratio relative to the wild-type residue $P_i(a) / P_i(a_{wt})$. At site 34, the wild-type Asp was the most probable

residue, and as a result, this site was not selected for mutation. At site 65, Arg was the most probable amino acid (P_{65}(R) = 0.83), yielding the suggested mutation E65R. At site 127, Arg was the most probable amino acid (P_{127}(R) = 0.63), and the mutation A127R was selected. At site 131, Lys was the most probable amino acid P_{131}(K) = 0.93. Upon examining the resulting model structures, the conformations of this side chain directed the ammonium group within the protomer, and the side-chain interactions did not span an interface with other protomers; this site was not selected for mutation. At site 138, the four most probable amino acids were Arg, Asn, Asp, and Lys, and P_{138}(K)/ P_{138}(D) = 1.49. The mutation D138K was selected at this site.

General Protein Characterization

We prepared E65R, A127R, and D138K single point mutants using standard site-directed mutagenesis. After expression and purification, protein purity was verified by SDS-PAGE and UV-vis spectroscopy (Figures 2.3 and 2.4) and identity was verified by MALDI-TOF MS (Figure 2.5).

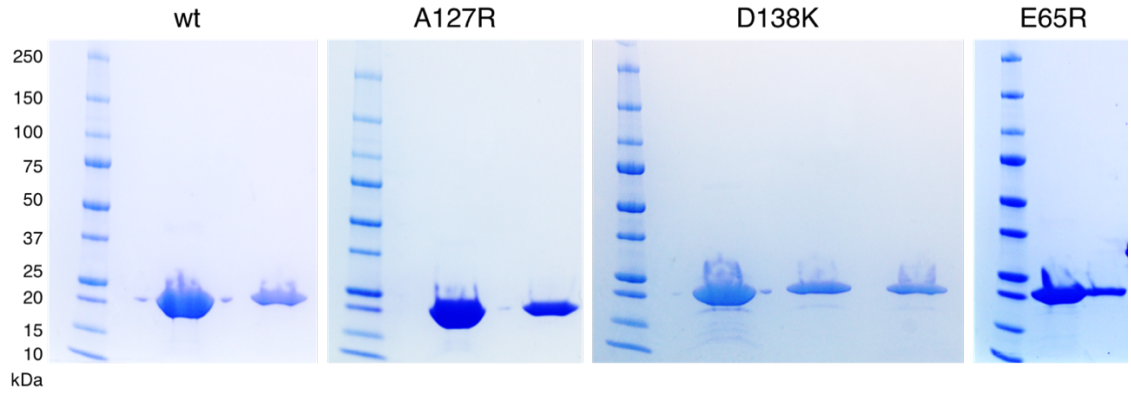

Figure 2.3. SDS-PAGE denaturing gels showing >90% purity for all proteins used and a monomer MW of approximately 20 kDa, as expected.

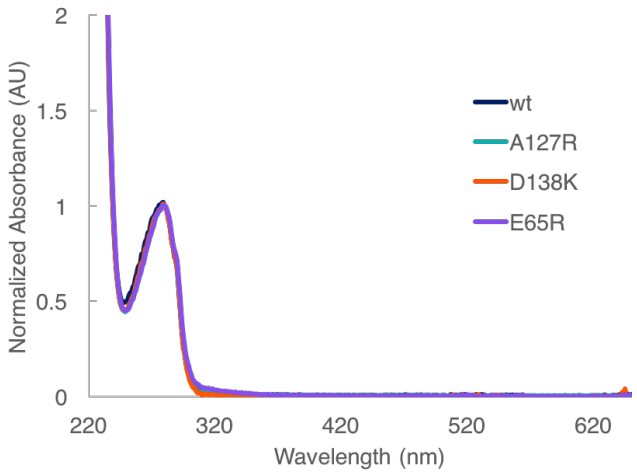

Figure 2.4. Normalized UV-vis spectra of purified proteins. No significant DNA contamination is observed.

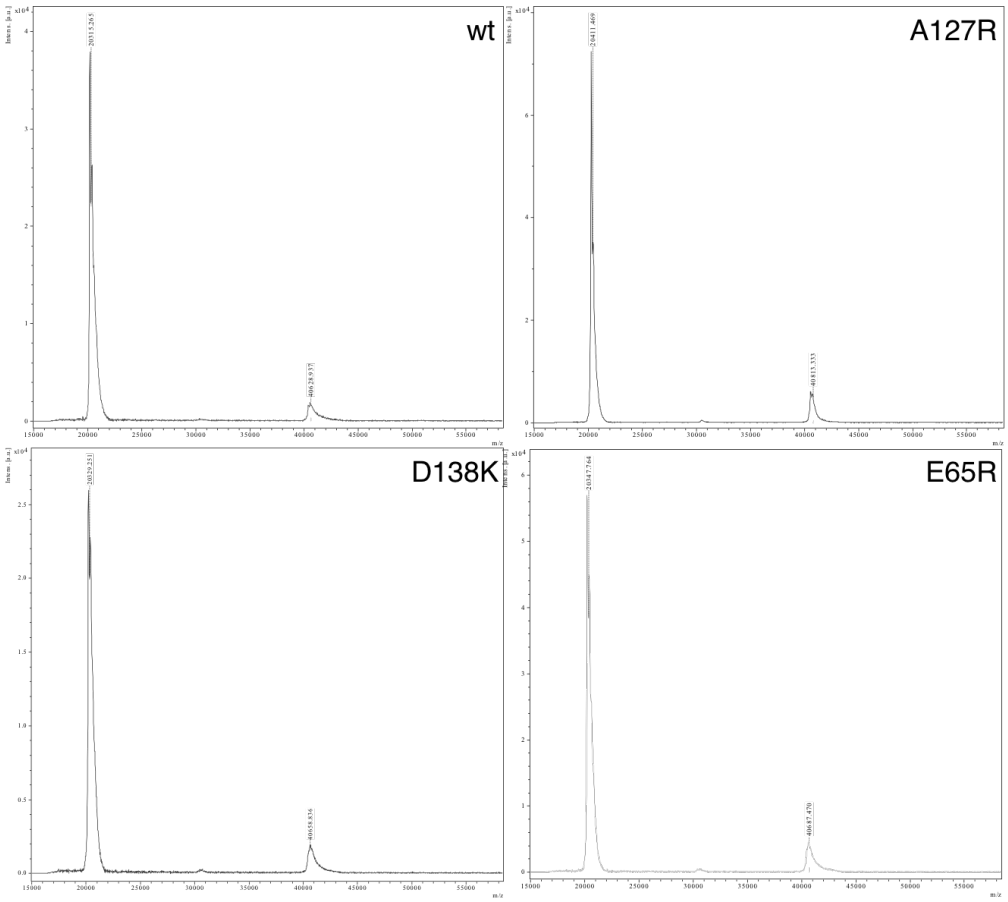

Figure 2.5. MALDI-TOF-MS for all proteins used. Measured mass for monomer (expected): wt 20315.3 (20316.1 Da), A127R 20411.5 (20401.2 Da), D138K 20329.3 (20329.2 Da), E65R 20347.8 (20343.1 Da). Peaks at ~40 kDa correspond to dimer. Sinapinic acid was used as a matrix, and linear-positive mode was used as the method.

We then verified cage formation in 800 mM NaCl by transmission electron microscopy (TEM). Shown in Figure 2.6 and summarized in Table 2.1, cages with approximately the same diameter as wild type (wt) were observed in TEM micrographs, showing the mutations did not inhibit self-assembly in high ionic strength solution. Dynamic light scattering (DLS) also showed similar results, with all mutants having average particle diameters within 2 nm of that of wt (D_{avg}(wt) = 13.5 nm). Circular dichroism (CD) spectra for all three mutants showed almost no change compared to wt, demonstrating a lack of perturbation in secondary structure (see Figure 2.7). This is unsurprising, as ferritins and ferritin-like proteins have been shown to be stable to extensive mutagenesis.[109]

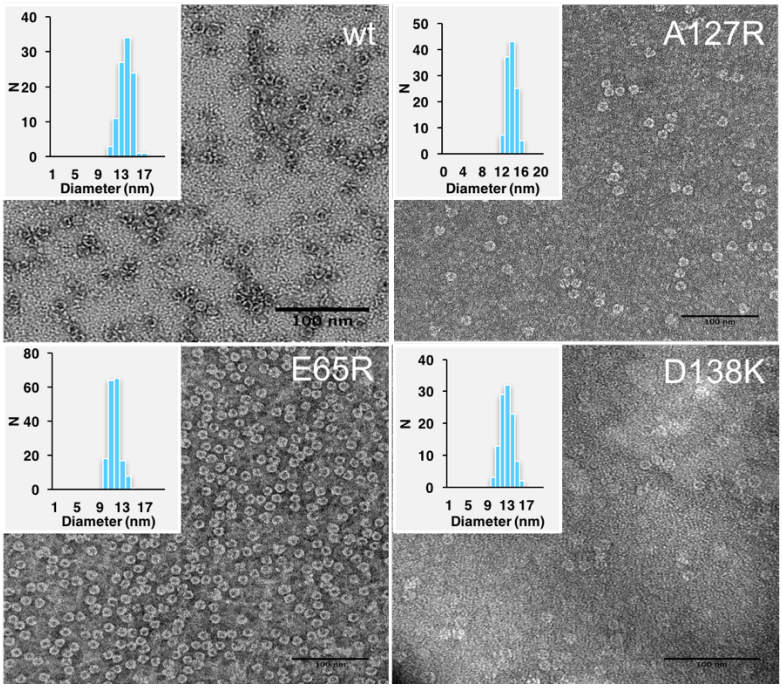

Figure 2.6. TEM micrographs and size distributions for wt and mutant AfFtn. Similar cage structures were observed for all samples, indicating mutations did not prevent self-assembly. Grids were stained with either 2% uranyl acetate or 2% ammonium molybdate negative stain. Particle size was measured manually using ImageJ.[110] Scale bars are 100 nm.

Table 2.1. Assembled cage characterization in 800 mM NaCl.

Sample	D_{avg} TEM (nm)[a]	N[b]	D_{avg} DLS (nm) [PDI]	T_m (°C) [c]
wt	13.2 ± 1.1	101	13.5 [0.035]	84
A127R	13.3 ± 0.9	117	13.6 [0.052]	85
D138K	12.3 ± 1.3	110	14.9 [0.103]	84
E65R	11.1 ± 0.9	173	12.9 [0.059]	98

[a] D_{avg} is average diameter.
[b] N is number of particles that were measured manually using ImageJ[111] to calculate average diameter.
[c] T_m was measured by CD for wt, A127R, D138K and by DSC for E65R.

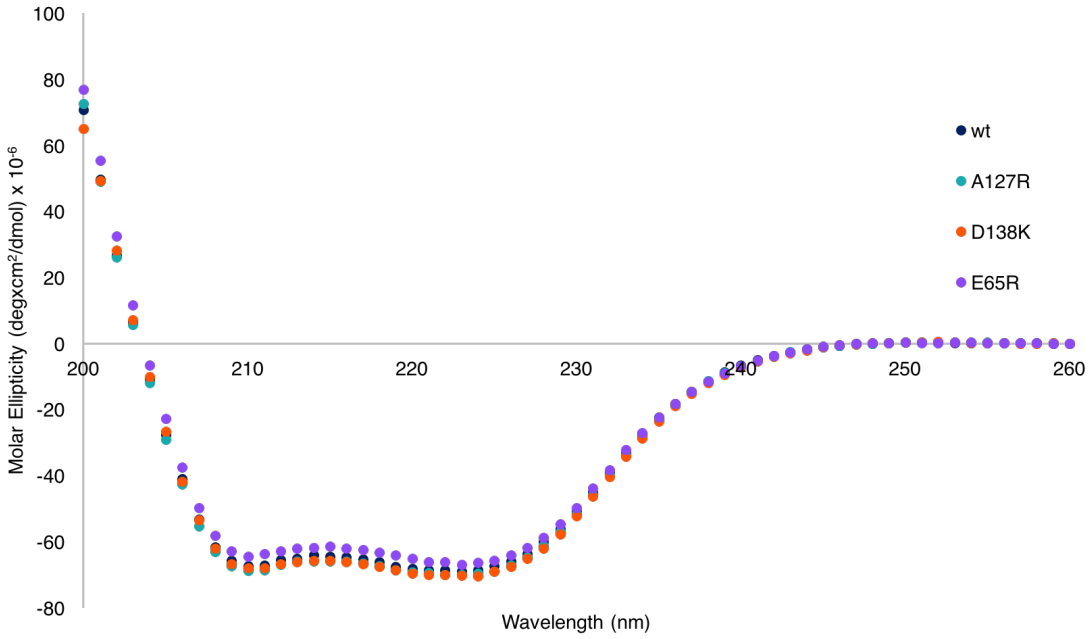

Figure 2.7. CD spectroscopy for wt and mutant AfFtn. Minimal changes in secondary structure are seen upon mutation. Sample concentration was 0.3 mg/mL in 800 mM NaCl, 20 mM phos, pH 7.6 buffer.

Next, we investigated the thermal stability of the mutants using CD spectroscopy (Figure 2.8a). Because CD spectroscopy monitors changes in secondary structure, our thermal stability data only provide information on the secondary structures of individual

four-helix bundle subunits. At 0.3 mg/mL, both A127R and D138K showed nearly identical thermal stability to wt AfFtn (T_m = 84 °C, Table 1). However, E65R did not unfold for T < 96 °C, and we were unable to measure its T_m by CD. Instead, we turned to differential scanning calorimetry (DSC), which uses a pressurized, sealed sample chamber, enabling us to measure higher melting temperatures in aqueous conditions. By DSC at 0.5 mg/mL, we measured a T_m = 98 °C for E65R; using the same technique, we measured T_m = 84 °C for wt, which confirmed the CD-determined values (Figure 2.8b). Remarkably, E65R has thermal stability enhanced by 14 °C compared to the hyperthermophilic wt protein and other two mutants.

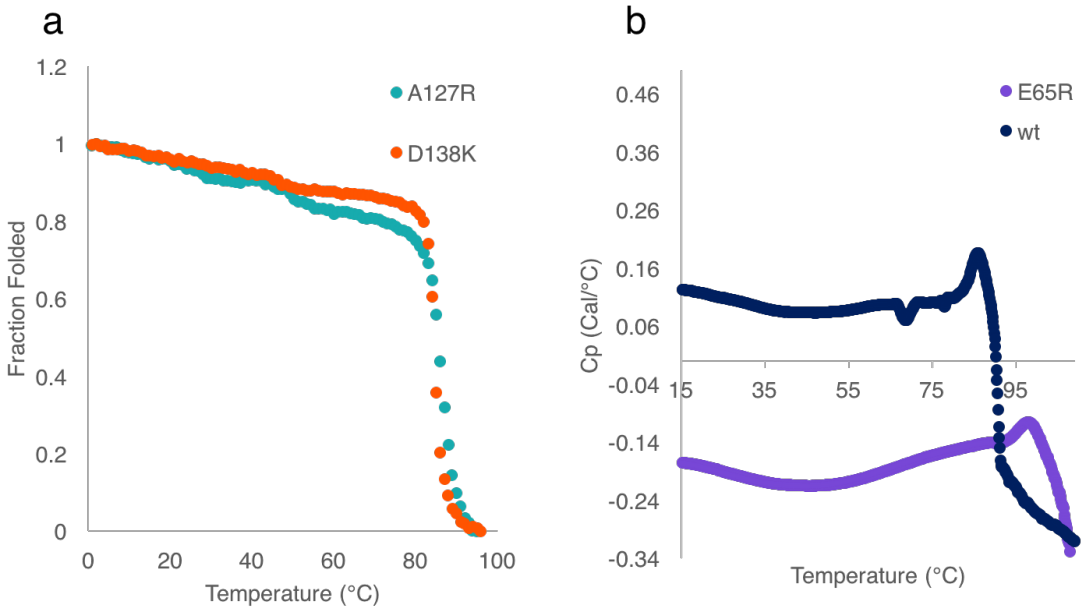

Figure 2.8. Thermal stability characterization of AfFtn mutants. a) CD spectroscopy was used to generate fraction folded plots for A127R and D138K. b) Differential scanning calorimetry traces for wt and E65R.

Shown in Figure 2.9, we also investigated the enzymatic activity of the mutants using an absorbance-based ferroxidase assay.[112] An aliquot with 480 eq of Fe^{2+} was added to each sample and oxidation to Fe^{3+} was monitored by the increase in iron mineral

absorbance at 315 nm. E65R had slightly enhanced activity compared to wt, while D138K had slightly diminished activity and A127R had significantly diminished activity. A127R is closest to the ferroxidase site of the protein and likely interacts with glutamates in positions 128 and 131, potentially perturbing their activity. In light of minimally affected structural features and thermal stability mentioned above, this represents a localized disruption of the ferroxidase site compared to wt AfFtn.

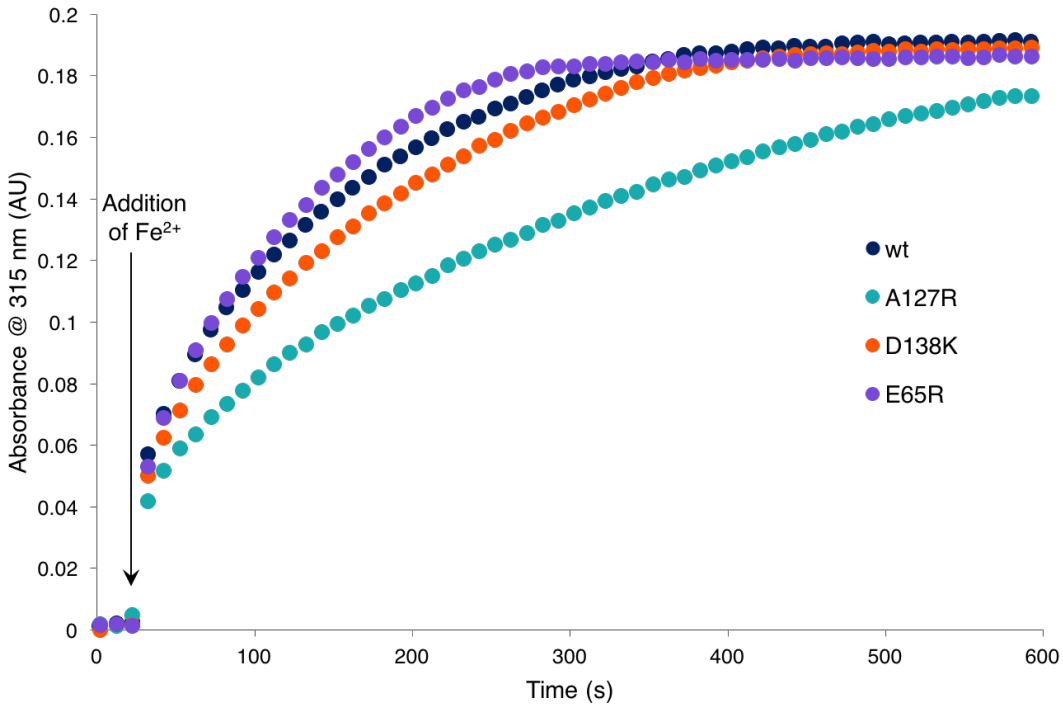

Figure 2.9. Ferroxidase activity of wt and mutant proteins. D138K and E65R show similar activity to wt, while A127R shows inhibited ferroxidase, indicating some perturbation to the ferroxidase site of the protein.

Self-assembly Equilibria

After general characterization of all mutants, we were interested in how mutagenesis affected the dimer-24mer equilibrium. To investigate the assembly state of

the proteins at varying salt concentrations, we used size exclusion chromatography (SEC), tryptophan fluorescence, DLS, and native gel electrophoresis.

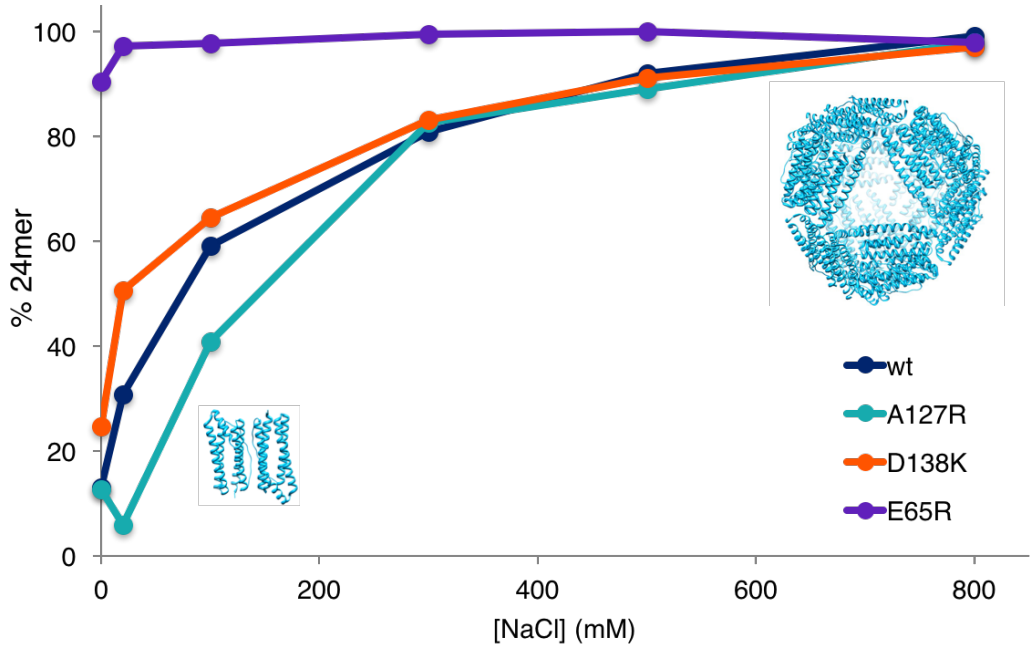

Figure 2.10. Size exclusion chromatography quantification of the amount of 24mer present at various salt concentrations for all proteins. Compared to wt (dark blue) at low salt concentrations, D138K has a slightly larger percentage of the fully formed assembly (orange), and A127R has a slightly larger percentage of the dimer (teal). E65R has greater than 90% assembly at all salt concentrations tested, [NaCl] = 0-800 mM (violet).

SEC was performed after incubating each mutant overnight at 5 mg/mL in solutions of different salt concentrations, as seen in Figure 2.10. The peak in the SEC trace at ~10 mL was attributed to 24mer, while the peak at ~14 mL was attributed to dimer (see Figure 2.11), based on column MW calibration.

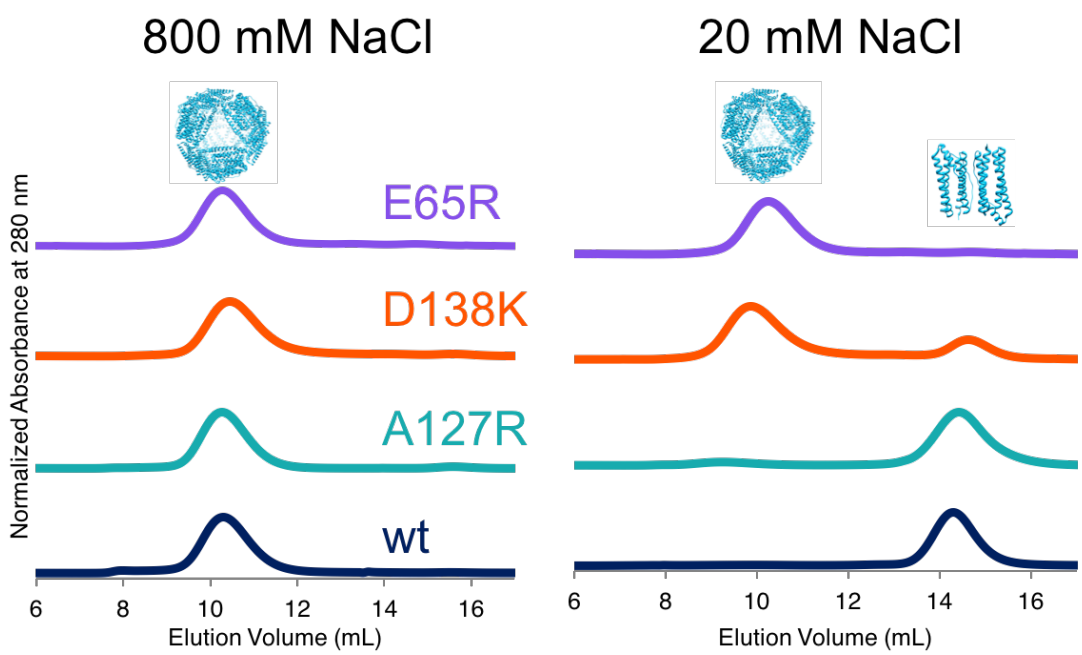

Figure 2.11. Representative size exclusion traces showing 24mer elution at ~10 mL and dimer elution at ~14 mL.

The area under the peaks was used to quantify the percentage 24mer for each protein at each salt concentration. As expected, at high-salt conditions ([NaCl] > 500 mM), all proteins showed nearly 100% 24mer. At lower salt conditions ([NaCl] < 200 mM), different behaviors were observed. A127R is slightly less likely to self-assemble in low-salt conditions compared to wt, while D138K has slightly higher propensity to assemble, with higher 24mer populations than wt at 0, 20, and 100 mM NaCl. E65R shows >90% 24mer under all salt conditions tested, demonstrating a dramatic change in self-assembly equilibrium.

To corroborate SEC results, we used Trp fluorescence, which is reflective of the solvation environment of Trp residues in the protein (Figure 2.12a). AfFtn contains four Trp residues per single-chain subunit, two of which are predicted to see some change in solvation upon disassembly (Trp44 and Trp124). For wt, in 800 mM NaCl buffer where

AfFtn is completely assembled, the Trp emission maximum is at 332 nm. In 0 mM NaCl buffer, where AfFtn is disassembled into dimers, the emission red shifts to 337 nm, consistent with the Trp residues becoming more solvent exposed. We measured the Trp fluorescence spectrum for each protein in 0 and 800 mM NaCl buffer. All of the mutants exhibited similar fluorescence spectra to wt at 800 mM NaCl, with similar peak shapes and maximum emission wavelengths. E65R showed a slight blue shift compared to wt, with an emission maximum of 331 nm compared to 332 nm for wt. At 0 mM NaCl, significant changes were observed. A127R and wt had the largest red shifts, moving to 337 and 338 nm, respectively, indicating disassembly for both proteins. D138K had a red shift of only 2 nm, while E65R only shifted by 1 nm. These trends for D138K and E65R match those observed by SEC, with E65R showing minimal structural changes with changing salt concentration, and D138K showing smaller changes than wt.

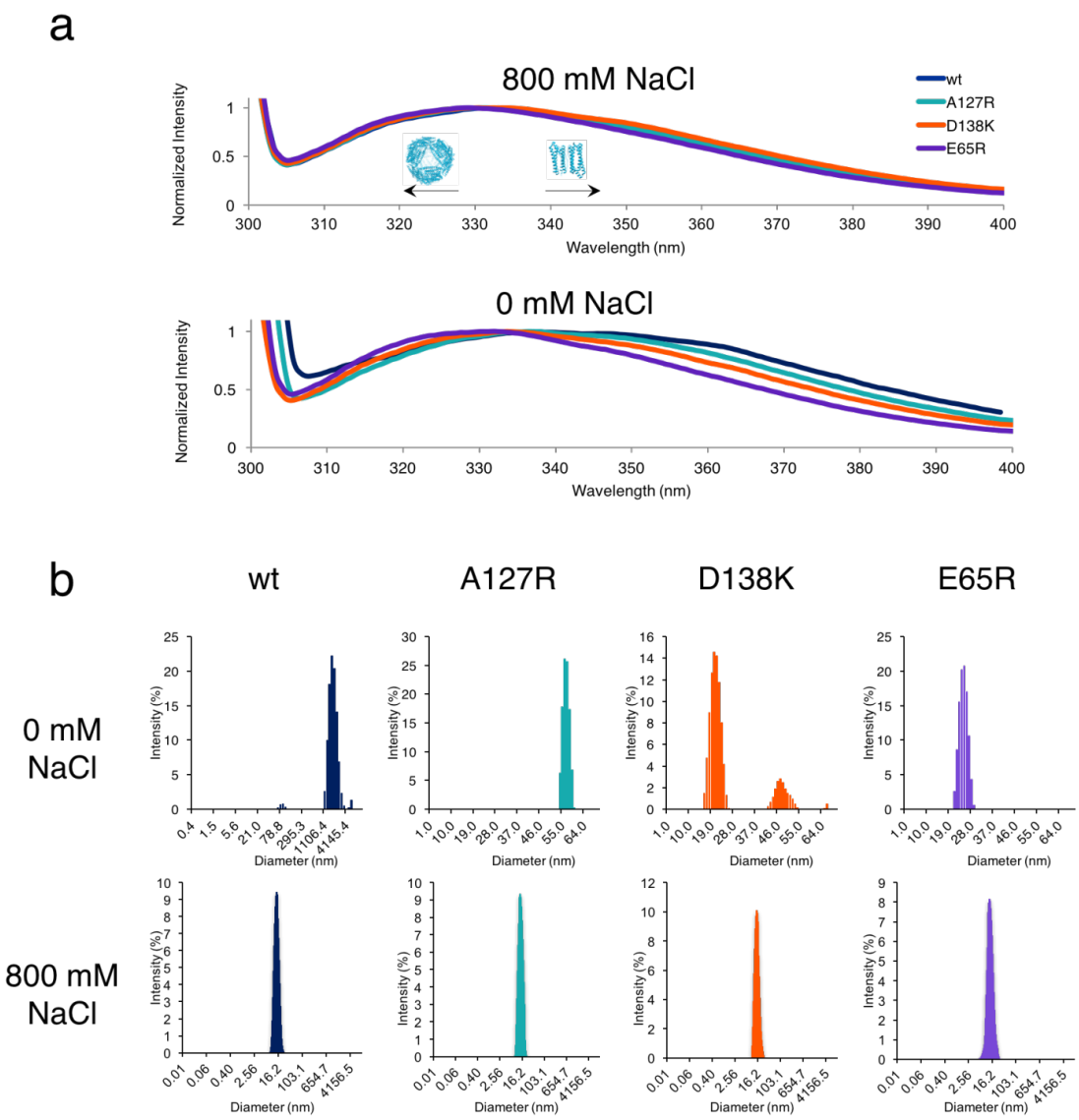

Figure 2.12. Additional size characterization of AfFtn mutants. a) Tryptophan fluorescence results for wt and mutants. b) Dynamic light scattering results. All proteins in 800 mM NaCl show complete 24mer assembly. At 0 mM NaCl, only E65R remains assembled, while D138K forms discrete dimers and some aggregate, and wt and A127R predominantly form aggregates of dimers.

DLS corroborated Trp fluorescence results showing A127R with similar self-assembly behavior to wt, E65R, and D138K, with increased 24mer population at low-salt conditions (Figure 2.12b). Like wt, A127R 24mer was present at 800 mM NaCl and not at 0 mM NaCl. DLS also indicated that at 5 mg/mL protein and 0 mM NaCl, A127R, wt, and D138K (to a smaller extent) form a broad range of higher molecular weight aggregates.

These aggregates are too weakly associated to withstand FPLC treatment as no aggregates were observed on the sizing column under any conditions. Aggregate formation is concentration-dependent, as wt samples at 1 mg/mL had individual dimer visible in DLS data, but at 5 mg/mL only aggregate was present (Figure 2.13). D138K was predominantly 24mer at 800 mM NaCl and mostly dimer (with some 24mer) at 0 mM NaCl, whereas E65R remained fully assembled at both salt concentrations. Native gel results also support the uniqueness of the E65R mutant, as shown in Figure 2.14, where E65R was the only protein to run similar to horse spleen apoferritin (HSAF, used as a control due to its lack of salt-mediated disassembly). WT, D138K, and A127R all ran as smaller species.

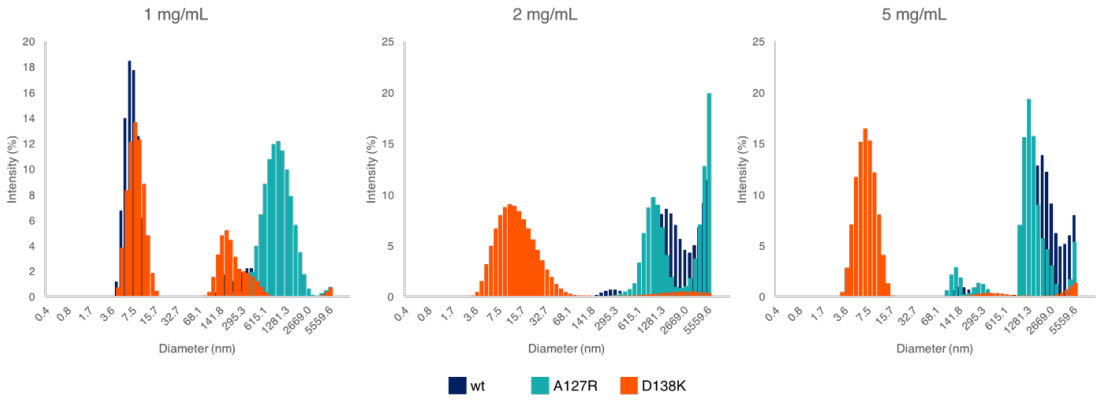

Figure 2.13. DLS in no-salt conditions at varying protein concentrations. At higher concentrations, wt and A127R have a greater tendency to aggregate compared to D138K, which maintains discrete dimers at all protein concentrations tested.

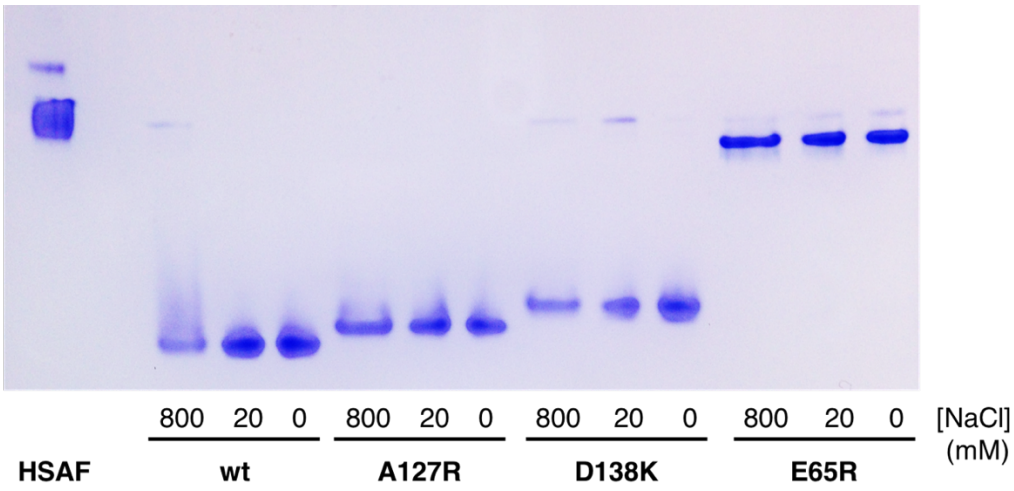

Figure 2.14. Native gel (4-20%) showing enhanced stability of E65R 24mer compared to wt, A127R, and D138K. Horse spleen apoferritin (HSAF) was used as a marker to indicate where a ferritin 24mer cage should run, as it does not have ionic strength-dependent assembly.

Self-assembly Kinetics

By monitoring particle size using DLS, we were also able to investigate differences in the kinetics of 24mer assembly for wt, A127R, and D138K. Because E65R does not disassemble with decreasing ionic strength, no changes were observed by DLS or SEC upon changing the buffer conditions. We started with disassembled protein in 0 mM NaCl buffer, which was transferred to 800 mM NaCl buffer to induce self-assembly. The rate of assembly was concentration-dependent, particularly for A127R and wt (Figure 2.15). For wt protein at 5 mg/mL, assembly appeared to be complete within 4 h. For A127R at 5 mg/mL, assembled 24mer population increased up to 75% over 4 h, and then stalled with no further assembly. At 2 mg/mL, both wt and A127R took approximately 24 h to reassemble. At 1 mg/mL, wt assembly occurred within 10 min (the time it took to prepare samples and take the DLS measurement), and A127R was >90% 24mer within 2 h. Assembly was significantly faster for D138K compared to wt and A127R at 2 and 5 mg/mL. At these concentrations the D138K samples were >90% 24mer within 10 min. At

1 mg/mL, assembly was still quite fast, with a population of >80% 24mer within 10 min. Rapid assembly kinetics with D138K at all concentrations tested is consistent with lack of aggregate formation, and an orderly process of subunit assembly. This feature should lead to more reversible and higher-yielding ferritin disassembly and assembly processes with D138K, e.g., as required for cargo loading.

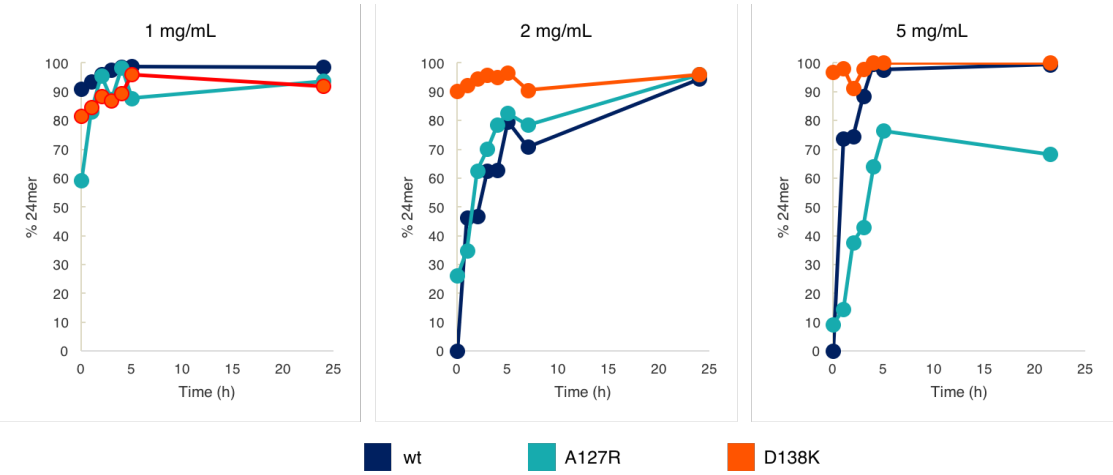

Figure 2.15. DLS was used to monitor assembly of wt and mutants, starting from dimers. Assembly rate was concentration-dependent for A127R, with faster assembly at lower protein concentrations. WT showed fastest assembly at 1 mg/mL, followed by 5 mg/mL and 2 mg/mL. D138K assembled within the time it took to take the measurement for all protein concentrations tested.

We observed a less dramatic difference among the protein disassembly kinetics, moving samples from 800 mM NaCl to 0 mM NaCl. By DLS, A127R and wt appeared to disassemble immediately, producing large aggregates. The disassembly of D138K was more difficult to monitor by DLS due to the relative similarity in diameter of 24mer and dimer (and lack of aggregates). By SEC, as shown in Figure 2.16, we could observe disassembly for all three proteins within 25 min (the measurement time). Some 24mer remained for D138K within this time frame, which matched the results for the 0 mM NaCl equilibrium measurement (Figure 2.10).

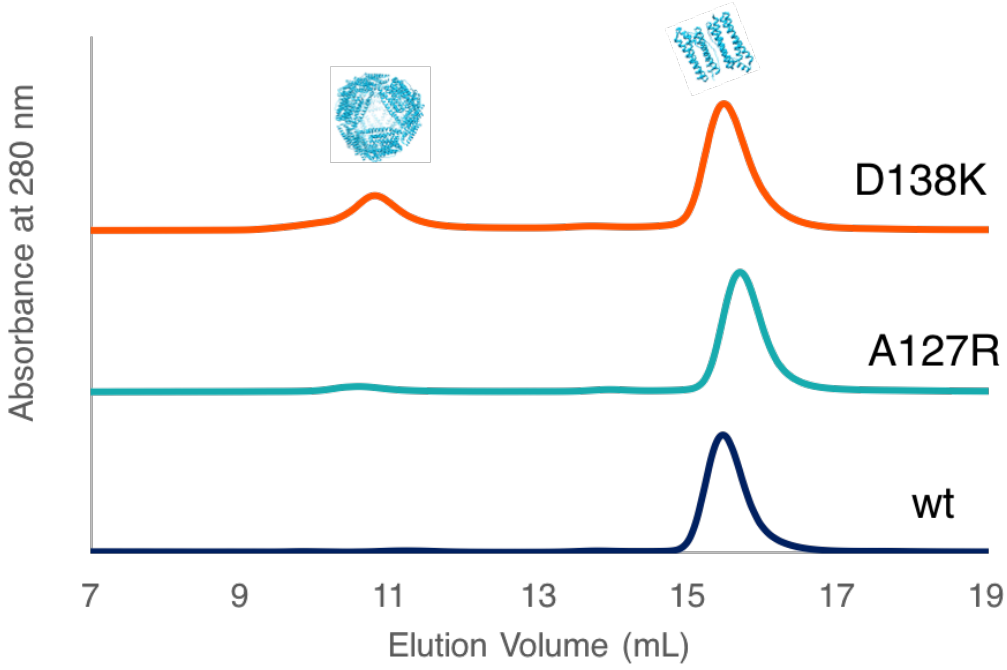

Figure 2.16. SEC shows fast disassembly for all three proteins. Superdex200 Increase column equilibrated with 0 mM NaCl buffer with a flow rate of 0.9 mL/min was used. Samples were 2 mg/mL and were buffer exchanged using a Zebaspin column immediately before chromatography.

X-ray Crystallography

To better understand the significantly enhanced stability of E65R, we obtained a 3.08 Å resolution X-ray crystal structure (PDB ID 5V5K). Although the quality of the electron density maps does not allow for sidechain conformations to be confidently modeled, the crystallography data do offer insights pertaining to the global structure of the E65R mutant. As shown in Figure 2.17, the structure of 24mer E65R shows a shift in the symmetry of the assembled cage to octahedral (as opposed to the tetrahedral structure of wt), resulting in a lack of the large triangular pores. The 544,000 $Å^3$ volume calculated from the structure of the E65R cage using the Voss Volume Voxelator program[113] is roughly 10% smaller than the 600,000 $Å^3$ calculated for a polyALA version of wt (PDB ID 1SQ3)[49] – a finding also reflected in our TEM and DLS results (Table 2.1). These

volumes correspond to outer diameters of 10.1 nm and 10.5 nm for E65R and wt, respectively.

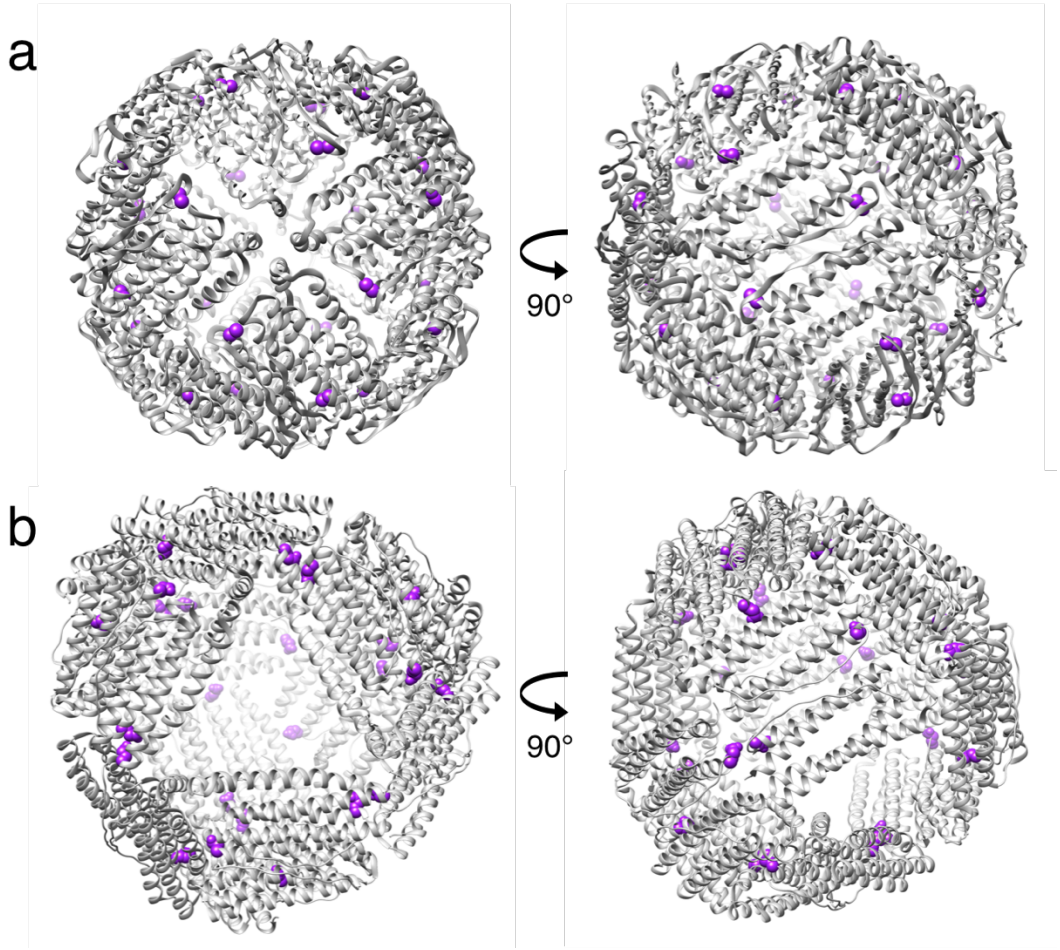

Figure 2.17. E65R exists exclusively in its 24-mer state in a closed-pore assembly. a) Cartoon of E65R crystal structure with residue 65 highlighted in purple. b) Open-pore wt AfFtn (PDB 1SQ3) with residue 65 highlighted in purple.

Exploring E65R Stability Through Mutagenesis

Because our crystal structure does not have high enough resolution to observe individual sidechains, we decided to further investigate the enhanced stability of E65R via mutagenesis. R65 is predicted to form a salt bridge with D138 on a neighboring subunit. If that salt bridge interaction alone causes the enhanced stability observed, removing it should restore wt-like self-assembly in E65R. To test this, we made a double mutant

E65R/D138N, which we expressed, purified, and characterized. By DLS and Trp fluorescence, we saw very similar behavior to the single mutant E65R, with intact assembly at low ionic strengths (Figure 2.18).

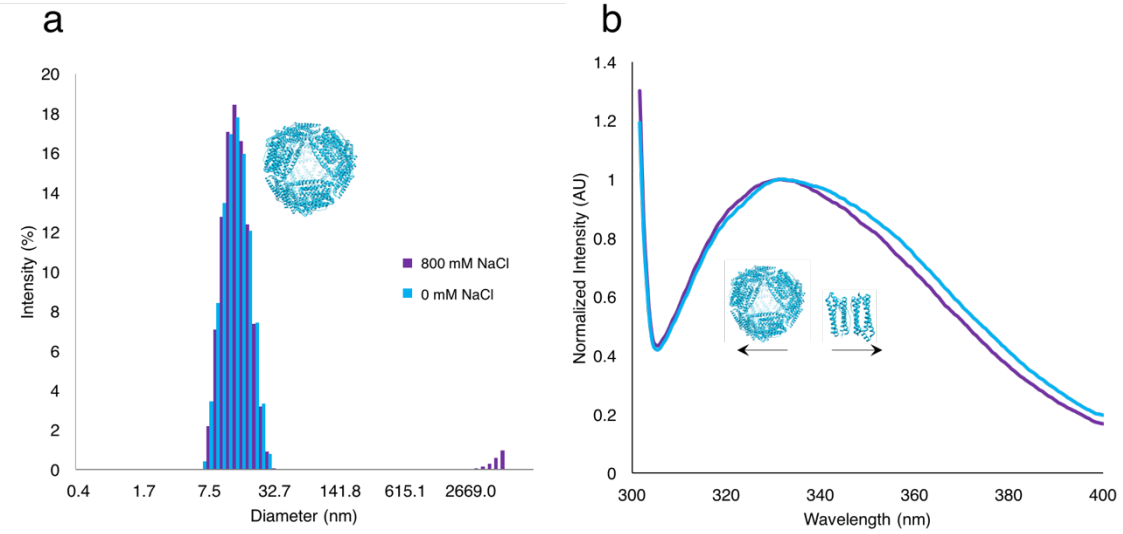

Figure 2.18. Self-assembly characterization of E65R/D138N. a) Dynamic light scattering shows predominantly 24mer at high (violet bars) and low (blue bars) ionic strength. b) Tryptophan fluorescence shows little disassembly upon low ionic strength incubation. Violet line is 800 mM NaCl, blue line is 0 mM NaCl.

Computations for E65R/D138N show that R65 rotates upward to salt bridge with E131 instead of D138 (Figure 2.19), likely maintaining the enhanced cage stability. Although mutation could be done to prevent salt bridging to E131, E131 is in a pocket of negatively charged residues that are all within salt bridging distance of R65. Elimination of one would probably result in R65 shifting to another. Extensive mutagenesis to remove all possible salt bridging partners of R65 is likely to result in significant perturbation of the protein structure and would yield little information on the root cause of E65R enhanced stability. Thus, a higher resolution crystal structure is needed to more fully explain the unique behavior of E65R.

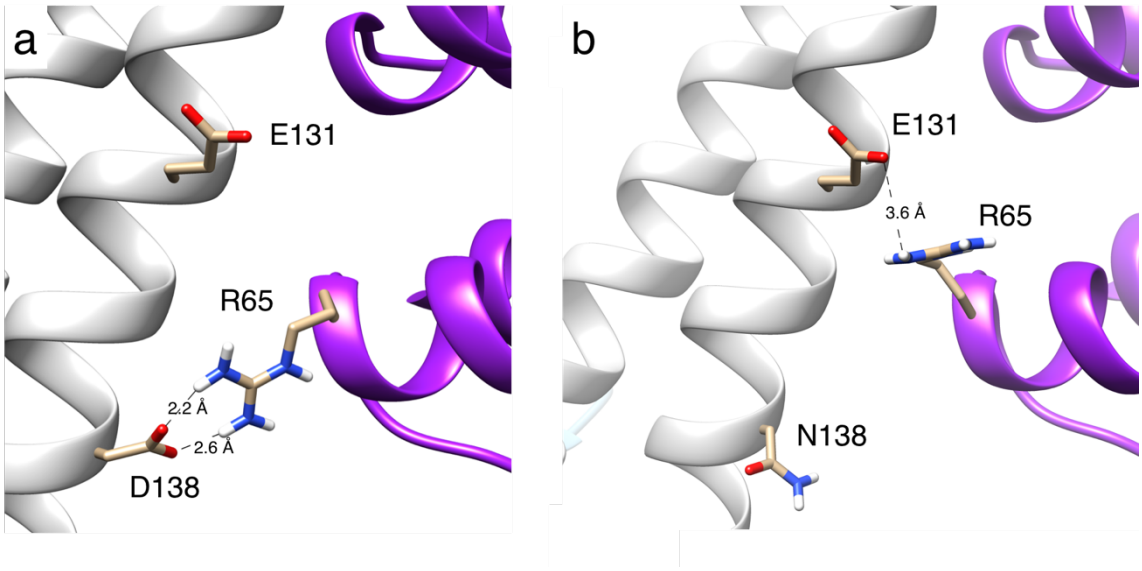

Figure 2.19. Possible salt bridges for E65R and E65R/D138N. a) R65 can pair with D138 on a neighboring subunit, potentially leading to enhanced stability observed. b) When D138 is mutated to N138, R65 is predicted to rotate upward toward E131 and form a salt bridge, maintaining the enhanced stability.

Gold Nanoparticle Encapsulation

Having established differences in self-assembly patterns for the various proteins, we next investigated their interaction with 5 nm AuNPs coated in bis- (*p*-sulfonatophenyl)phenylphosphine (BSPP). We showed previously that BSPP-coated, 5-nm AuNPs are more stably encapsulated within wt-AfFtn compared to citrate-coated AuNPs.[51] To encapsulate the NPs, we first incubated the proteins at 0 mM NaCl overnight at 4 °C to allow for maximum disassembly. We then added AuNPs and incubated for 48 h at room temperature with gentle agitation. After 48 h the presence of AuNP did not disrupt the 2° structure of any of the proteins when incubated at a ratio of 1:1 AfFtn 24mer:AuNP (Figure 2.20).

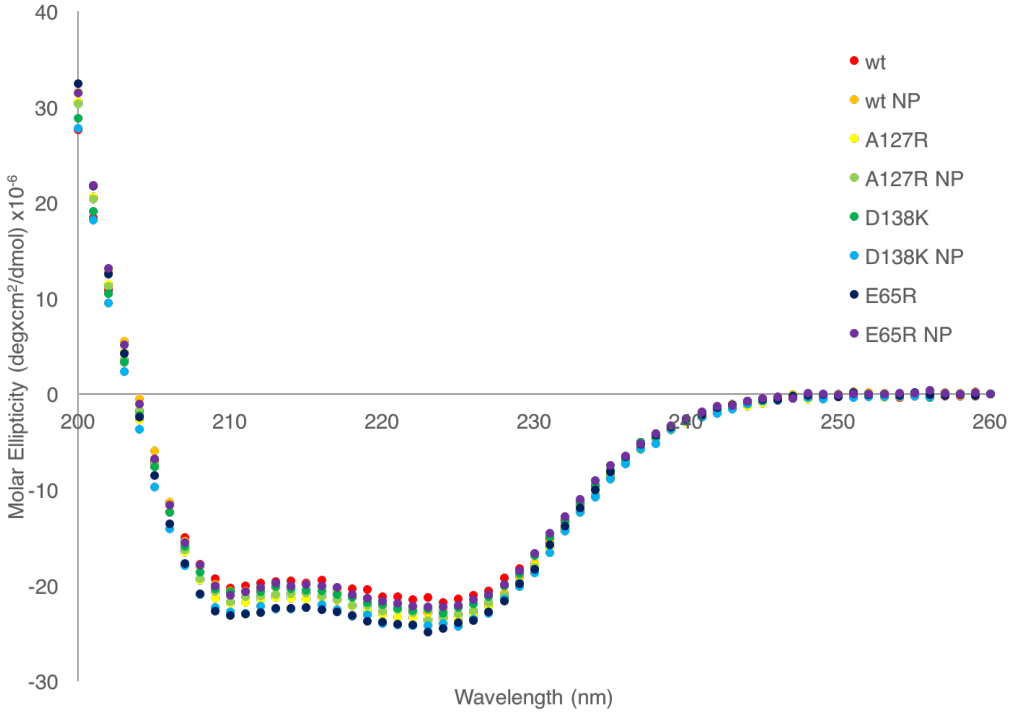

Figure 2.20. CD spectroscopy shows minimal changes in secondary structure upon 48 h incubation with AuNPs. Sample concentration was 0.1 mg/mL protein, 0.2 μM AuNP to minimize AuNP scattering artifacts.

However, by native agarose gel electrophoresis some differences were observed among the samples. By 48 h, wt, A127R, and D138K appeared to successfully encapsulate AuNPs as judged by cleanly overlapping blue protein and red AuNP bands, while the AuNP bands in the E65R-containing sample remained diffuse (Figure 2.21).

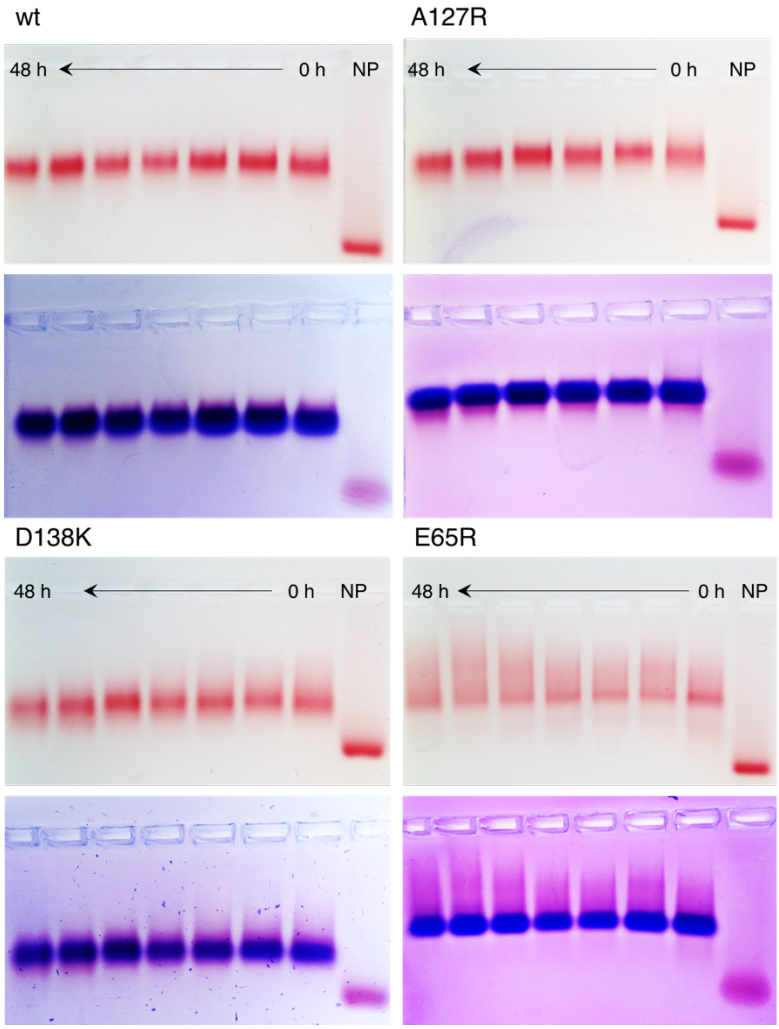

Figure 2.21. Native gel electrophoresis time course for AfFtn-AuNP samples. Samples were 0.6 μM AfFtn, 0.6 μM AuNP in 20 mM phos (pH 7.6).

Shown in Figure 2.22, successful AuNP encapsulation was observed for wt, A127R, and D138K at a ratio of 1:1 AfFtn 24mer:AuNP and higher. In contrast, the AuNP bands for the E65R-containing samples were significantly more diffuse, indicating greater variety in particle charge:mass ratio. Two bands are visible in the Coomassie stained image, with the less intense band overlapping with the darkest part of the AuNP bands. This suggests that although some AuNPs are encapsulated within the E65R cavity, many are not, likely due to less disassembly of the protein cage.

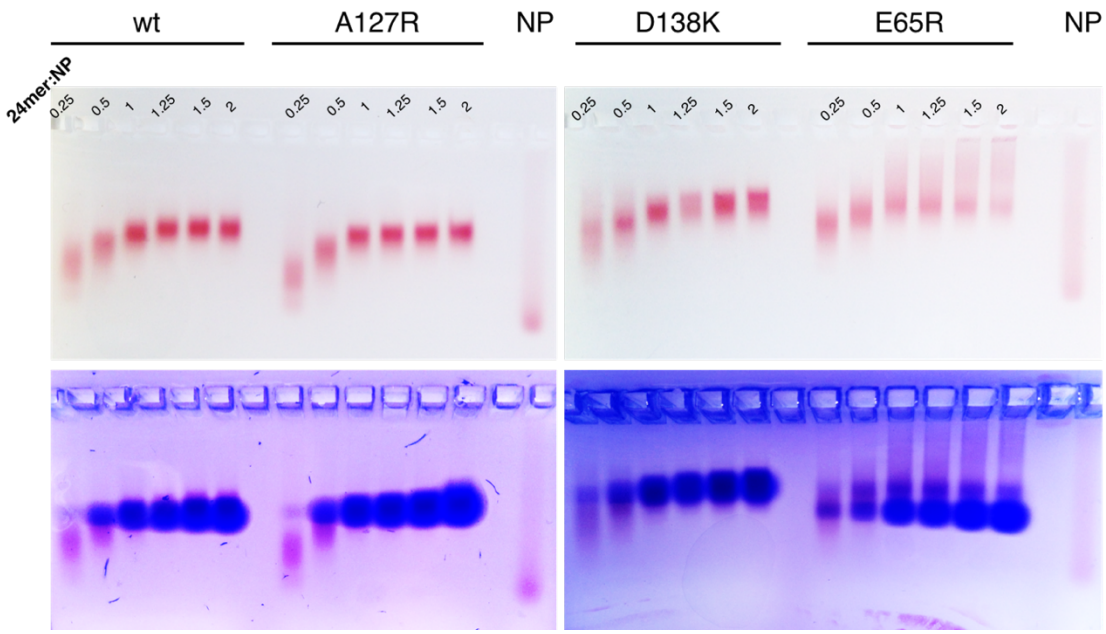

Figure 2.22. Native gel electrophoresis for AfFtn-AuNP samples at varying stoichiometries. AuNP association is seen for wt, A127R, and D138K at ratios of 1:1 AfFtn 24mer:AuNP, but not E65R, which shows lower propensity for disassembly.

We investigated the ability of the protein to stabilize the AuNPs against salt-induced aggregation. With increasing ionic strength, electrostatically-stabilized AuNPs begin to aggregate, causing a red shift in the surface plasmon resonance (SPR) peak.[114] By monitoring the SPR peak with increasing concentration of NaCl, we could observe how well the proteins passivated the AuNP surface (Figure 2.23). Bare AuNPs had the largest SPR red-shift of over 40 nm, from 0 to 800 mM NaCl. E65R-AuNP had the next largest shift of approximately 20 nm, while wt-AuNP, A127R-AuNP, and D138K-AuNP all had similarly small red shifts of less than 10 nm. This suggests that E65R does not passivate the surface of the AuNP, in agreement with the native gel results. As a 24mer, E65R likely interacts with the AuNP surface, providing a smaller stabilizing effect compared to wt,

A127R, and D138K. By TEM (Figure 2.24), several 24mer cages can be seen in contact with the AuNP surface, supporting this hypothesis.

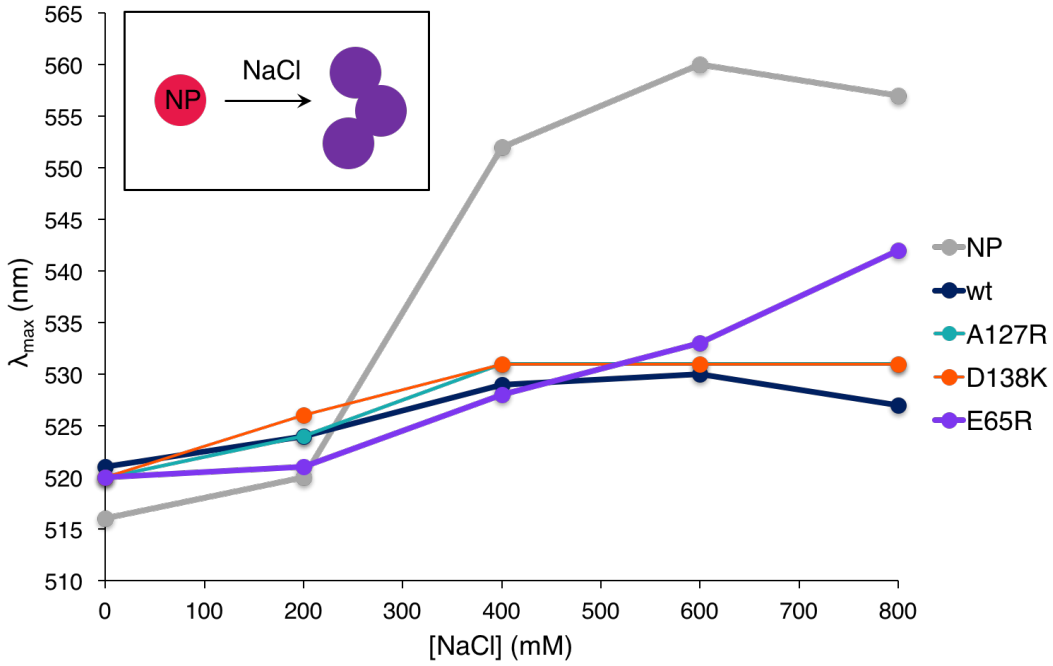

Figure 2.23. AuNP salt stability assay. Changes in SPR peak maximum with respect to salt concentration show higher stability for AuNPs that appear associated with proteins by gel.

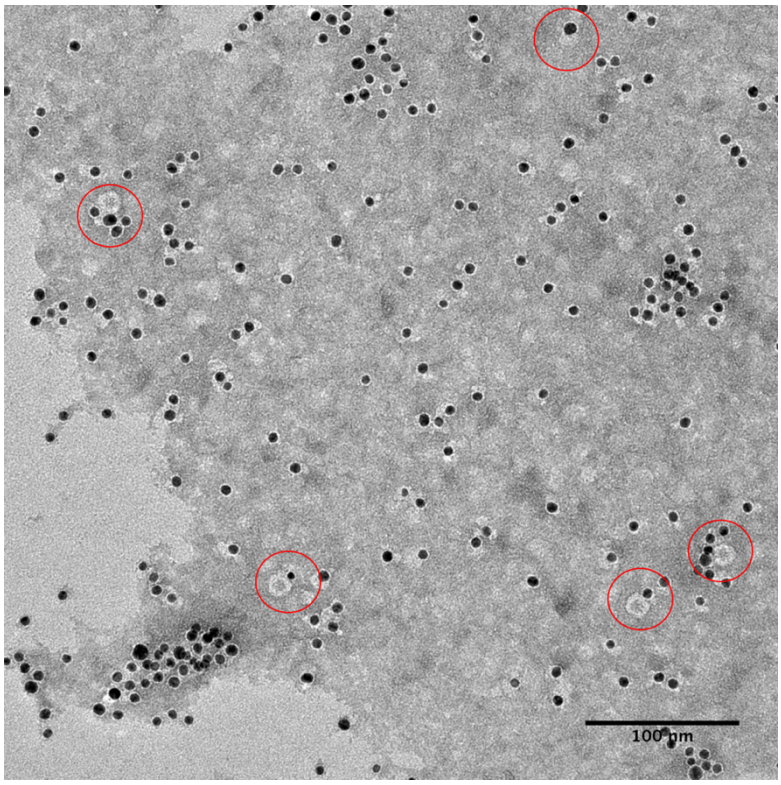

Figure 2.24. TEM micrograph of E65R-AuNP sample, showing 24mer cages near AuNP surface (highlighted in red circles).

We also explored the AuNP templating ability of the protein, after encapsulating a preformed 5-nm AuNP. By adding additional gold salt and reducing agent, the AuNP can be further grown inside the AfFtn cavity, with the protein acting as a template to constrain growth.[51] As shown in Table 2.2 and Figure 2.25, all of the proteins with high encapsulation yields showed controlled particle growth to ~7 nm with narrow size distributions. As expected, E65R-AuNP had a comparatively wider size distribution and larger average particle size. The UV-vis spectra of the templating samples also showed differences between high-encapsulating and low-encapsulating proteins (Table 2.2 and Figure 2.26). Whereas wt, A127R, and D138K all had post-growth SPR peak positions unchanged from the initial 519 nm, the E65R sample redshifted to 524 nm, indicating a small amount of

aggregation. The SPR peak width is indicative of particle size distribution, with narrower peaks corresponding to narrower distributions. The SPR width decreased after templating for the wt, A127R, and D138K samples, but increased for E65R, supporting TEM results that suggest a broader AuNP size distribution. These results suggest that wt, A127R, D138K successfully encapsulate the AuNP and template further growth, whereas E65R is more selective and encapsulates fewer NPs, resulting in less templated growth.

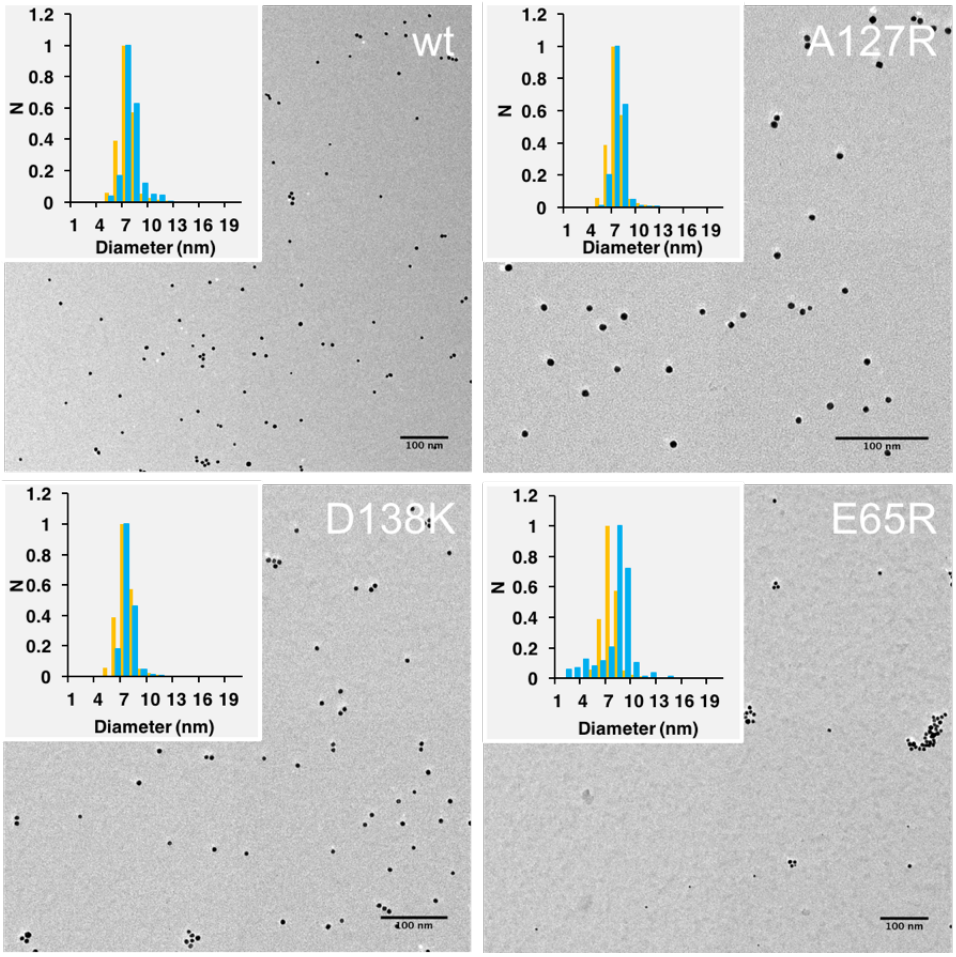

Figure 2.25. TEM micrographs post-particle growth. Insets show normalized size distributions based on TEM images. Yellow bars are pre-growth samples, blue bars are post-growth. Scale bars are 100 nm.

Table 2.2. Gold nanoparticle templating summary

Sample	D_{avg} AuNP (nm)[a]	N[b]	SPR post-growth (nm)	Change in SPR width (nm)[c]
wt-AuNP	7.2 ± 1.1	366	519	-8
A127R-AuNP	6.8 ± 0.7	464	519	-10
D138K-AuNP	6.8 ± 0.7	379	519	-10
E65R-AuNP	7.2 ± 1.8	224	524	4

[a]Average diameter of AuNPs post-templated growth.
[b]Number of particles measured using the Analyze Particles feature of ImageJ[111] to calculate average diameter.
[c]As calculated by 2x the half-width, half-max of the peak.

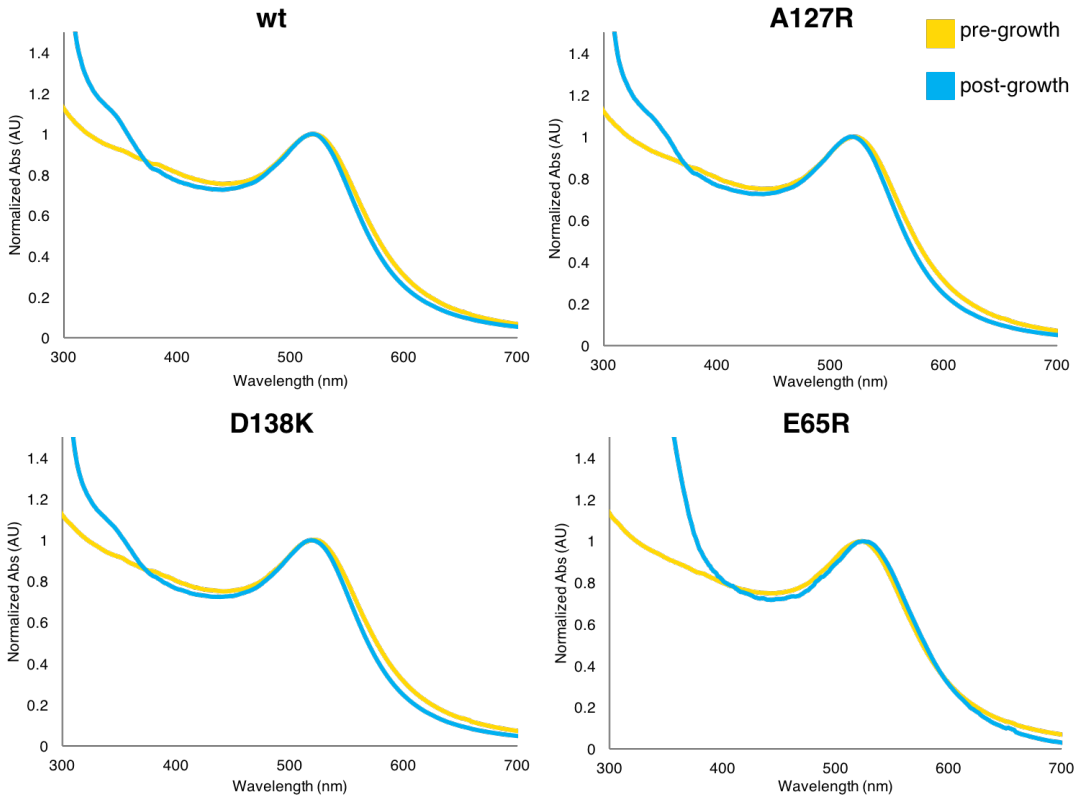

Figure 2.26. UV-vis spectra for AuNP templating. Pre-growth spectra are in yellow, post-growth spectra are in blue.

2.3 Discussion

We have expressed and characterized three novel AfFtn mutants, each replacing a negative or neutral residue with one that is positively charged. None of the mutations decreased the thermal stability nor hampered the ability of the protein to self-assemble into

a nanocage at high ionic strengths. However, the results presented here demonstrate the profound effect a single point mutation can have on the self-assembly of AfFtn. This is in keeping with recent literature, where *E. coli* bacterioferritin,[38] ferritin-like DNA binding protein from starved cells (Dps),[37] and bullfrog ferritin[43] were also shown to be susceptible to changes in self-assembly through minor mutagenesis. While the AfFtn mutations changing a negative residue to a positive one (D138K and E65R) showed increased 24mer population in low ionic strength solutions, changing a neutral residue to a positive one (A127R) showed similar behavior to wt, and even slight destabilization of the 24mer. Even between D138K and E65R there were significant differences in the favorability of 24mer assembly, with E65R remaining >90% 24mer in all salt concentrations tested and D138K disassembling at low salt conditions. The specific interdimer location of the point mutation greatly affects self-assembly.

It is notable that E65R shows enhanced subunit thermal stability in addition to its assembly stability. Increased thermal stability can often go hand-in-hand with enhanced cage stability. For example, when the self-assembly equilibrium of *E. coli* bacterioferritin[39] was shifted from a mixture of dimer and 24mer to 100% 24mer, the T_m increased by over 20 °C. The inverse can also be true, as destabilization in favor of dimers has led to decreased thermal stability in mycobacteria ferritin,[115] *E. coli* ferritin A,[42] Dps,[37] and *E. coli* bacterioferritin.[38] However, in *E. coli* bacterioferritin, mutations designed to plug an interdimer water pocket with hydrophobic residues led to significantly enhanced thermal stability (ΔT_m >20 °C) and yet greater dimer population compared to the wt, as the geometry of the more stable dimers prevented cage formation.[40] Although A127R appears

to favor dimer more than wt at low-salt conditions, its subunit thermal stability is identical. For D138K, its enhanced 24mer stability at low-salt conditions also does not appear to be linked to thermal stability, as it too exhibits the wt T_m.

All our results support enhanced cage stability for E65R and D138K at low ionic strengths. The symmetry shift seen in the crystal structure of E65R is striking (Figure 2.27a) but cannot alone explain the enhanced cage stability. A double mutant of AfFtn, K150A/R151A, was previously shown to change the cage symmetry to octahedral; however, it maintained the salt-dependent disassembly and reassembly behavior of the wt protein.[116] It is remarkable that in our study a single point mutation led to such a dramatic change in assembly behavior. This symmetry shift can be rationalized using the computationally predicted side chain conformation of R65. In the tetrahedral assembly, the amino acid exists in two distinct environments due to the symmetry of the cage. In one environment, R65 on one subunit is positioned directly across from R65 of a neighboring subunit (Figure 2.27b), resulting in electrostatic repulsion. In the octahedral assembly, however, R65 is in only one environment, highly similar to the 3-fold axis in the open pore wt, and the residue is not in proximity to an R65 residue on a separate protomer, which is consistent with octahedral assembly being preferred. Within the model of E65R, R65 and D138 form a salt-bridge at the interface present in both the tetrahedral and octahedral assemblies (Figure 2.27c), which could lead to the enhanced cage stability observed. A127R was also predicted to form complementary electrostatic interactions (Figure 2.27d). However, Arg127 is conformationally constrained at an interface that is more sterically crowded than the pore environment where the mutations E65R and D138K were introduced. With A127R, this introduction of a large residue at a subunit interface may

reduce the stability of the 24mer at low-salt concentrations relative to the wild type. Within the model of D138K, a K138-D34 salt bridge is observed between neighboring subunits, which may increase the population of 24mer relative to wild type (Figure 2.25e).

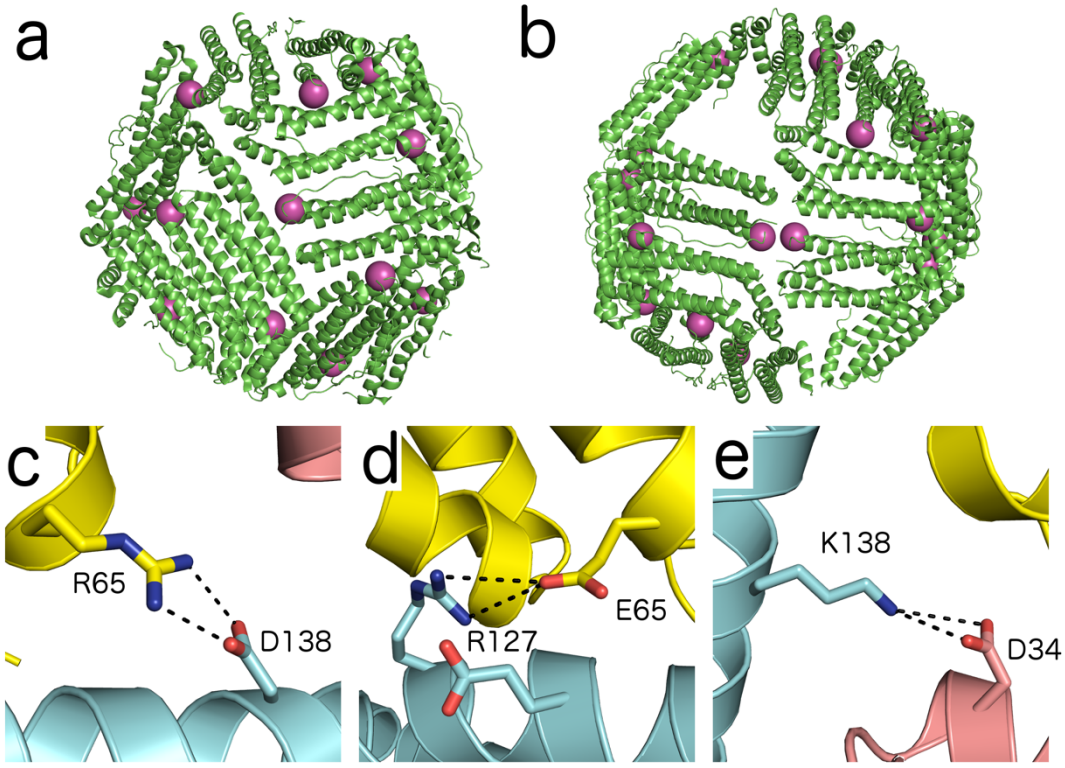

Figure 2.27. Inter-protomer interactions in mutants of AfFtn. Crystallographic structures of AfFtn with site 65 highlighted as purple sphere (a, b). (a) Crystallographic structure for E65R reported herein (closed form, octahedral structure). (b) Structure of wt AfFtn (PDB ID 1SQ3) (open pore, tetrahedral structure). Two R65 are in close proximity at one interface. (c-e) Computationally modeled structures of mutants with most probable conformations of mutated side chains. Distinct protomers (chains) have different colors: cyan, yellow, and pink. (c) Within E65R, potential R65-D138 salt bridge. (d) Within A127R, a potential R127-E65 salt bridge within a sterically crowded local environment. (e) Within D138K, a potential K139-D34 salt bridge.

Both mutants capable of disassembly (A127R, D138K) showed interaction with AuNPs by gel, unlike E65R, which does not disassemble. It is interesting that we see changes in self-assembly kinetics for the proteins alone, and yet in the presence of AuNPs, protein assembly encapsulating the AuNP seems to be similarly fast for wt, A127R, and D138K. High ionic strength solution perhaps does not model the charged AuNP surface

and thus differences seen in protein-only assembly are not observed in the presence of AuNPs. We hypothesize that the AuNP nucleates protein assembly at its surface and may thereby increase the effective concentration of protein in solution. Our DLS results suggest that protein concentration has a large effect on the rate of protein cage assembly, with decreasing concentration paradoxically leading to faster assembly. This is likely due to minimal aggregation of dimers at low concentrations, allowing assembly to occur. We were unable to monitor reassembly by DLS at 0.3 mg/mL due to low signal-to-noise ratio, but based on our results from 1, 2, and 5 mg/mL samples, we would expect assembly to occur rapidly at 0.3 mg/mL for all three proteins that disassemble.

When NPs are introduced into a biological medium, protein adsorption is rapid and evolves with time. This shell of protein on the surface of NPs is termed the protein corona.[64] Protein adsorption has been shown to sterically stabilize NPs against aggregation with increasing salt concentration,[72,117] similar to our results. A127R, D138K, and wt protein all successfully encapsulated AuNPs as seen by native gel, prevented aggregation of AuNPs with increasing ionic strength compared to particles without protein present, and enabled effective AuNP templating. Although E65R does not encapsulate AuNPs at the same high yields as the disassembling proteins, there is still some level of AuNP stabilization, as the SPR red shift for the E65R-AuNP sample was smaller compared to bare particles. The fully-assembled E65R cage may be adsorbed to the NP surface, which does not provide full encapsulation, but may be enough to somewhat stabilize the particle. This hypothesized adsorption is also not enough to prevent less controlled particle growth upon addition of gold salt and reducing agent. It is possible that the cage dynamics of E65R are such that some AuNPs are encapsulated, as indicated by faint bands overlapping by native gel

(Figure 2.21 and 2.22). Such is the case for lumazine synthase from *Aquifex aeolicus*, a protein cage capable of encapsulating large cargo without first disassembling.[118] The greater 24mer stability and cargo selectivity exhibited by E65R opens up the possibility of designing more specific ferritin-cargo interactions in the future. We are beginning to explore new types of cargo for ferritin encapsulation.

2.4 Conclusions

We have shown that single point mutations of AfFtn can have varying effects on thermal stability, assembly symmetry, and self-assembly equilibrium, kinetics, and reversibility. More dramatic charge changes such as changing negatively charged residues to positive ones increased the stability of the 24mer in decreasing ionic strength, while a less dramatic change, changing a neutral residue to a positive one, had a slightly destabilizing effect. The E65R mutant shows enhanced cage formation as well as thermal stability, formation of the 24mer at low salt conditions, and self-assembly in octahedral symmetry rather than tetrahedral. The kinetics of self-assembly were also affected by mutation, with A127R showing slower nanocage assembly compared to wt, and D138K assembling faster. These results corroborate earlier studies in other ferritin species, demonstrating the generality of single point mutations along subunit interfaces dramatically affecting cage self-assembly. All mutants showed some salt stabilization of AuNPs compared to bare particles, but only mutants that retained their ability to disassemble showed full AuNP encapsulation and well-controlled templated AuNP growth. Enhanced control over protein cage assembly could have applications in delivery, nanomaterials separations, and controlled inorganic NP synthesis.

2.5 Experimental Procedures

Computational design of AfFtn mutants. Using atomic coordinates from chains G, H and J of the crystallographic structure of *Archaeoglobus fulgidus* thermophilic ferritin (PDB ID 1SQ3[49]), amino acid probabilities were calculated independently for sites 34, 65, 127, 131, and 138. Sites 127, 131, and 138 are situated along a helical interfacial region. Sites 34 and 65 were chosen as they form, along with site 138, the center of a carboxylate-rich pore. Eighteen natural amino acids were considered at each site selected; cysteine and proline were precluded. For each mutation calculation, residues other than the site of interest were constrained to the crystal structure conformations. Side-chain conformational states of mutated sites were taken from a rotamer library.[119,120] An entropy-based, probabilistic formalism was used to calculate the probabilities of the amino acids and their rotamer conformations.[121–124] Using CHARMM19,[119] hydrogen atoms were added, and energies were calculated using the dihedral, van der Waals, and electrostatic terms, with a non-bonded cut-off of 8 Å. The probabilistic approach has an effective parameter β that is conjugate to the average energy over sequences and side chain conformations; $\beta = 0.5$ mol/kcal for these calculations.[121–123] The probability of each amino acid at a mutated site was the sum of the calculated probabilities of its side-chain conformations.

Mutagenesis. Site-directed mutagenesis was used to generate the mutant AfFtn plasmids using the Quik Change kit (Stratagene). Primers used to generate the mutations were purchased from Integrated DNA Technologies and are listed below:

E65R

Forward (5′-3′): GATTTCGTTTCCCGTCGCGGTGGCCGTG

Reverse (5 ′-3′): CACGGCCACCGCGACGGGAAACGAAATC

A127R

Forward (5′-3′): CTGCAGTGGTACGTTCGTGAACAAGTGGAAG

Reverse (5′-3′): CTTCCACTTGTTCACGAACGTACCACTGCAG

D138K

Forward (5′-3′): GGAGGAAGCCTCTGCCCTCAAAATTGTGGAGAAGCTGAGG

Reverse (5′-3′): CCTCAGCTTCTCCACAATTTTGAGGGCAGAGGCTTCCTCC

E65R/D138N (used E65R plasmid as the template, the following primers inserted D138N mutation):

Forward (5′-3′): GTTTCTCAACGATGTTCAGGGCGCTCGCTTC

Reverse (5′-3′): GAAGCGAGCGCCCTGAACATCGTTGAGAAAC

Mutations were confirmed using Sanger Sequencing on ABI 3730, provided by the DNA Sequencing Facility at the University of Pennsylvania.

Protein expression and purification. The plasmids were transformed in *E. coli* BL21-CodonPlus(DE3)-RP cells and cultured overnight in LB medium at 30 °C, supplemented with 100 μg/mL ampicillin and 35 μg/mL chloramphenicol. The cultures were then transferred to 1 L terrific broth (TB) supplemented with the same antibiotics and grown at 37 °C until OD_{600} reached ~0.6-0.8. The cells were then induced with 1 mM isopropyl β-D-1-thiogalactopyranoside (IPTG) for 4 h. Cells were lysed by treating with lysozyme at rt for 30 min, followed by sonication. The cell-free extract was obtained by centrifugation (30 min, 6 krpm, 4 °C), and after adding $MgCl_2$ to a final concentration of 2 mM, the supernatant was treated with DNAse for 15 min at rt. The solution was then heat shocked at 80 °C for 10 min and soluble protein was obtained following centrifugation (1 h, 9 krpm, 4 °C). The supernatant was filtered and buffer exchanged to assembly buffer (2 M NaCl, 1 mM EDTA, 20 mM phos, pH 7.6). The protein was concentrated and injected onto a HiLoad 16/60 column equilibrated with high-salt buffer (800 mM NaCl, 20 mM

phos, pH 7.6). Purity was confirmed using SDS-PAGE (4–15% tris–HCl, Mini-Protean TGX gel). By UV-vis spectroscopy no significant DNA contamination was observed. Identify was confirmed using matrix-assisted laser desorption ionization-time of flight mass spectrometry (MALDI-TOF MS), using sinapinic acid as a matrix and linear positive mode ion generation. Protein concentration was determined using the Bradford Assay, with bovine gamma globulin as a standard. Average protein yield was 12 mg/L TB.

Transmission electron microscopy (TEM). TEM samples were prepared using glow-discharged carbon-coated copper grids (Electron Microscopy Sciences). The grids were floated on 5 μL of sample for 5 min, washed with 2 drops of distilled water, and stained with 2% ammonium molybdate or uranyl acetate. Micrographs were obtained using a Tecnai T12 electron microscope operating at 120 keV. Images were analyzed using ImageJ.[111]

Circular dichroism spectroscopy (CD). CD data were obtained using an Aviv 410 CD spectrometer (Aviv Biomedical; Lakewood, NJ) with 1 mm quartz cuvette (Hellma USA). Protein samples were 0.3 mg/mL in high-salt buffer. For melting point determination, the signal at 222 nm was monitored as temperature increased 1-96 °C, with a 1 min equilibration at each 1 °C step. Signal was averaged over 10 s at each temperature.

Differential scanning calorimetry (DSC). A VP-DSC microcalorimeter was used to measure the T_m of E65R and wt proteins. Buffer scans were run overnight prior to sample measurement. Samples of 0.5 mg/mL protein in high-salt buffer were degassed with stirring at 10 °C before loading into the sample chamber. The temperature range was 10-125 °C with a scan rate of 60 °C/h.

Ferroxidase activity assay. Ferritin samples were buffer exchanged to 25 mM tris (pH 7.0) and diluted to 0.1 mg/mL, 800 μL total volume. A fresh solution of 10 mM $FeSO_4$ was prepared in 5 mM HCl to prevent premature oxidation. Ferroxidase activity was monitored at 315 nm and 37 °C with stirring using an Agilent 8453 UV-visible spectrometer. The absorbance was measured at 10 s intervals over a total time of 600-800 s, adding 480 eq iron per AfFtn 24mer after an initial ~20 s.

Tryptophan fluorescence. Steady-state fluorescence spectra were collected on a Varian Cary Eclipse fluorescence spectrophotometer (Cary Eclipse software, 2003) using 100 µL quartz cuvette (Starna Cells). Protein samples were prepared at 5 mg/mL and incubated overnight at 4 °C in the appropriate high-salt or no-salt buffer (20 mM phos, pH 7.6). Samples were excited at 295 nm, scanned 300-400 nm, with a PMT voltage of 700-750 V, at 25 °C.

Dynamic light scattering (DLS). DLS data were collected on a Zetasizer Nano ZS (Malvern). Protein samples (5 mg/mL) were prepared in 0.22 µm filtered high-salt or no-salt buffer and incubated overnight at 4 °C. The measurements were done in plastic micro cuvettes at 25 °C, with backscatter detection at an angle of 173°.

Size exclusion chromatography (SEC). Samples of 5 mg/mL protein were prepared in 20 mM phos (pH 7.6), varying concentrations of NaCl, and incubated overnight at 4 °C. Samples of 200 µL were injected onto a Superdex200 Increase 10/300 GL column equilibrated with the same buffer, using an ATKA FPLC (GE Healthcare). The samples were run at 4 °C with flow rate of 0.9 mL/min.

Native gel electrophoresis. For PAGE analysis, 2.4 μg protein was loaded onto 4–20% tris–HCl gels (Mini-Protean TGX) and run at 150 V for 90 min, on ice. The running buffer was tris-glycine (25 mM tris, 192 mM glycine, pH 8.3). Agarose gels (0.7%) were run at 100 V for 20 min at room temperature, with 5 mM NaCl, 20 mM phos (pH 7.6) as the running buffer.

X-ray crystallography. Crystals of E65R were prepared by mixing 2 μL of protein solution (10 mg/mL E65R in high-salt buffer) with 2 μL of precipitant solution (0.45 M potassium phosphate monobasic, 0.3 M sodium phosphate monobasic, 5% (v/v) glycerol) in a sitting drop suspended over a 500 μL reservoir of precipitant solution. The sitting drop was streak seeded with E65R crystals previously grown in the same conditions. The crystallization tray was incubated at 21 °C, and large octahedral crystals appeared within 24 h. Single crystals of E65R were briefly immersed in cryoprotectant solution (0.8 M potassium phosphate monobasic, 0.8 M sodium phosphate monobasic, 20% (v/v) glycerol) before being flash-cooled in liquid nitrogen. X-ray diffraction data from single crystals of E65R were collected at beamline 9-2 at the Stanford Synchrotron Radiation Lightsource (SSRL). Diffraction data were integrated using iMosflm[125] and processed using AIMLESS[126] from the CCP4 suite of programs.[127] The structure of E65R was phased in PHENIX[128–130] by molecular replacement using a monomer of wild-type AfFtn (PDB ID 1SQ3).[49] Structure refinement was performed in PHENIX and manual model adjustments were made in COOT.[131] Initial rounds of refinement showed ambiguous density in the 2Fo-Fc map for protein sidechains, so a polyALA model for E65R was used in which all protein sidechains were replaced with alanine. The lack of density in the Fo-Fc difference map

after refinement with polyALA E65R affirmed that sidechain conformations could not be confidently assigned based on experimental data. Refinement proceeded until R_{free} converged at its lower limit. The quality of the final model was assessed using MolProbity[132] and the wwPDB validation server. Data collection and refinement statistics are recorded in Table 2.3. Figures were generated using PyMOL.[133]

Table 2.3. Data collection and refinement statistics

	AfFtn E65R
wavelength (Å)	0.979
resolution limits (Å)[a]	99.15 – 3.08 (3.25-3.08)
unit cell	
space group	$P2_13$
a, b, c (Å)	171.7, 171.7, 171.7
α, β, γ (°)	90.0, 90.0, 90.0
total/unique reflections	566942/31499
multiplicity[a]	18.0 (18.9)
R_{merge}[a,b]	0.164 (1.031)
R_{pim}[a,c]	0.056 (0.348)
$CC_{1/2}$[a,d]	0.999 (0.570)
$I/\sigma(I)$[a]	15.0 (3.6)
completeness (%)[a]	100 (100)
R_{work}[e]	0.26
R_{free}[f]	0.28
root-mean-square deviations	
bonds (Å)	0.003
angles (°)	0.891
Ramachandran plot (%)[g]	
favored	91.2
allowed	8.7
outliers	0.2
PDB accession code	5V5K

[a] Values in parentheses refer to the highest-resolution shell of the data.
[b] $R_{merge} = \sum|I_h - \langle I_h\rangle|/\sum\langle I_h\rangle$; I_h = intensity measure for reflection *h;* $\langle I_h\rangle$ = average intensity for reflection *h* calculated from replicate data.
[c] $R_{pim} = \sum(1/(n-1)^{1/2}|I_h - \langle I_h\rangle|/\sum\langle I_h\rangle$; n = number of observations (redundancy).
[d] $CC_{1/2} = \sigma_\tau^2/(\sigma_\tau^2 + \sigma_\varepsilon^2)$, where σ_τ^2 is the true measurement error variance and σ_ε^2 is the independent measurement error variance.
[e] $R_{work} = \sum||F_o| - |F_c||/\sum|F_o|$ for reflections contained in the working set. $|F_o|$ and $|F_c|$ are the observed and calculated structure factor amplitudes, respectively.
[f] $R_{free} = \sum||F_o| - |F_c||/\sum|F_o|$ for reflections contained in the test set held aside during refinement (5% of total).
[g] calculated by MolProbity

Salt stability assay. 5-nm citrate-capped AuNPs were purchased from TedPella. Ligand exchange to BSPP was performed as previously published.[51] Protein-AuNP samples were prepared by first disassembling AfFtn overnight in no-salt buffer at 4 °C. Disassembled protein was mixed with AuNPs to a final concentration of 0.6 μM AfFtn, 0.6 μM AuNP in 0 mM NaCl buffer. The sample was incubated at rt with gentle agitation (gel rocker) for 48 h. After incubation, 50 μL sample was mixed with 50 μL increased salt buffer (0, 400, 800, 1200, 1600 mM NaCl, 20 mM phos, pH 7.6) for final salt concentrations of 0, 200, 400, 600, 800 mM NaCl. UV-vis spectra were collected using an Infinite M1000 microplate reader (Tecan).

Gold nanoparticle templating. $AuCl_3$ (10k equivalents) were added to protein-AuNP samples (0.6 μM AfFtn, 0.6 μM AuNP) and incubated at rt for 3 h. Samples were then desalted on a 10DG column pre-equilibrated with 0 mM NaCl buffer to remove excess $AuCl_3$. Pink fractions containing protein-AuNP were combined and 30k equivalents of freshly prepared ascorbic acid were added. Samples were incubated overnight at rt and characterized by UV-vis and TEM. TEM micrographs were analyzed using the Analyze Particles function in ImageJ,[111] with 5-infinity nm^2 as the particle area range and 0.5-1.0 as the circularity.

2.6 Acknowledgments

This work was supported by the NSF (PD 09-6885). MALDI-TOF MS was purchased with NSF grant CHE-0820996. J.G.S. and I.J.D. acknowledge support from NSF CHE-1508318. J.G.S. acknowledges additional support from the Penn Laboratory for

Research on the Structure of Matter (NSF DMR-1120901). This work used the Extreme Science and Engineering Discovery Environment (XSEDE), which is supported by National Science Foundation grant number ACI-1053575, under grant number TG-CHE110041. B.W.R. was supported by an NIH Structural Biology and Molecular Biophysics Training Grant. J.A.V. was supported in part by an NIH Chemical-Biology Interface Training Grant. T.L.H. was supported by the REU program of the LRSM (Penn MRSEC) through NSF grant DMR-1062638 Penn-REU summer fellowship, NSF DMR 11-20901. The authors thank Eric Johnson for providing the *Archaeoglobus fulgidus* ferritin gene in the pAF0834 plasmid. We thank the Stanford Synchrotron Radiation Lightsource for access to beamline 9-2. Use of the Stanford Synchrotron Radiation Lightsource, SLAC National Accelerator Laboratory, is supported by the U.S. Department of Energy, Office of Science, Office of Basic Energy Sciences under Contract No. DE-AC02-76SF00515. The SSRL Structural Molecular Biology Program is supported by the DOE Office of Biological and Environmental Research, and by the National Institutes of Health, National Institute of General Medical Sciences (including P41GM103393). We are grateful to Joshua Wand, Kyle Harpole, and Evan O'Brien for use of and help with the differential scanning calorimeter. We are also grateful to Andrew Tsourkas for use of the ZetaSizer and to the University of Pennsylvania Electron Microscopy Resource Laboratory for use of the TEM.

CHAPTER 3: STRUCTURAL-FUNCTIONAL ANALYSIS OF ENGINEERED PROTEIN-NANOPARTICLE ASSEMBLIES USING GRAPHENE MICROELECTRODES

The content of this chapter has been submitted for publication. It has been adapted here:

Reprinted with permission from Ping, J.; Pulsipher, K.W.; Vishnubhotla, R.; Villegas, J.A.; Hicks, T.L.; Honig, S.; Saven, J.G.; Dmochowski, I.J.; Johnson, A.T.C. Structural-Functional Analysis of Engineered Protein-Nanoparticle Assemblies Using Graphene Microelectrodes. **2017.** *Submitted.*

3.1 Introduction

The ability to attach functional biomolecules to nanoparticle surfaces has spurred development of nano-therapeutic,[94] diagnostic,[134] and biosensing agents,[135,136] as well as novel nano-structures[137] and devices.[138] Methods for controlling the number and orientation of oligonucleotides and peptides at nanoparticle surfaces have been established,[138] but it remains challenging to create nanoparticle-protein assemblies with native-like protein structure and function.[139] One emerging paradigm is a thermophilic ferritin protein[140,141] whose 24 self-assembling four-helix bundles maintain native stoichiometry and secondary structure when encapsulating a single 5-nm gold nanoparticle (AuNP).[50–52] However, the assembly configuration in solution (i.e. protein quaternary structure) remains unknown because conventional methods for characterizing protein structure, such as X-ray crystallography,[105] are not suitable for liquid-phase protein-nanoparticle conjugates. Here, we demonstrate a non-perturbing method using a graphene microelectrode[142] for structural-functional analysis of an ordered AuNP-ferritin protein assembly that differs substantively from an unstructured protein corona. Ferritin is a multimeric iron-storage protein comprising 24 identical protein subunits and featuring a large (~8-nm) interior compartment separated from the exterior solution by a protein shell. The *Archaeoglobus fulgidus* ferritin (AfFtn) used here is a unique archaeal ferritin that forms a tetrahedral arrangement of its four-helix-bundle subunits, yielding four wide (4.5-nm), triangular pores spanning the 2-nm protein shell[49] (Figure 3.1a). Stoichiometric addition of 5-nm gold nanoparticles (AuNPs) to disassembled apo-AfFtn induces AfFtn assembly around individual AuNPs capped with bis(*p*-sulfonatophenyl)phenylphosphine (BSSP),[50–52] while maintaining its native thermal stability, stoichiometry, ferroxidase

activity, and secondary structure.[51] Charge flowing from the AuNP through ferritin pores transfers into the graphene microelectrode and is recorded by an electrometer. The measurements are consistent with a pore diameter of 4.5-nm, providing evidence that ferritin maintains native-like quaternary structure when complexed with AuNP. This work demonstrates a new tool for probing the nano-bio interface, and highlights the design and characterization of nanoparticle-protein assemblies with tunable ionic conductivity and chemical reactivity.

3.2 Results and Discussion

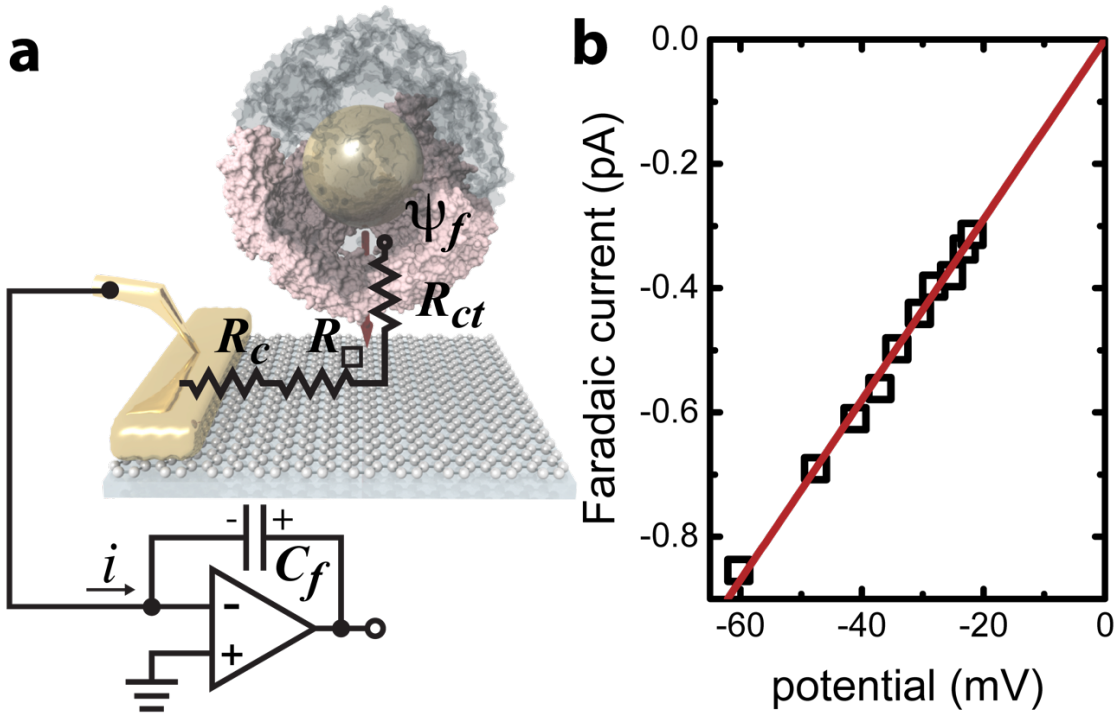

Figure 3.1. Graphene microelectrode setup. a) Schematic of the setup for measuring spontaneous Faradaic charge transfer across a pore to a graphene microelectrode in buffer solution and circuit diagram. b) Faradaic current as a function of electrostatic potential in the buffer solution above graphene. The red line is a linear fit to the data.

A graphene microelectrode was used to quantify Faradaic current through a ferritin-AuNP assembly and to differentiate between open- and closed-pore forms of the AfFtn shell. The experimental setup (Figure 3.1a) consisted of a graphene-based microelectrode connected to the inverting input of an electrometer[142] (Keithley 6517a). The electrostatic potential above a protein assembly in fluid, ψ_f, drives a sub-picoampere Faradaic current, i, through the series resistance of the charge-transfer at the graphene-solution interface[142] (R_{ct} ~ 100 GΩ), the graphene sheet ($R_{\square}$ ~ 10^2 – 10^3 Ω/□), and the graphene-gold contact[143] (R_c ~ 10 Ω). Transferred charge accumulates on the feedback capacitor and is read out on the electrometer. Because there is no extrinsic bias voltage between the solution and the microelectrode, heat dissipation (aW μm^{-2}) and electrical perturbation (~pA) to the protein structure[144] are minimized.

Detecting AfFtn Disassembly via Graphene Microelectrode

To interrogate our AfFtn-AuNP system, we first recorded the buffer response. The Faradaic current i is proportional to the potential ψ_f: $i = \psi_f / R_{ct}$. We applied a phosphate buffer solution to the graphene microelectrode and measured the Faradaic current while the electrostatic potential above the graphene surface was tuned by varying the buffer ionic strength c (Figure 3.1b). The variation of ψ_f with ionic strength was inferred from the Grahame equation for the electric double layer.[145] The fit to the data corresponds to a constant charge-transfer resistance R_{ct} = 69 ± 2 GΩ, and the fit passes through the origin as expected (0.6 ± 0.9 fA).

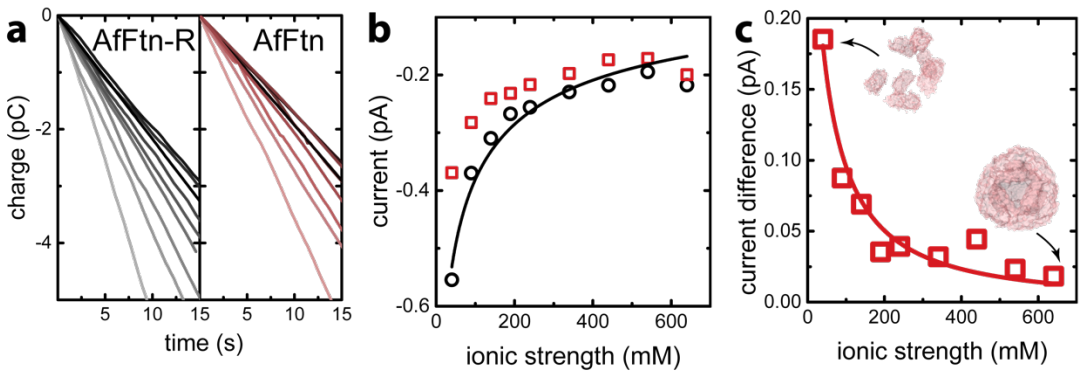

Figure 3.2. Graphene microelectrode can distinguish between assembled and disassembled ferritin. a) Time trace of the charge transfer between a graphene microelectrode and mutant *A. fulgidus* E65R ferritin solution (AfFtn-R), and wild-type *A. fulgidus* ferritin solution (AfFtn). The ionic strength of the solution increases as the grey-level of the data increases. b) Faradaic current for AfFtn-R (black circles) and AfFtn (red squares) based on the data in panel a). The black curve is a fit to the data for AfFtn-R using Equation 3.2. c) Faradaic current difference for AfFtn compared to AfFtn-R; the red curve is a fit based on Equation 3.3.

We next recorded a baseline response for assembled AfFtn. We measured the Faradaic current of an AfFtn mutant (E65R, termed AfFtn-R), which remains a 24mer even in low ionic strength solution (see Chapter 2). The solution (200 µL; 0.6 µM) was applied to the microelectrode, and a sparse layer of non-specifically bound protein allowed to form and equilibrate (Figure 3.3).

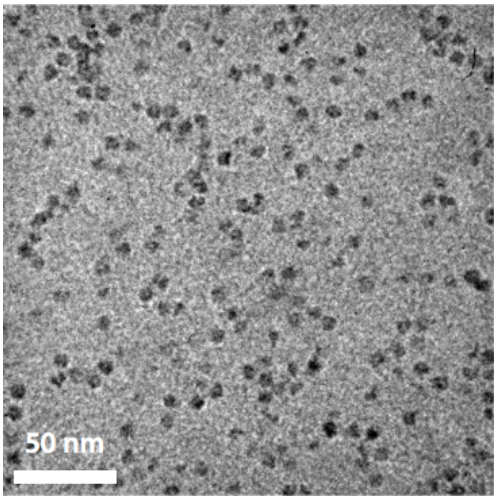

Figure 3.3. TEM image of ferritin non-specifically adsorbed on graphene. The light gray background is a sheet of monolayer graphene. Dark dots are individual ferritin cages.

As the ionic strength of the solution was varied from 40 mM to 640 mM, a 15-sec time trace of Faradaic charge transfer (Figure 3.2a) for AfFtn-R or AfFtn was used to extract the corresponding Faradaic current (Figure 3.2b). The solutions showed nearly identical Faradaic current at high ionic strength where both ferritins form stable 24mer assemblies, but the currents differed significantly at low ionic strength, where only AfFtn disassembles into dimers. The measured current for the AfFtn-R solution (black circles in Figure 3.2b) and the Faradaic current difference between the solutions of AfFtn and AfFtn-R (Figure 3.2c) are well explained by models based on known properties of the electric double layer and AfFtn assembly.

The Grahame equation[145] can be written as:

$$\psi_f = \frac{2k_{\mathrm{B}}T}{e}\sinh^{-1}\left(\frac{\sigma_s}{8\varepsilon\varepsilon_0 k_{\mathrm{B}}Tc}\right) \tag{3.1}$$

where k_B is Boltzmann's constant, T the absolute temperature, e the electronic charge, ε (ε_0) the relative (vacuum) permittivity, and σ_s the areal charge density in the solution above the graphene, and c the solution ionic strength. This leads to:

$$i = \frac{-1}{R_{ct}}\cdot\frac{2k_{\mathrm{B}}T}{e}\sinh^{-1}\left(\frac{\sigma_s}{8\varepsilon\varepsilon_0 k_{\mathrm{B}}Tc}\right) \tag{3.2}$$

The data in Figure 3.2b are well fit by Equation 3.2. The best fit values for $R_{\mathrm{ct,24mer}}$ and $\sigma_{\mathrm{d,24mer}}$ are 232 ± 74 GΩ and -0.07 ± 0.03 C m^{-2}, respectively. Compared to the fit values obtained for an experiment conducted in pure phosphate buffer (R_{ct}= 65 ± 3 GΩ, σ_{d}=-0.031 ± 0.003 C m^{-2}), there is an increase of the negative charge areal density due to the negative charge carried by AfFtn-R, accompanied by an increase in the charge transfer resistance due to the inhibition of charge communication by charged AfFtn-R

molecules.[146,147] Given the measured areal number density of non-specifically adsorbed ferritin on graphene, ~3500 μm^{-2} (Figure 3.3), the effective negative charge carried by each AfFtn-R 24mer is ~40, smaller than the value estimated by the pK_a values of the residues of AfFtn-R, ~110. This is not surprising as charges on ferritin far from the graphene should be screened by ions in solution.[148]

The Faradaic current measured for AfFtn solution differs significantly from that for AfFtn-R solution. Unlike AfFtn-R, which remains assembled across the range of ionic strengths tested, AfFtn disassembles into dimers at low ionic strength with a portion of $\frac{K/c}{1+K/c}$, where K is the dissociation constant for AfFtn.[50] The inverse of the charge transfer resistance $1/R_{\mathrm{ct}}$ and the surface charge density σ_{s} for the graphene/AfFtn solution interface are the sum of these quantities for the dimers, $1/R_{\mathrm{ct,dimer}}$ and $\sigma_{\mathrm{s,dimer}}$, and those for the 24-mers, $1/R_{\mathrm{ct,24mer}}$ and $\sigma_{\mathrm{s,24mer}}$, weighted by $\frac{K/c}{1+K/c}$ and $\frac{1/c}{1+K/c}$, respectively. The current difference can then be written as:

$$\Delta i = \frac{2k_{\mathrm{B}}T}{eR_{\mathrm{ct}}}\sinh^{-1}\left(\frac{\sigma_{\mathrm{s}}}{8\varepsilon\varepsilon_0 k_{\mathrm{B}}Tc}\right) - \frac{2k_{\mathrm{B}}T}{eR_{\mathrm{ct,24mer}}}\sinh^{-1}\left(\frac{\sigma_{\mathrm{s,24mer}}}{8\varepsilon\varepsilon_0 k_{\mathrm{B}}Tc}\right) \tag{3.3}$$

The measured current for the AfFtn-R solution is well fit by Equation 3.2 with best fit values of R_{ct} (232 ± 74 GΩ) and σ_s (-0.07 ± 0.03 C m^{-2}), consistent with our earlier report on graphene microelectrodes in buffer.[142] The Faradaic current difference between the solutions of AfFtn and AfFtn-R (Figure 3.2c, Equation 3.3) can be explained using the above model. The best fit value for K = 210 ± 60 mM derived from this model is in excellent agreement with the value obtained by liquid chromatography[50] (K = 200 mM).

Exploring AfFtn Assembly on AuNP Surface

To interrogate AfFtn assembly on AuNPs, we measured the real-time Faradaic charge transfer for solutions of AuNPs (I_{AuNP}, see Figure 3.4a), and of AuNP-ferritin assemblies based upon the wild-type ferritin AfFtn and a recently identified mutant, AfFtn-AA (K150A/R151A), which features an octahedral arrangement of its subunits with "closed" (< 1 nm) pores.[116] Representative data are shown in Figure 3.4b. When an AuNP is encapsulated in the closed-pore AfFtn-AA assembly, the AuNP surface should be less accessible compared to when AuNPs are encapsulated in AfFtn. The AfFtn-AA-containing sample should therefore have less charge transfer compared to AfFtn.

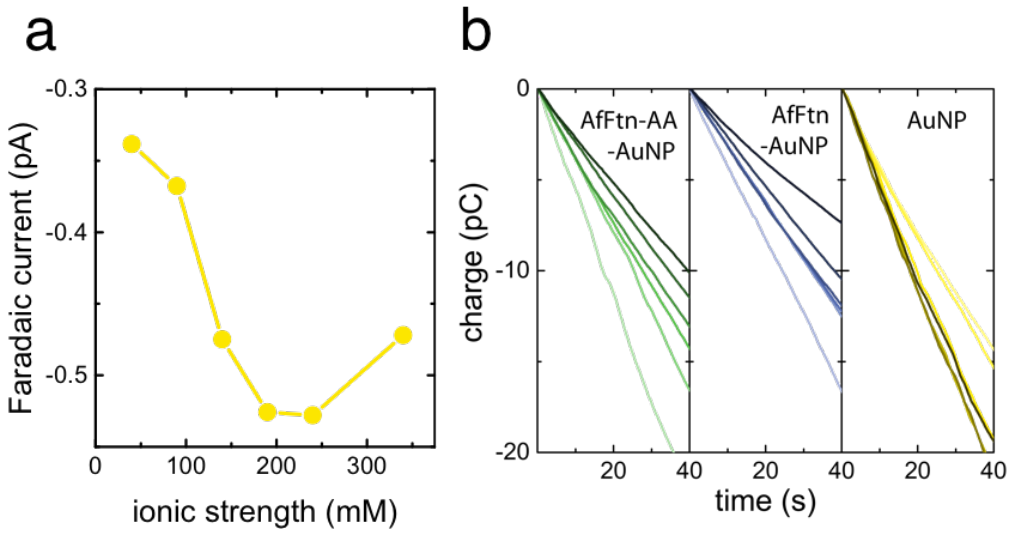

Figure 3.4. Faradaic current and charge transfer for AuNP-containing samples. a) Faradaic current for AuNP as a function of ionic strength by graphene electrodes. The Faradaic current is negative and reaches its maximum magnitude for ionic strength ~240 mM due to competing effects of AuNP-adsorption and ionic screening. b) Real-time charge transfer for AfFtn-AA-AuNP, AfFtn-AuNP, and AuNP measured by graphene electrodes.

We used the Faradaic current of AfFtn-R as the baseline for assembled (24mer) ferritin, which leads to several strict requirements for accurate quantification of trans-pore current. First, ferritin must remain assembled with the AuNP enclosed. This is satisfied as

24mer assemblies of both AuNP-AfFtn and AuNP-AfFtn-AA are stable in the range of ionic strengths tested[51] (40 – 340 mM). Second, all AuNPs must be encapsulated by ferritin with no free AuNPs in solution. As shown in Figure 3.5, more than 99% AuNPs were enclosed in a ferritin protein shell as confirmed by TEM and gel electrophoresis. We also verified that AuNPs were stable in the range of ionic strengths used without aggregation (Figure 3.6).

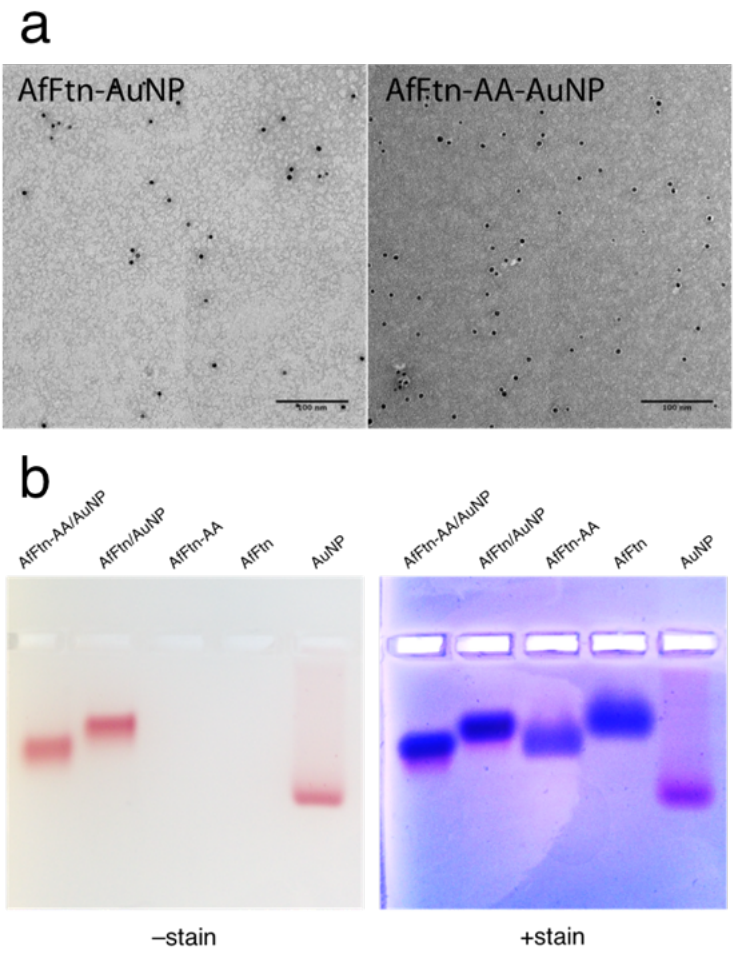

Figure 3.5. Evidence of AuNP encapsulation. a) The TEM images for AfFtn-AuNP solution and AfFtn-AA-AuNP solution. The black dots are AuNPs. All the AuNPs are enclosed by a white, halo-like ring, which corresponds to the protein shell. b) Native gel electrophoresis also confirms encapsulation. Gel was run at 100 V for 20 min. Overlapping red AuNP bands and blue protein bands (+stain gel) indicate encapsulation.

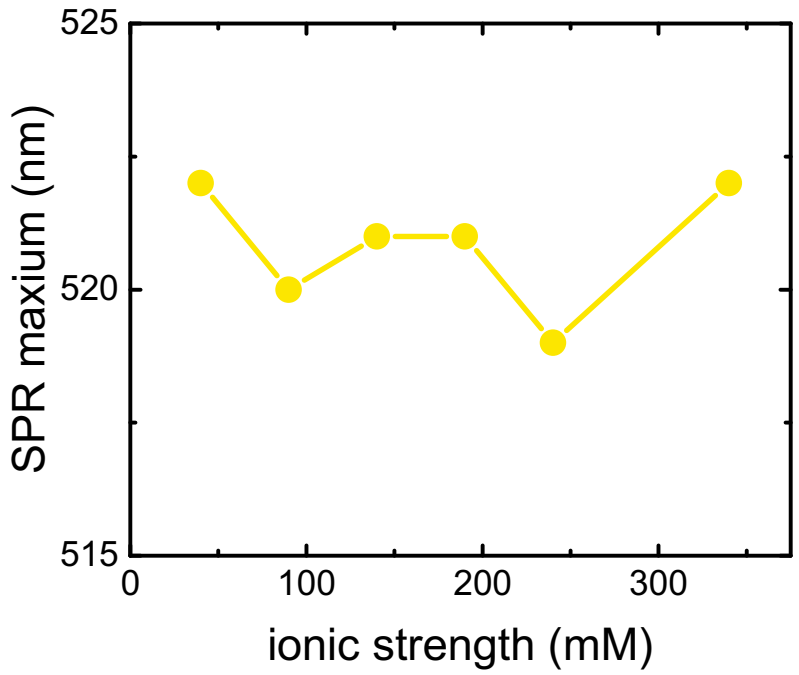

Figure 3.6. AuNP stability with varying ionic strength. Maximum of the surface plasmon resonance peaks measured for gold-nanoparticle PBS solutions with ionic strength ranging from 40 mM to 340 mM.

To quantify Faradaic current contributed by enclosed AuNPs, we calculated the difference between the current for AuNP-AfFtn (AuNP-AfFtn-AA), $I_{\text{AuNP-AfFtn}}$ ($I_{\text{AuNP-AfFtn-AA}}$) and the baseline ($I_{\text{AfFtn-R}}$): $\Delta I = I_{\text{AuNP-AfFtn}} - I_{\text{AfFtn-R}}$ ($I_{\text{AuNP-AfFtn-AA}} - I_{\text{AfFtn-R}}$), with results plotted in Fig. 3.7a. For AuNP-AfFtn, ΔI varied by ~0.12 pA through the range of ionic strength, with a minimum at ~240 mM. For AuNP-AfFtn-AA, ΔI was much smaller and essentially constant at -0.020 ± 0.005 pA. For AuNP-AfFtn, the plot of ΔI *vs.* I_{AuNP} (Fig. 3.7b) followed a linear trend with slope $a = 0.59 \pm 0.05$, suggesting that the efficiency of Faradaic charge transfer *via* AuNPs enclosed in open-pore AfFtn is ~60% of that for bare AuNPs. In contrast, for AuNP-AfFtn-AA, we found a slope $a = 0.03 \pm 0.03$, suggesting that the presence of closed pores completely suppresses this charge transfer pathway.

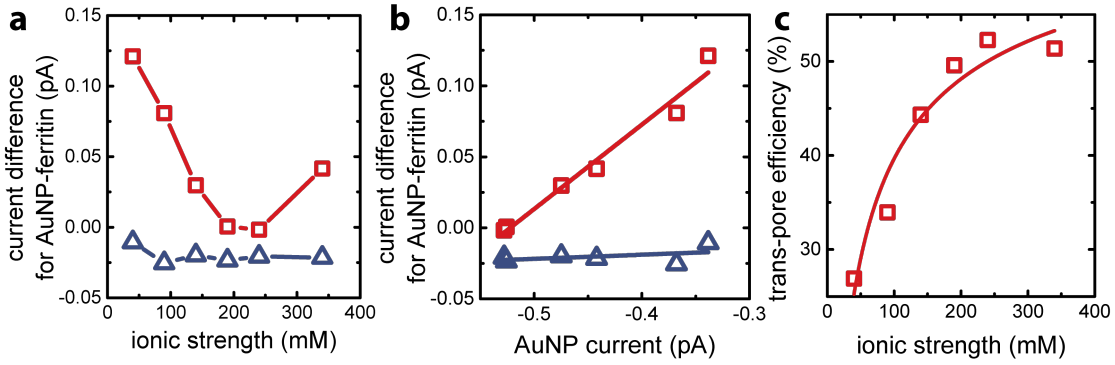

Figure 3.7. Microelectrode can distinguish between closed and open pore AfFtn in presence of AuNPs. a) Difference in Faradaic current for solutions of AuNP-enclosed in *A. fulgidus* mutant ferritin K150A/R151A (AuNP-AfFtn-AA, blue triangles) and AuNP-enclosed in wild-type ferritin (AuNP-AfFtn, red squares) compared to the baseline current set by a solution of E65R ferritin (AfFtn-R). b) Faradaic current difference for AuNP-AfFtn-AA (blue triangles) and AuNP-AfFtn (red squares) as a function of the Faradaic current for AuNP. The lines are linear fits to the data. c) Charge-transfer efficiency ξ as a function of ionic strength fitted by the formula for the model based on electrical double layer.

This analysis suggests that the Faradaic current carried by the ferritin-AuNP system has two components: i) pore-mediated current *via* the AuNP and ii) current associated with the protein shell, quantified by $I_{\text{AfFtn-R}}$. We define the trans-pore efficiency $\xi(c) = |aI_{\text{AuNP}}(c)|/(|aI_{\text{AuNP}}(c)| + |I_{\text{AfFtn-R}}(c)|)$ to quantify the fraction of the total current carried by the enclosed AuNPs. The efficiency increases monotonically by ~100% as the ionic strength increases from 40 mM to 340 mM (Figure 3.7c). In contrast to molecular diffusion through the pore, which is driven by a concentration gradient, the Faradaic current depends on the gradient of the electrostatic potential. Thus, negative charge at the edge of the AfFtn pores can suppress the (negative) Faradaic current *via* the enclosed AuNP over length scales given by the Debye screening length $\lambda_{\text{D}}[nm] = 0.304/\sqrt{c[M]}$. Thus we expect that the efficiency will be affected by ionic strength approximately as $\xi = A(4.5 - k\lambda_{\text{D}}[\text{nm}])^2$ where A is a factor scaling area to efficiency, 4.5 nm is the pore diameter for AfFtn, and k is ~ 1. The charge-transfer efficiency is well fit by this equation

(Fig. 3.3d) with best fit value $k = 1.2 \pm 0.1$. This experiment demonstrates the capability of graphene microelectrode measurements to differentiate between open- and close-pore structures in ferritin-nanoparticle assemblies, confirms the accessibility of enclosed AuNPs, and provides strong evidence that the AfFtn pore maintains a native-like structure in the presence of the enclosed AuNP.

Conventional Catalysis Methods Comparison

For confirmation and comparison, we used conventional catalysis methods to differentiate between wild-type AuNP-AfFtn and AuNP-AfFtn-AA: dehalogenation of a bisiodinated boron dipyrromethene derivative (I-BODIPY) and reduction of 4-nitrophenol. More AuNP surface area should be exposed in the AfFtn-containing sample compared to AfFtn-AA, and should therefore have greater AuNP catalytic activity. The reactions were monitored by different spectroscopic techniques: an increase in fluorescence at 507 nm was observed for the I-BODIPY dehalogenation reaction,[149] and a decrease in absorbance at 400 nm was observed for the nitrophenol reduction.[150]

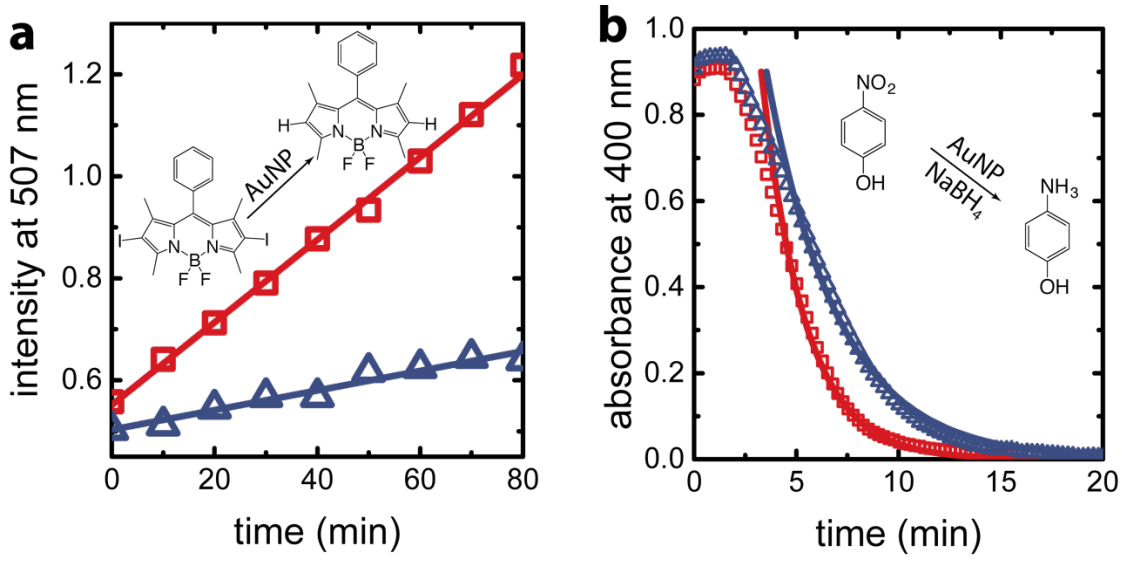

Figure 3.8. Catalysis assays distinguish between AfFtn and AfFtn-AA. a) Real-time fluorescence intensity of I-BODIPY dehalogenation catalyzed by AuNP-AfFtn-AA and AuNP-AfFtn solutions. b) Real-time UV-visible spectroscopy of reduction of 4-nitrophenol catalyzed by AuNP-AfFtn-AA and AuNP-AfFtn solutions. The solid curves are fits based on first-order kinetics. The corresponding catalytic reactions are shown in panels a-b.

As shown in Figure 3.8a, the rate of increase in the fluorescence intensity in the AuNP-AfFtn solution (0.0081 ± 0.0002 A.U./min) is approximately 4 times larger than the AuNP-AfFtn-AA solution (0.0019 ± 0.0002 A.U./min). For the 4-nitrophenol reduction, AuNP-AfFtn had roughly twice the catalytic rate constant, $k = (7.4 \pm 0.7)\ \text{x}10^{-3}\ \text{s}^{-1}$ vs. $(4.0 \pm 0.3)\ \text{x}10^{-3}\ \text{s}^{-1}$ for AuNP-AfFtn-AA (Figure 3.8b). Neither ferritin contributed to the catalytic activity as shown in Figure 3.9.

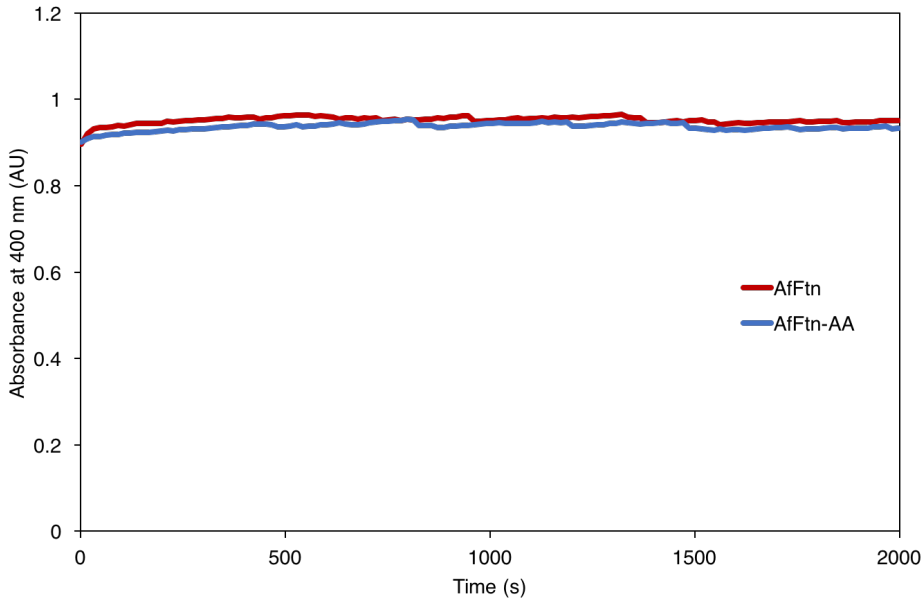

Figure 3.9. Reduction of 4-nitrophenol in the presence of AfFtn (red) or AfFtn-AA (blue). Neither protein shows any change in A_{400}, indicating no catalytic activity.

For the catalytic assays, the difference in signal for AuNP-AfFtn versus AuNP-AfFtn-AA is only four-fold and two-fold for the I-BODIPY and 4-nitrophenol reactions, respectively. In contrast, the difference between AuNP-AfFtn and AuNP-AfFtn-AA for the microelectrode is nearly 20-fold. Thus, our methodology based on graphene microelectrode is comparatively rapid (seconds versus tens of minutes), enables a quantitative estimate of the pore diameter through direct charge-transfer measurement through the protein shell, and overcomes limitations in sensitivity imposed by the AuNP catalytic reactions.

3.3 Conclusions

In summary, we have developed a graphene microelectrode device as a sensitive tool for structure-function analysis of AuNP-ferritin assemblies in solution. This all-electronic method has multiple advantages for identifying protein pores compared to

conventional AuNP catalysis methods, and it provides a direct measurement of the pore-mediated charge-transfer process. Our approach provides a way to explore protein structure at nm-scale and, more broadly, to explore interactions of biomolecules with inorganic nanomaterials in complex biofluids, systems shown to offer significant promise in bio-imaging, sensing, catalysis and templated nanoparticle synthesis.

3.4 Experimental Procedures

Graphene growth. Copper foil (99.8% purity) was loaded into a four-inch quartz tube furnace and annealed for 30 min at 1050 °C in ultra-high-purity (99.999%) hydrogen atmosphere (flow rate 80 sccm; pressure 850mT at the tube outlet) for removal of oxide residues. Graphene was deposited by low-pressure chemical vapor deposition (CVD) using methane as a precursor (flow rate 45 sccm) at 1050 °C for 60 min.

Graphene device fabrication. The graphene-copper growth substrate was coated with 500-nm layer of poly(methyl methacrylate) (PMMA, MicroChem), and the PMMA-graphene film was floated off the surface by immersion in 0.1 M NaOH solution with the graphene-copper growth substrate connected to the cathode of a power supply. The PMMA-graphene film was transferred onto a 300 nm SiO_2/Si wafer with an array of 5 nm/40 nm Cr/Au contact electrodes that were previously fabricated using photolithography. Al_2O_3 (5 nm) was deposited on the whole wafer as a sacrificial layer, and 50 μm × 100 μm graphene microelectrodes were defined by photolithography with photoresist PMGI (MicroChem) and S1813 (MICROPOSIT) and oxygen plasma etching. The Al_2O_3 layer on top of the microelectrode areas was removed by the basic photoresist developer MIF-319 (MICROPOSIT). After removal of the photoresist residues with 1165

(MICROPOSIT), another passivation layer of photoresist SU-8 (MicroChem) was applied to the device, and the wells exposing the microelectrodes were defined via photolithography.

Ferritin mutagenesis. The pAF0834 plasmid containing the AfFtn gene was provided by the laboratory of Dr. Eric Johnson at the California Institute of Technology. AfFtn-R was made by site-directed mutagenesis using the Stratagene QuikChange kit. The primers were obtained from Integrated DNA Technologies:

sense (5′-3′) GATTTCGTTTCCCGTCGCGGTGGCCGTG

antisense (5′-3′) CACGGCCACCGCGACGGGAAACGAAATC

The mutated cDNA was transformed into XL1-Blue Supercompetent *E. coli* cells (Stratagene) according to the manufacturer's protocol. The plasmid was isolated using a QIAprep Spin Miniprep kit (Qiagen). All sequencing was performed by the University of Pennsylvania DNA Sequencing Facility. The AfFtn-AA plasmid was purchased from DNA2.0 and transformed the same as AfFtn-R and wt AfFtn.

Ferritin expression/purification. Production and purification of AfFtn and mutants was performed as previously published,[52] with some modifications. The plasmid was transformed into BL21-Codon Plus(DE3)-RP competent *E. coli* cells (Stratagene) in TB medium (1 L containing 100 mg ampicillin, 35 mg chloramphenicol) at 37 °C with shaking at 225 rpm until OD_{600} ~0.8 was reached. The cells were induced with 1 mM isopropyl β-D-1-thiogalactopyranoside (IPTG, Lab Scientific) and continued incubating for 4 h. Cells were centrifuged and frozen, followed by resuspension in buffer (20 mM phosphate, 20 mM NaCl, pH 7.6) with an EDTA-free protease inhibitor cocktail tablet (ThermoFisher Scientific). Cell lysis was performed by treatment with lysozyme and sonication, followed

by nuclease treatment (15 min at room temperature, Pierce universal nuclease, ThermoFisher Scientific). The lysate was heat shocked to remove most endogenous *E. coli* proteins (10 min at 80 °C), buffer exchanged to induce ferritin assembly (2.5 M NaCl, 2 mM EDTA, 20 mM phosphate, pH 7.6), and purified further using size exclusion chromatography (HiLoad 16/60 column, GE Healthcare). The purity of the protein was determined to be >95% by denaturing PAGE gel (4-15% Tris-HCl, Mini-Protean TGX gel), as seen in Figure 3.10. Protein concentration was determined using the Bio-Rad Protein Assay (based on the Bradford method), using bovine gamma globulin as the standard. Proteins were also characterized by MALDI-TOF-MS (Figure 3.11).

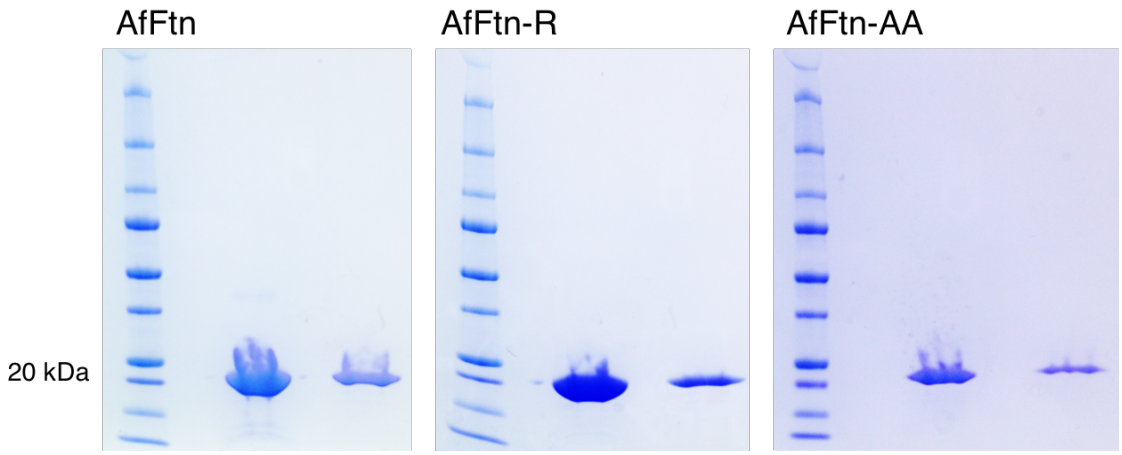

Figure 3.10. Denaturing PAGE shows pure protein for all three samples, with monomer MW approximately 20 kDa, as expected.

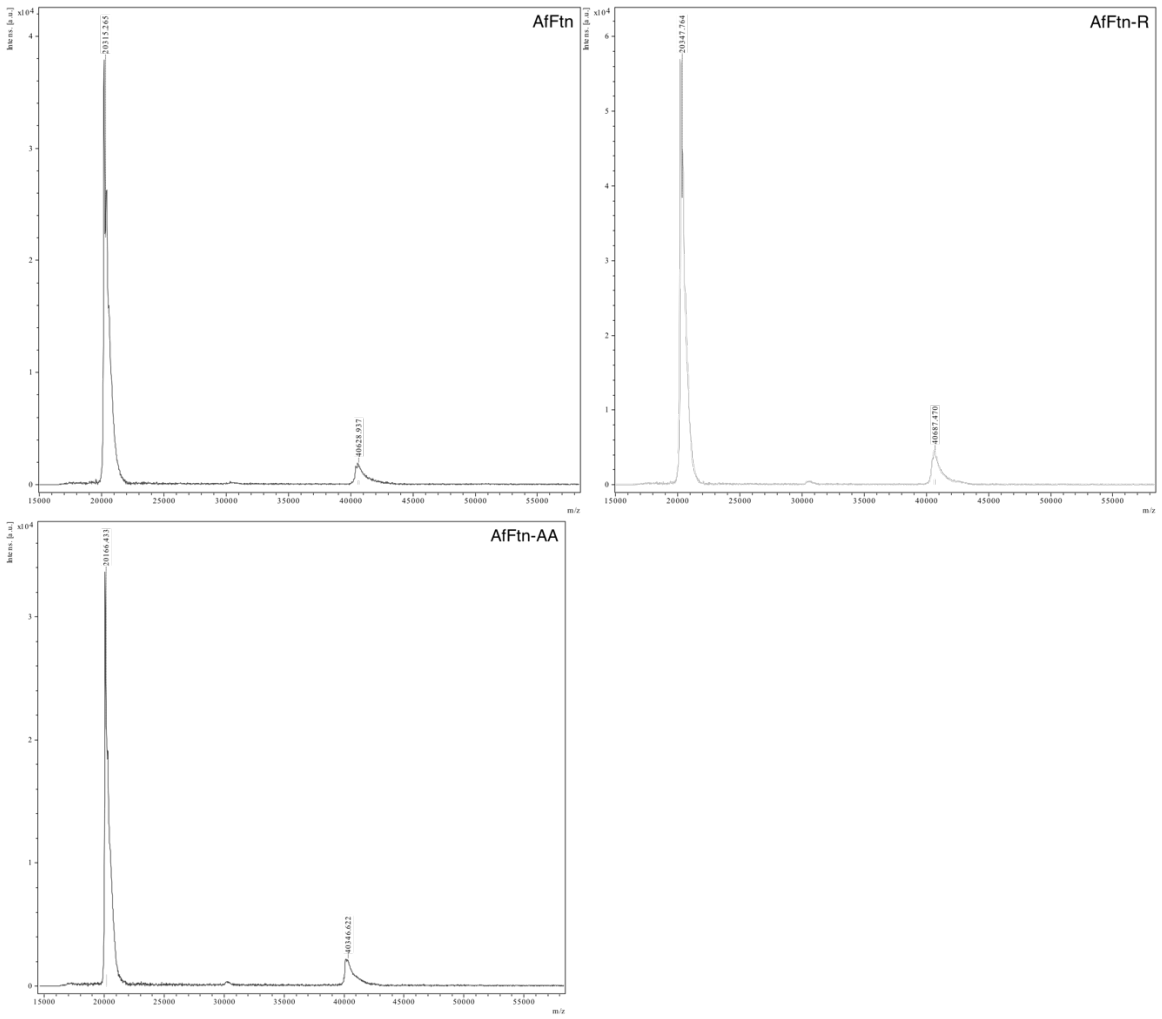

Figure 3.11. MALDI-TOF-MS for all proteins. Measured mass for monomer (expected): AfFtn 20315.3 (20316.1 Da), AfFtn-R 20347.8 (20343.1 Da), AfFtn-AA 20166.3 (20173.9 Da). Peaks at ~40 kDa correspond to dimer. Sinapinic acid was used as a matrix, and linear-positive mode was used as the method.

AfFtn solution and AfFtn-R solution preparation. Protein samples were prepared at 10 μM concentration in phosphate buffer (20 mM phosphate, pH 7.6), using NaCl to vary ionic strength (40, 90, 140, 190, 240, 340, 440, 540, 640 mM). To ensure accurate ionic strengths, samples were buffer exchanged on a Zebaspin column (ThermoFisher Scientific) equilibrated with the appropriate buffer. Samples were incubated overnight at 4 °C to allow for equilibration.

AuNP-AfFtn solution and AuNP-AfFtn-AA solution preparation. Citrate-capped 5 nm AuNPs were purchased from Ted Pella. The citrate was exchanged for bis(*p*-sulfonatophenyl)phenylphosphine (BSPP, Strem Chemicals) as described previously.[51] For device measurements, 1 mL samples were prepared at 0.3 mg/mL protein, 0.6 μM 5 nm AuNP-BSPP in 20 mM phosphate pH 7.6 and equilibrated at room temperature for 48 h with gentle agitation to ensure encapsulation. Protein NP samples were buffer-exchanged into various ionic strengths (40, 90, 140, 190, 240, 340 mM) using 10DG columns (Bio-Rad) equilibrated with the appropriate phosphate buffer. The 10DG column also helped ensure that only encapsulated AuNPs remained in the samples, as confirmed by TEM and native gel electrophoresis (Figure 3.5). The first two fractions were combined, and AuNP concentration was verified by UV-vis spectroscopy. Because bare AuNPs cannot elute on a 10DG column, buffer exchange for the AuNP samples without protein was done using Zebaspin columns equilibrated at the same ionic strengths. All samples were diluted to 2 mL to match the lowest concentration sample (20 nM). All samples were measured on the same device on the same day they were prepared, to minimize bulk AuNP aggregation.

Preparation of I-BODIPY. I-BODIPY was prepared following the method of Zuber et al.[151] A dark red solid product was obtained with a mass of 31.8 mg (69.7% yield). ^{1}H NMR (CD_2Cl_2): 7.54 (3H, m), 7.29-7.28 (2H, m), 2.62 (6H, s), 1.40 (6 H, s). Mass was verified using MALDI-TOF-MS with α-cyano-4-hydroxycinnamic acid (CHCA) as matrix. For characterization data, see Figure 3.12.

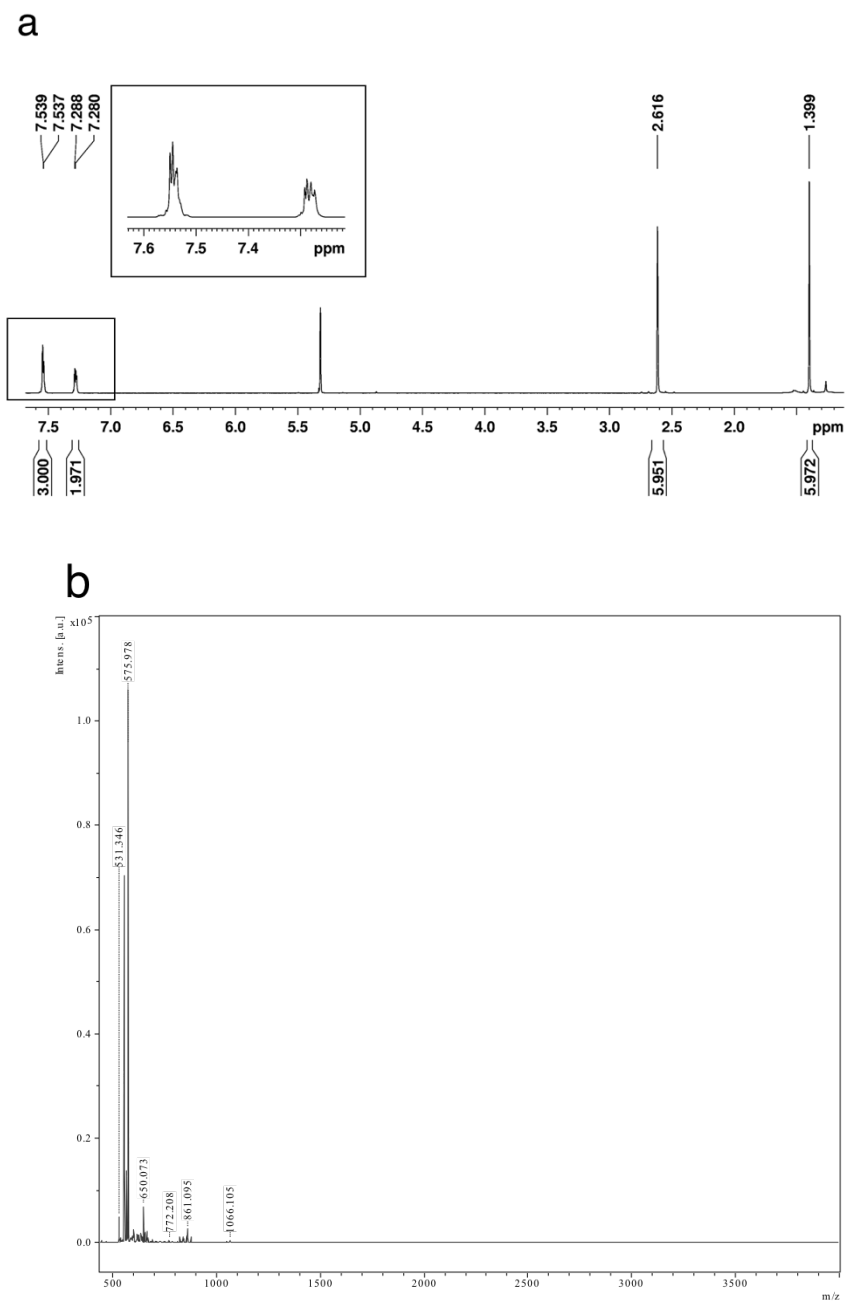

Figure 3.12. I-BODIPY characterization. a) ^{1}H NMR spectrum of I-BODIPY in CD_2Cl_2. b) MALDI-TOF-MS spectrum of I-BODIPY using CHCA as matrix. Peaks at 531.346, 650.073, 772.208, 861.095, 1066.105 m/z correspond to matrix. Observed sample mass is 575.978, expected is 575.954.

Fluorescence measurements. For the AuNP-catalyzed dehalogenation reaction, 10 nM AuNP-AfFtn and 1 μM I-BODIPY were mixed in 50 mM HEPES buffer (pH 7.0). Steady-state fluorescence was monitored using a Varian Cary Eclipse fluorimeter, with PMT detector voltage at 800 V, excitation wavelength of 465 nm, and temperature of 25 °C.

4-Nitrophenol reduction. A solution of 5 nM AuNP-AfFtn and 50 μM 4-nitrophenol (Fluka) was mixed in a cuvette. Freshly prepared aqueous $NaBH_4$ (Fluka) was added to a final concentration of 2.5 mM and total sample volume of 1 mL. Absorbance at 200—1100 nm was measured every 15 s at 25 °C using an Agilent 8453 UV-visible spectrometer. To determine the rate constant k, the data were fit to a first-order reaction, after subtracting the induction time (197 s):

$$\text{Abs} = \varepsilon[A]_0 e^{-kt}$$

where Abs is the measured absorbance, ε the extinction coefficient of 4-nitrophenol at 400 nm (18000 M^{-1} cm^{-1}), $[A]_0$ the initial concentration of 4-nitrophenol (50 μM), and t the time.

3.5 Acknowledgments

J.P. and A.T.C.J. acknowledge the support from the Defense Advanced Research Projects Agency (DARPA) and the U.S. Army Research Office under grant number W911NF1010093. K.W.P. and I.J.D. acknowledge support from the NSF (PD 09-6885). J.G.S. and I.J.D. acknowledge support from NSF CHE-1508318. J.G.S. acknowledges additional support from the Penn Laboratory for Research on the Structure of Matter (NSF DMR-1120901). This work used the Extreme Science and Engineering Discovery

Environment (XSEDE), which is supported by National Science Foundation grant number ACI-1053575, under grant number TG-CHE110041. MALDI-TOF-MS was purchased with NSF grant CHE-0820996. T.L.H. was supported by the REU program of the LRSM (Penn MRSEC) through NSF grant DMR-1062638 Penn-REU summer fellowship, NSF DMR 11-20901.

CHAPTER 4: Controlling Gold Nanoparticle Seeded Growth in Thermophilic Ferritin Protein Templates

The content of this chapter has been submitted for publication. It has been adapted here:

Reprinted with permission from Pulsipher, K.W.; Honig, S.; Deng, S.; Dmochowski, I.J. Controlling Gold Nanoparticle Seeded Growth in Thermophilic Ferritin Protein Templates. **2017.** *Submitted.*

4.1 Introduction

Ferritins are hollow, multimeric proteins whose native function is the oxidation, mineralization, and storage of iron.[23] Because of their unique structure, ferritins can be used as mini-reactors to prepare inorganic nanoparticles (NPs) by reducing metal salts inside the protein cavity. In addition to iron, ferritins naturally bind other metals[152–156] and can also be redesigned to enhance metal ion binding.[48,108] Ferritin-templated NP synthesis can occur in room-temperature aqueous conditions, which is significantly more environmentally friendly compared to other conventional NP synthesis methods. Furthermore, protein-constrained growth offers potential advantages in controlling nanoparticle shape and size and can result in monodisperse samples. In 1991, Meldrum et al. presented the first examples of non-native inorganic NP synthesis inside ferritin, producing MnO_2, FeS, and uranyl oxyhydroxide cores.[157] Since that time, metallic cores of widely varying composition have been synthesized using ferritin, including semiconducting quantum dots,[158–160] metal oxide NPs,[161] noble metal NPs,[103,108,162–164] and magnetic NPs.[165–168] This wide range of protein-assisted reactions motivates the study of model ferritin systems, where the composition and presentation of polypeptides is well defined compared to many biologically controlled biomineralization reactions, e.g., the formation of shells and bone.

While ferritin provides an excellent nanoreactor for the formation of NPs, it has been challenging to restrict particle growth to the interior of the protein cage. Many amino acids such as histidine and cysteine can bind metal ions, generating multiple nucleation sites on the interior and exterior ferritin surfaces. Zhang et al.[163] demonstrated ferritin-aided AuNP growth on the surface of HSAF via reduction of $HAuCl_4^-$ with either $NaBH_4$ or 3-

(N- morpholino)propanesulfonic acid (MOPS). Without HSAF present, synthesized AuNPs were unstable, demonstrating the improved passivation by ferritin. TEM showed the AuNPs to be on the exterior protein surface, with average diameters of 3.6 ± 1.2 and 15.4 ± 4.5 nm for $NaBH_4$ and MOPS, respectively.

Ideally, NP formation should occur exclusively inside the ferritin cage, taking advantage of complete protein coating. Butts et al.[108] mutated human H ferritin (HuHFtn) to encourage interior particle growth by removing all histidines and cysteines (four per subunit) present on the outer protein surface (called H4). A second protein mutant (H8) was made from H4 by adding four interior-surface cysteine residues per monomer to further promote NP growth in the central cavity. Ag NPs were formed by addition of $AgNO_3$ in MOPS buffer, while illuminating with a 60 W bulb. To prepare AuNPs, $AuCl_3$ was added to ferritin in MOPS buffer, with formation of AuNPs complete in 1.5 h at room temperature. Samples were purified by centrifugation followed by desalting column to remove excess reagents and any large NPs growing outside ferritin. While wt, H4, and H8 samples all showed characteristic yellow/brown color indicating formation of AgNPs, only H8 contained particles that remained stable and exhibited an AgNP SPR band through chromatography purification. H8 was also the only protein that formed stable, non-aggregating AuNPs.

Another approach to ensuring particle growth within the cavity is not through changes to ferritin itself, but in removing excess Au ions through desalting before reduction. Fan et al.[169] demonstrated a two-step AuNP formation specifically inside HSAF. To generate small, uniform "seed" particles, $HAuCl_4$ was incubated with HSAF for 3 h, then desalted with a sizing column to remove excess gold ions, particularly gold ions that

were weakly coordinated to the HSAF exterior surface. Strong reducing agent $NaBH_4$ was then added to generate seed particles inside the HSAF cavity. After 3 h, additional $HAuCl_4$ and mild reducing agent ascorbic acid were added to further NP growth. After incubating overnight at room temperature, the solution was purified by size exclusion chromatography and ultracentrifugation through a sucrose gradient. The AuNPs were found to be exclusively within the protein cavity, had an average diameter of 6.3 ± 0.8 nm, and were mostly single crystalline.

We have demonstrated a hybrid technique[51] of encapsulating a 5-nm seed AuNP and performing in situ growth in the AfFtn cavity as shown in Figure 4.1. Addition of gold ions and reducing agent promoted AuNP growth. $HAuCl_4$ was added to AfFtn and incubated at room temp for 3 h. The solution was desalted using a sizing column to remove excess $AuCl_4^-$ and AfFtn surface-bound $AuCl_4^-$. Mild reducing agent ascorbic acid was added to reduce gold ions interacting with the AuNP surface. This process led to small, incremental growth. Two cycles led to AuNPs with an average diameter of 8.2 ± 1.9 nm, almost completely filling the ferritin cavity. Control experiments with AuNPs without protein present led to rapid precipitation, demonstrating the importance of the protein template in generating monodisperse, stable particles.

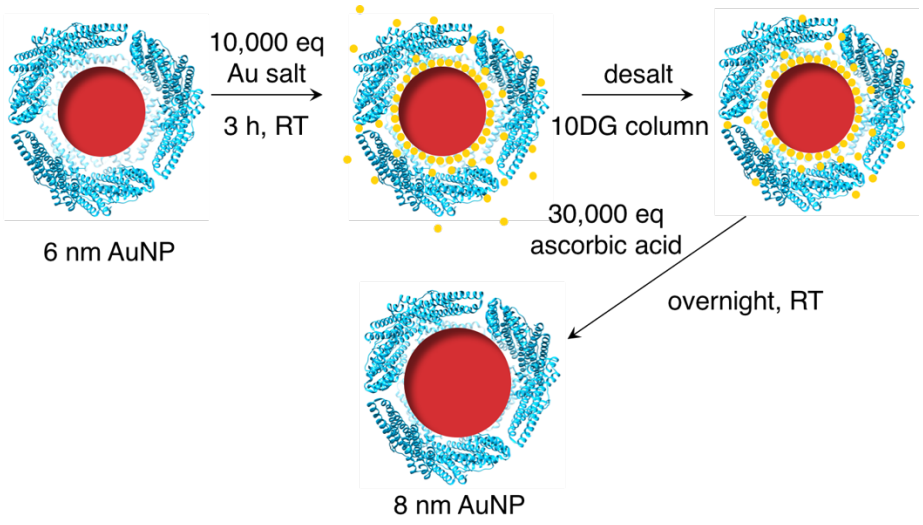

Figure 4.1. Templated growth scheme for AuNPs encapsulated within AfFtn. After addition of gold ions, the sample is desalted to remove excess reagent and encourage growth inside the cavity. Mild reducing agent ascorbic acid reduces gold ions on the surface of the NP, growing the AuNP to fill the protein cage.

AuNPs are most commonly prepared in ferritins using $HAuCl_4$ or $AuCl_3$ as the gold salt. Intrigued by the need for two rounds of seeded growth reaction in order to grow the AuNP to fill the AfFtn cavity, we decided to explore the role of the charge of the gold salt. Because the interior of AfFtn is negatively charged,[50] we hypothesized that electrostatic repulsion was preventing $HAuCl_4$ from entering the cavity in concentrations needed for significant particle growth. Shown in Figure 4.2, we used three gold salts with different charges in solution: $HAuCl_4$, $AuCl_3$, and Au(ethylenediamine)$_2Cl_3$. $HAuCl_4$ deprotonates in aqueous solution to form a variety of anionic species in the form of $[AuCl_{4-n}(OH)_n]^-$, where n = 0–4, depending on pH, chloride concentration, and oxidizing conditions.[170] $AuCl_3$, which exists as Au_2Cl_6 in crystalline form,[171] is initially neutral in solution. Electrospray ionization of aqueous gold(III) chloride produces a large variety of mononuclear clusters in the gas phase evidenced by mass spectrometry, e.g.,

$[AuCl_2]^+(H_2O)_n$ (n = 0-4), as well as dinuclear $[Au_2Cl_{5-x}OH_x]^+(H_2O)_n$ (x = 0-1) species.[172] However, on the short timescale of our seeded growth reaction, the dimeric neutral Au_2Cl_6 species likely predominates in aqueous buffer, pH 7.6. Finally, $Au(en)_2Cl_3$ loses its chloride counterions in water and has a +3 charge.[173]

We also compared the templating capabilities of AfFtn with bovine serum albumin (BSA), which does not form an ordered cage around the AuNP and can directly adsorb to the AuNP surface.[174] Previous studies using BSA to promote particle growth led to polydisperse Ag, Au, or Ag/Au alloy NPs.[175–177] We therefore expected that BSA in seeded growth reactions would be unable to control AuNP growth to the same extent as AfFtn. Finally, we compared wt AfFtn templating with a double mutant AfFtn-AA (K150A/R151A)[116] lacking the characteristic large pores, to determine whether the pores can facilitate molecular diffusion processes required for seeded nanoparticle growth.

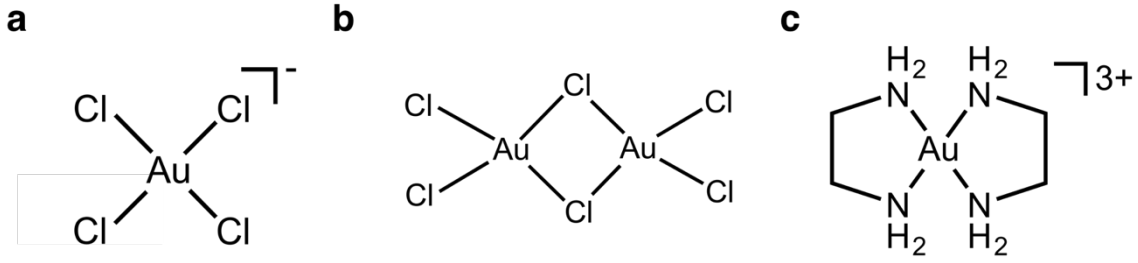

Figure 4.2. Predominant aqueous solution structures of gold complexes used. a) $AuCl_4^-$ b) Au_2Cl_6 c) $Au(ethylenediamine)_2^{3+}$

4.2 Results and Discussion

Effect of Gold Salt on Seeded Growth

We synthesized $Au(en)_2Cl_3$ following the method of Zhu et al.[173] and $HAuCl_4$ and $AuCl_3$ were used as received from Sigma Aldrich and Acros, respectively. We prepared

seeded growth samples following the procedure outlined in Figure 4.1, starting with pre-encapsulated AuNPs with an average diameter of 6.0, 6.1, or 6.3 nm, as measured by TEM. The addition of 10,000 eq gold salt was expected to grow the starting ~6 nm AuNP to a diameter of just over 8 nm, assuming 100% incorporation of gold salt into the AuNP. The resulting samples were characterized by TEM and UV-visible spectroscopy. TEM micrographs (Figure 4.3) showed monodisperse particles with average diameters between 6 and 8 nm for all AfFtn samples, with AuNPs from the $AuCl_3$ sample most closely matching the AfFtn inner cavity diameter. We calculated a % yield based on the expected particle volume change with addition of 10,000 eq gold salt. The differences among the samples were striking: only 10% of the gold atoms were incorporated into AuNPs using $HAuCl_4$, while 40% were incorporated using $Au(en)_2Cl_3$, and 70% for $AuCl_3$. BSA-templated samples were considerably more polydisperse, with somewhat larger particle diameters ranging from 7 to 9 nm. The larger particle "growth" is more likely due to particle aggregation, rather than greater deposition and reduction of gold ions. Some larger particles appeared by TEM to be slightly misshapen and resembled several conjoined particles, rather than single larger, spherical particles. Control experiments without either AfFtn or BSA present led to complete precipitation of the AuNPs for all Au ions tested, emphasizing the important role for protein stabilization.

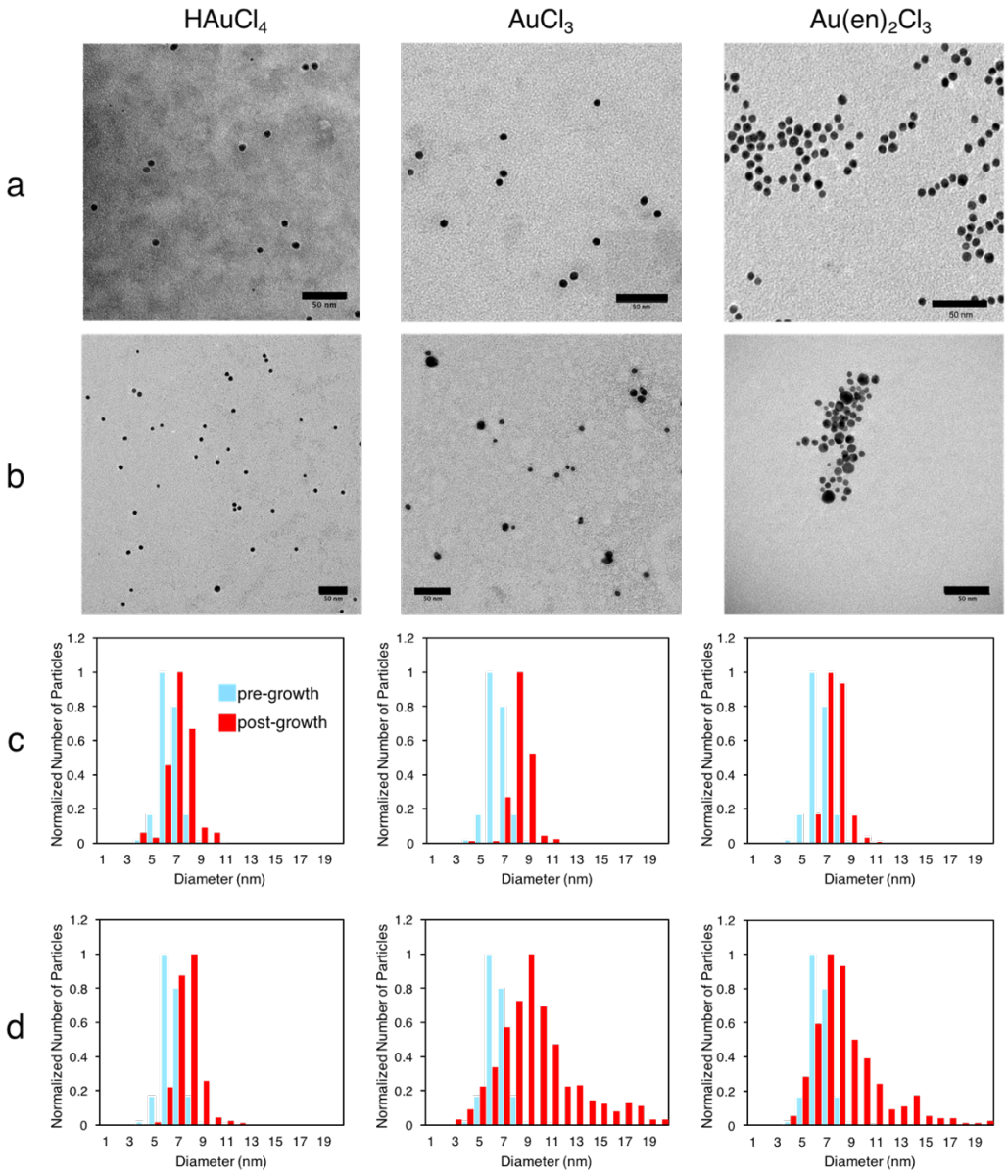

Figure 4.3. TEM micrographs post-growth. a) Representative AfFtn-AuNP micrographs. b) Representative BSA-AuNP micrographs. All scale bars are 50 nm. c) TEM size distributions for AfFtn-AuNP pre- (blue) and post- (red) growth. d) TEM size distributions for BSA-AuNP pre-(blue) and post- (red) growth. AfFtn-AuNP particles are highly monodisperse post-growth, while BSA-AuNP samples are less so, due to the lack of protein templating.

Because TEM is not an ensemble measurement and can be prone to bias, we also characterized the bulk solution samples by UV-visible spectroscopy. Due to the optical properties of the AuNPs, a surface plasmon resonance (SPR) peak is observed in the UV-

vis spectrum. The monodispersity of the sample is reflected in the width of the SPR peak, with more monodisperse samples showing a narrower peak. We compared the UV-vis spectra of the samples pre- and post-growth, as shown in Figure 4.4 and summarized in Table 4.1. Supporting the TEM results, all of the AfFtn samples showed a narrowing of the SPR peak post-growth, with $AuCl_3$ showing the greatest change (-14 nm). In contrast, the BSA control samples ranged from marginal narrowing (-4 nm, $HAuCl_4$) to significant broadening (+30 nm, $AuCl_3$). With lower monodispersity than the AfFtn-templated samples, the BSA samples demonstrate the requirement for ordered protein assembly around the AuNP surface to ensure controlled particle growth, i.e., protein templating.

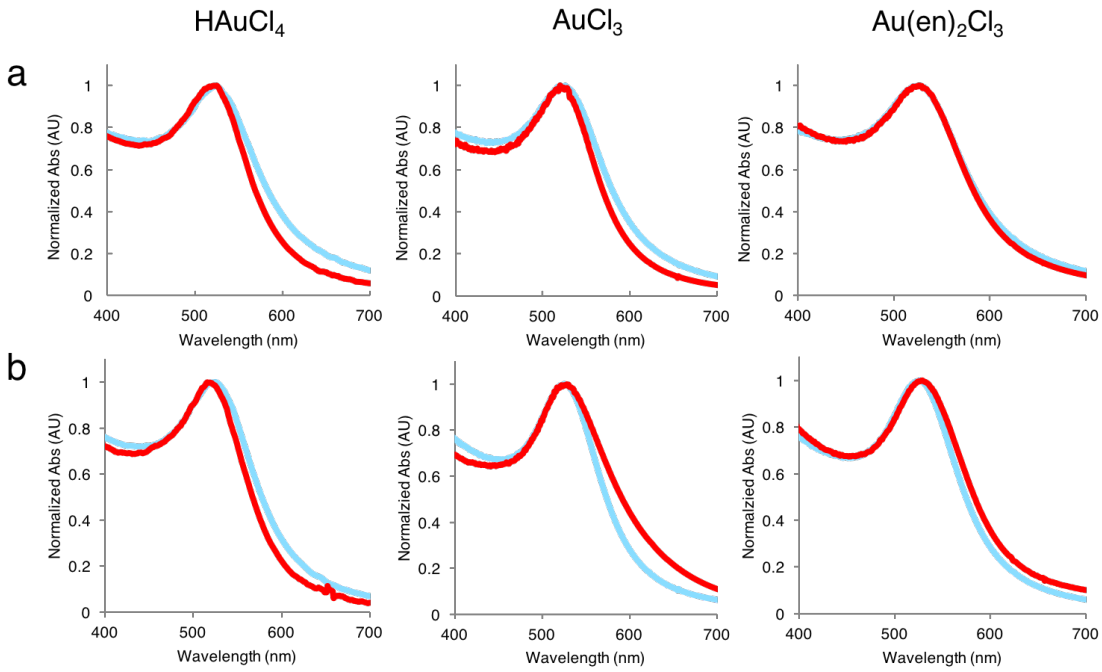

Figure 4.4 UV-vis spectra pre-growth (blue) and post-growth (red). a) AfFtn-AuNP samples. b) BSA-AuNP samples. A narrowing of the surface plasmon resonance peak at ~520 nm indicates more monodisperse sample.

Table 4.1. Summary of UV-vis and TEM results

Sample	D_{avg} (nm)[a]	N[b]	Δ2xHWHM (nm)[c]	ΔD_{avg} (nm)[d]
AfFtn $HAuCl_4$	6.3 ± 1.1	1262	-8	0.3
AfFtn $AuCl_3$	7.8 ± 0.9	508	-14	1.5
AfFtn $Au(en)_2Cl_3$	7.0 ± 0.8	648	-6	1.0
BSA $HAuCl_4$	7.1 ± 0.9	520	-4	0.8
BSA $AuCl_3$	9.4 ± 3.7	530	+30	3.3
BSA $Au(en)_2Cl_3$	8.0 ± 2.8	358	+14	1.9

[a]D_{avg} is average diameter calculated after using Analyze Particles function in ImageJ[111] to measure particle areas.
[b]Number of particles used to calculate average diameter.
[c]The change in twice the half-width at half-max (HWHM) gives a measure of the peak width, which is reflective of sample monodispersity.
[d]Batches varied slightly, with average initial particle diameters of either 6.0, 6.1, or 6.3 nm.

It is striking that the seeded growth experiments with AfFtn and BSA showed the same gold salt preference, with the largest AuNPs formed with $AuCl_3$, followed by $Au(en)_2^{3+}$ and $AuCl_4^-$ (Table 4.1). Similar to AfFtn, BSA is an acidic protein, with estimated pI of 4.7. Thus, both proteins at pH 7.6 should electrostatically repel $AuCl_4^-$, leading to less efficient AuNP growth. Moreover, the electrostatic interaction of the gold salt with the negatively charged, BSPP-coated AuNP should also disfavor $AuCl_4^-$. However, the preference for $AuCl_3$ over $Au(en)_2^{3+}$ likely arises from the much lower reduction potential of $Au(en)_2Cl_3$, which was reported to be -0.290 V and disfavors reduction by ascorbate.[173] The standard reduction potential for Au(III) chloride species is typically much more favorable, as shown by this half-reaction:

$AuCl_4^- + 3e^- \rightarrow Au + 4\ Cl^-$ $E° = 1.0$ V vs. NHE.[178,179] Our results demonstrate the significant effect of the charge and reduction potential of the gold complex on seeded particle growth within AfFtn.

The AfFtn $AuCl_3$ post-growth sample was further analyzed by native gel electrophoresis (Figure 4.5). By native gel, AfFtn and the templated AuNPs remained associated, with overlapping blue protein and red NP bands. Combined with TEM and UV-vis data, this suggests that the AuNP remains within the AfFtn cavity and no formation of *de novo* particles occurs. The size exclusion chromatography (SEC) FPLC trace shows several peaks, which can be assigned to AfFtn 24mer (presumably with AuNP inside) and excess ascorbic acid (Figure 4.6a). Circular dichroism spectroscopy was used on the collected fractions to verify these assignments (Figure 4.6b). However, the sample concentration was low and the S:N was poor, making it difficult to discern whether any α-helix signal was present in the "24mer" peak. The spectrum for the ascorbic acid peak was more distinct and could be confidently assigned based on a published spectrum.[180] None of the fractions collected appeared red in color, but a faint thin red band was noted at the top of the column. Even though the AuNPs appear to be encapsulated within the AfFtn cavity, they do not appear to be passing through the filter at the top of the column successfully. Whether this is due to some non-ideal interaction with the filter material or the general conditions of the SEC experiment (high pressure flow) remains to be determined.

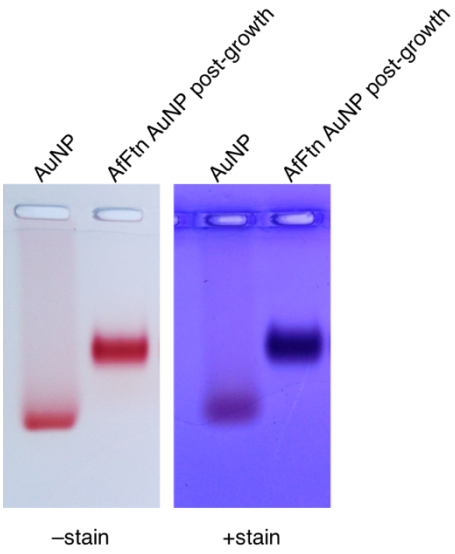

Figure 4.5. Native gel electrophoresis of AfFtn AuNP post-seeded growth using $AuCl_3$ as the gold salt. Overlapping red AuNP and blue protein bands indicate particles remained inside the ferritin cage.

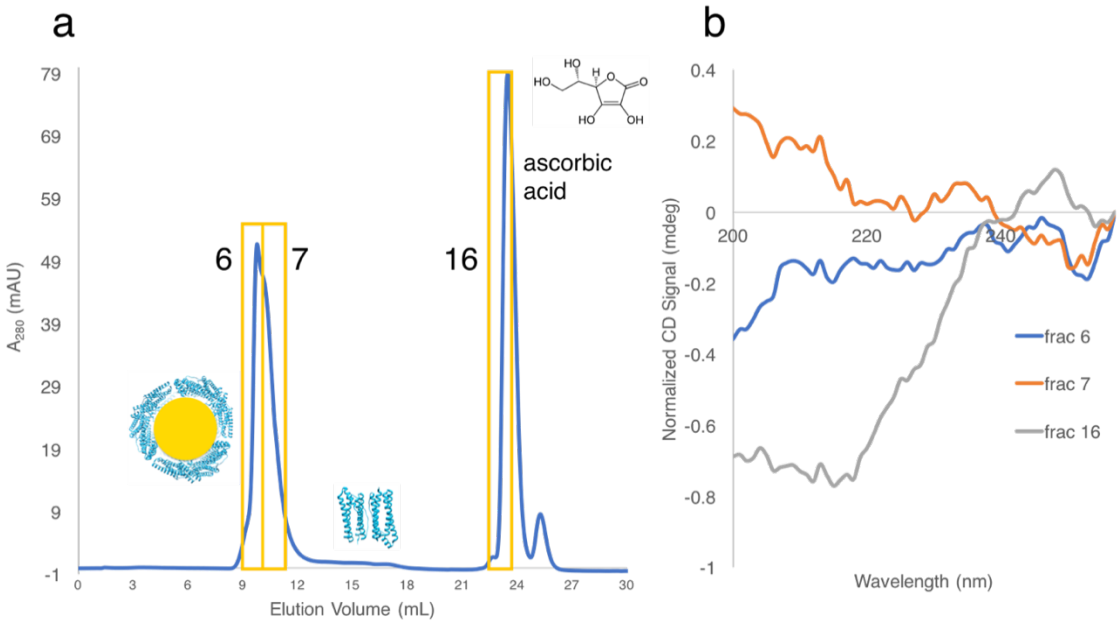

Figure 4.6. a) Size exclusion chromatography of AfFtn AuNP post-seeded growth using $AuCl_3$ as the gold salt. Peak at ~10 mL is expected to correspond to grown AuNP encapsulated within AfFtn, ~16 mL AfFtn dimer (cage disassembly product), ~24 mL excess ascorbic acid. b) Circular dichroism spectroscopy analysis of SEC fractions. S:N is low for all samples, making it difficult to identify any characteristic α-helix signal, though fraction 16 does resemble the published spectrum of ascorbic acid.

To better understand the seeded growth process using $AuCl_3$, we collected a UV-visible spectrum after each step (Figure 4.7). After addition of $AuCl_3$, the solution immediately turned more purple in color but remained clear. The UV-vis spectrum shows a corresponding red shift of 18 nm (from 522 to 540 nm) in the SPR peak. After incubation for 3 h at rt and desalting the sample, the peak remained red-shifted but showed a slight narrowing on the right side, indicating the removal of larger AuNP aggregates. TEM results suggest this red shift is due to deposition of gold ions on the AuNP surface and clustering of multiple AfFtn-AuNP particles. Post-desalting we measured an increase in average AuNP diameter of 0.4 nm (Figure 4.8a), corresponding to a monolayer of gold ions,[181] as seen in the templating scheme in Figure 4.1. By TEM we also observed AfFtn-AuNP clustering (Figure 4.8b). Although the grid was unstained, the outlines of AfFtn donut-like shapes are clearly visible, likely due to electron-dense gold ions decorating their surfaces and interior cavities. After addition of ascorbic acid, the SPR peak immediately blue-shifted to 523 nm (Figure 4.7), and the final particle size was reached. TEM samples prepared immediately after ascorbic acid addition and after 24 h looked very similar (Figure 4.9), indicating rapid AuNP growth. Because the growth happens so rapidly, most of the gold ions necessary for increasing the particle size must be within the cavity or on the AuNP surface by the end of the 3 h incubation with gold salt, which is also consistent with the TEM data (Figure 4.8a).

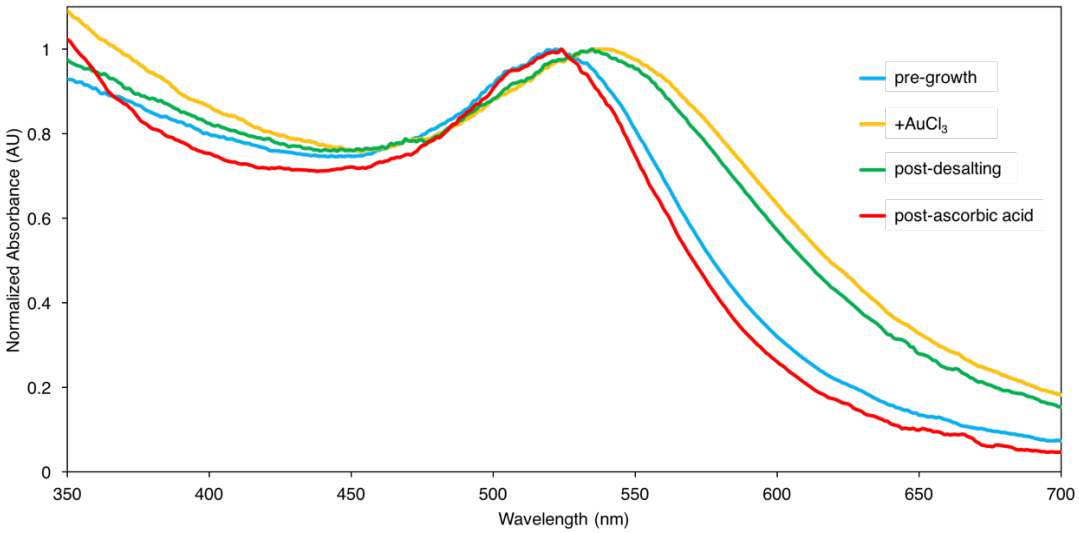

Figure 4.7. UV-visible spectra after each step in the seeded growth process. A large red-shift is seen after the addition of $AuCl_3$, along with SPR broadening. Desalting narrows the SPR somewhat. Addition of ascorbic acid results in a blue-shift almost to the initial wavelength, along with SPR narrowing.

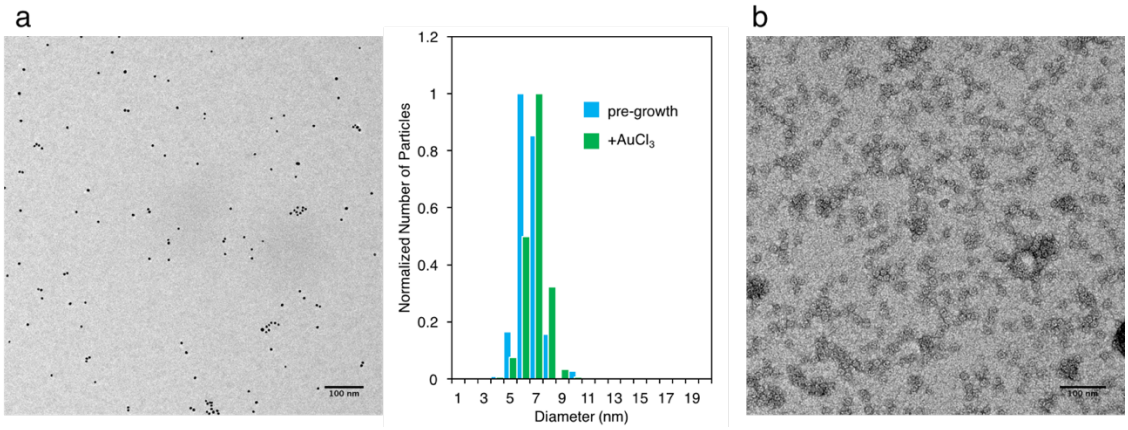

Figure 4.8 TEM analysis after $AuCl_3$ addition. a) TEM micrograph after 3 h incubation with $AuCl_3$ showing particle size increase of 0.4 nm due to gold ion deposition. 241 particles were measured for the pre-growth sample and 338 particles were measured for the $+AuCl_3$ sample. b) Evidence for clustering of AfFtn-AuNPs after addition of $AuCl_3$. Scale bars are 100 nm for both images.

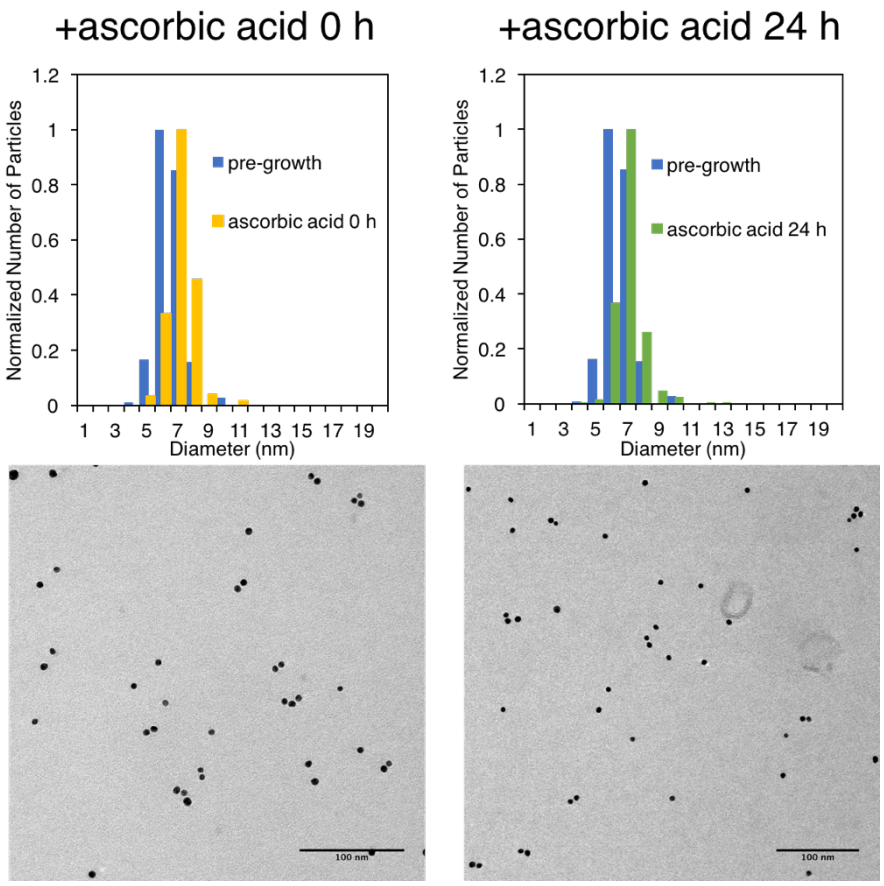

Figure 4.9. TEM micrographs of samples post-addition of ascorbic acid, comparing immediate and 24 h time points. Particle size was measured using ImageJ, [111] with 5-infinity nm^2 as the size range and 0.5-1.0 as the circularity. 338 particles were analyzed for 0 h sample, 330 for 24 h.

Effect of ferritin pore size on templating

Finally, we were interested in comparing the templating capabilities using $AuCl_3$ of AfFtn-wt with a closed pore mutant AfFtn-AA (K150A/R151A).[116] We have recently shown that wt and closed pore AfFtn maintain their quaternary structure upon encapsulation of AuNP, with the open pore preserved for wt (see Chapter 3). The large (4.5 nm) open pore of wt should facilitate easy access to the AuNP surface for gold ions in solution, while gold ions added to the AfFtn-AA sample will need to diffuse through much

smaller (< 1 nm) openings between subunits in the assembled protein, or rely upon dynamic protein structural fluctuations.

We repeated the same seeded growth protein-templating reaction with AfFtn-AA and characterized the post-growth sample by UV-vis spectroscopy and TEM (Figure 4.10). The post-growth average particle size was 7.0 ± 0.9 nm, corresponding to 40% yield, as determined by TEM (151 particles measured). The UV-vis spectrum showed a change in SPR width of -10 nm, indicating narrowed sample size distribution. Our results indicate that AfFtn-AA templates monodisperse particle growth, but to a smaller final diameter compared to wt. This may be due to less $AuCl_3$ present in the cavity when the reducing agent is added. Bulky 5,5′-dithiobis-2-nitrobenzoic acid was recently shown to diffuse more slowly into the internal cavity of AfFtn-AA, compared to AfFtn-wt,[182] suggesting the 3 h incubation period used in our reaction is not long enough for cavity saturation. Several closed-pore ferritins have been shown to template AuNP growth, although the final particle size is generally smaller than the internal cavity diameter.[108,169,183] With a resulting diameter of 7.8 ± 0.9 nm, our seeded growth method using $AuCl_3$ and wt AfFtn shows large AuNPs formed within ferritin (compared to 6.3 ± 0.8 nm in HSAF,[169] 2-4 nm in human H ferritin,[108] and 5.7 ± 1.6 nm in HSAF[183]). Although the final particle size is slightly smaller than our original iterative templating process (8.2 ± 1.9 nm),[51] seeded growth using $AuCl_3$ as presented here is considerably more efficient and twice as fast, requiring only one addition of gold ions and reducing agent, instead of two. In addition, the particles formed using a single round of $AuCl_3$ addition are more monodisperse, as measured by both TEM (0.9 nm average diameter standard deviation versus 1.9 nm) and UV-vis (narrowing of SPR versus slight broadening).

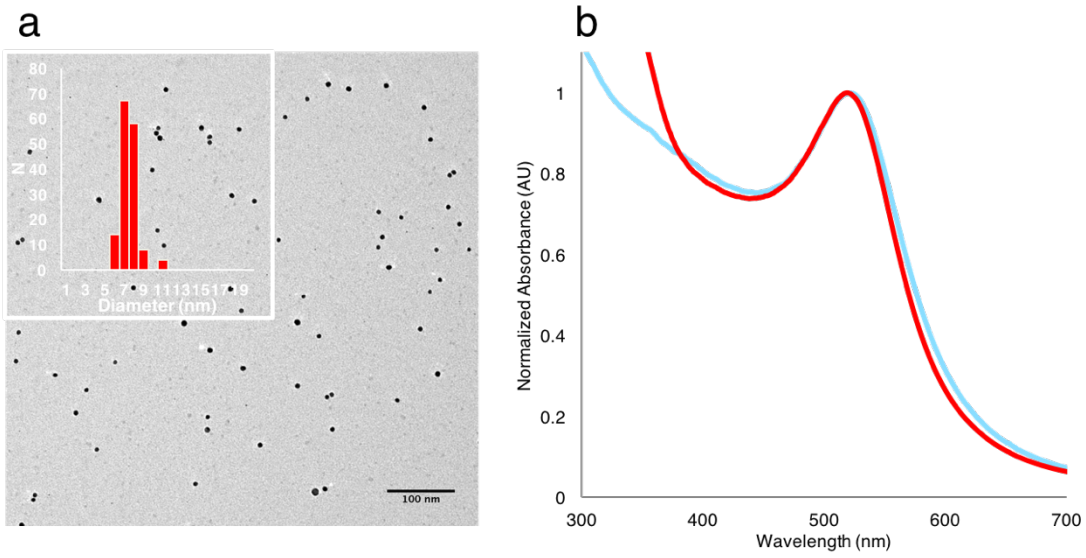

Figure 4.10. Characterization of AfFtn-AA AuNP templated growth. a) TEM micrograph of post-growth sample. Scale bar is 100 nm. b) UV-vis spectrum of pre-growth (blue) and post-growth (red) samples.

Recently published crystal structures of recombinant horse liver ferritin (rHLFr) in the presence of gold ions and reducing agent shed light on how gold ions might interact with the ferritin cavity.[184] rHLFr has octahedral symmetry, with similar assembly to the closed pore AfFtn-AA. Au ions were found to coordinate in three locations in rHLFr: at the 3-fold axis, at an engineered accumulation center diagonal from the 3-fold axis containing two additional cysteines, and at a Met and His pair across from the accumulation site. After addition of $NaBH_4$ reducing agent, the gold ions migrated to the 3-fold axis and formed a sub-nanocluster. While AfFtn lacks cysteine and methionine residues (apart from the start Met, which may be cleaved during production in *E. coli*), several gold-binding amino acids[185] decorate the 3-fold axis (Figure 4.11a). These amino acids may bind gold and direct its entry into the cavity and to the AuNP surface for both open and closed pore AfFtn. The large triangular pore of AfFtn is also rimmed with gold-binding amino acids

(Arg, His, Tyr, Lys, see Figure 4.11b). These features, combined with its open accessibility for easy diffusion, may help to improve Au loading over AfFtn-AA.

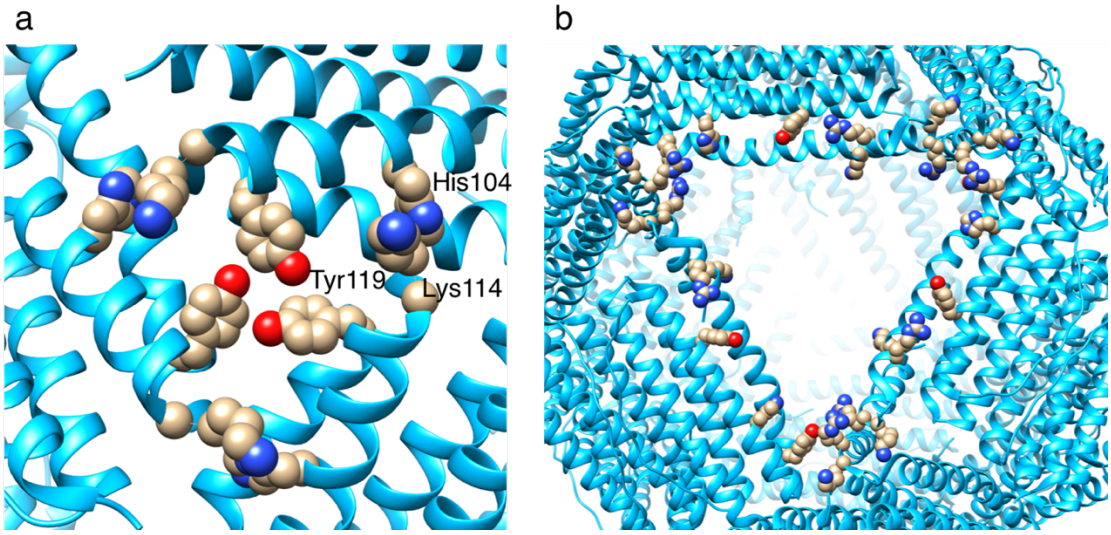

Figure 4.11. Locations of gold-binding amino acids along the pores of AfFtn. a) Small 3-fold pores feature Tyr119, His104, and Lys114, all of which have been shown to have an affinity for Au ions. b) The large triangular pore is also lined with gold-binding amino acids including Arg, His, Tyr, Lys.

4.3 Conclusions

The selection of gold salt is an important consideration for optimizing AfFtn-templated AuNP seeded growth. Neutral $AuCl_3$ yielded larger AuNP that filled the AfFtn cavity more completely compared to charge repulsive $AuCl_4^-$ or charge complementary $Au(en)_2Cl_3$ (70% gold atom incorporation versus 10% and 40%), which also led to greater AuNP monodispersity. The lack of an open pore in the mutant AfFtn-AA inhibits AuNP growth, showing the advantage of a ferritin template with a more porous cage structure. The AuNP synthetic process described here strikes a favorable balance between high gold incorporation efficiency and large particle size compared to all other ferritin-AuNP synthetic routes described to date. The porous protein coverage of AfFtn provides an elegant way to control AuNP chemistry in solution, preventing AuNP aggregation and bulk

precipitation. Such a functional, symmetric structure is difficult to recreate in abiological synthetic systems, e.g., by coating with polymer or small molecule ligands. AfFtn-AuNP conjugates could be used as more selective catalysts or for further NP manipulation, such as templating further NP growth or surface functionalization through the AfFtn open pores.

4.4 Experimental Procedures

Protein expression and purification. Thermophilic ferritin protein was expressed and purified as previously published[52] (see Chapter 2). The pAF0834 plasmid containing thermophilic ferritin was obtained from Eric Johnson (California Institute of Technology) and the plasmid containing K150A/R151A was purchased from DNA 2.0 (now ATUM). Purity was confirmed using SDS-PAGE (4–15% Tris–HCl, Mini-Protean TGX gel), shown in Figure 4.12. Protein concentration was determined using the Bradford Assay, with bovine gamma globulin as a standard.

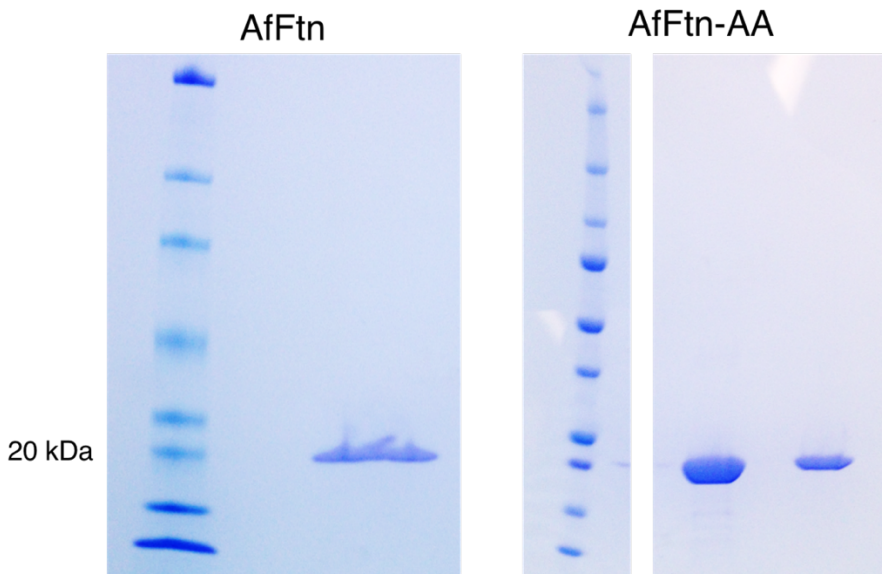

Figure 4.12. SDS-PAGE of AfFtn and AfFtn-AA used, confirming purity with bands at ~20 kDa, corresponding to monomer weight.

Gold nanoparticle ligand exchange. Citrate-coated 5 nm AuNPs were purchased from TedPella. Actual average diameter when measured by TEM was 6.0-6.3 nm, see Figure 4.13. Ligand exchange from citrate to bis-*p*(sulfonatophenyl)phenylphosphine (BSPP) was done following previously published procedure.[51] Briefly, 50 mL of AuNP solution was stirred overnight with 20 mg BSPP at rt. NaCl was added until the NPs precipitated, the sample was centrifuged at 3000 rpm, 4 °C for 30 min. The supernatant was discarded and the AuNP pellet was resuspended in DI H_2O and reprecipitated with methanol. The sample was then centrifuged again at 3000 rpm, 4 °C for 30 min. The washed pellet was resuspended in DI H_2O and the AuNP concentration was measured using an extinction coefficient provided by the manufacturer of 9.696 x 10^6 M^{-1} cm^{-1} at 520 nm.

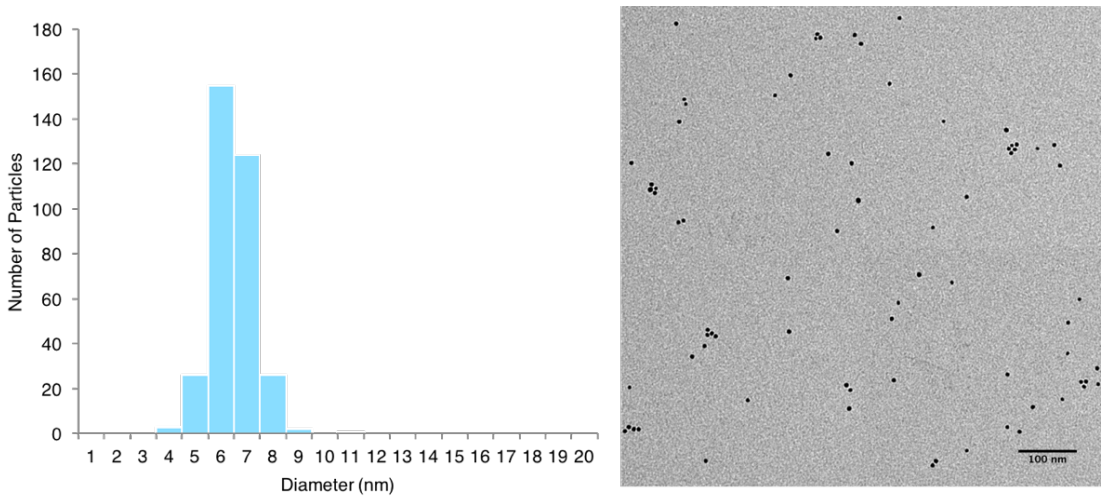

Figure 4.13. Transmission electron microscopy of citrate-coated AuNPs. TEM sample was prepared on a carbon-coated copper grid without stain, and imaged using a Tecnai T-12 microscope operating at 120 keV. Particle size was measured using the Analyze Particles function on ImageJ,[111] with 5-infinity nm^2 as the size range and 0.5-1.0 as the circularity. Scale bar is 100 nm. For batch shown, the average particle diameter was 6.0 ± 0.8 nm, based on measurement of 337 particles.

AfFtn-AuNP encapsulation. Protein-AuNP samples were prepared by first disassembling AfFtn overnight in 20 mM phos (pH 7.6) buffer at 4 °C. Disassembled

protein was mixed with AuNPs to a final concentration of 0.6 μM AfFtn, 0.6 μM AuNP in 20 mM phos (pH 7.6) buffer. The sample was incubated at room temperature with gentle agitation (gel rocker) for 48 h.

Synthesis and characterization of $Au(en)_2Cl_3$. $Au(en)_2Cl_3$ was prepared following the method of Zhu et al.[173] $HAuCl_4$ (0.50 g, 1.5 mmol) was added to 5 mL H_2O, followed by dropwise addition of 0.225 mL (3.4 mmol) ethylenediamine with stirring. The red-orange solution was stirred for 30 min at rt. The product was precipitated with 35 mL ethanol and then vacuum filtered (washing with ethanol). The resulting pale yellow solid was dried overnight under vacuum and isolated in 47% yield (290 mg, 0.92 mmol). The ^1H NMR spectrum in D_2O had one peak corresponding to the amine hydrogens at 3.291 ppm (Figure 4.14a). The product was also characterized by elemental analysis: Found %: C, 11.19; H, 2.94; N, 13.42; Cl, 24.97. Calc %: C, 11.34; H, 3.81; N, 13.23; Cl, 25.11. For further confirmation of the identity of the product, cyclic voltammetry was performed using Ag/AgCl as reference electrode, glassy carbon as working electrode, and Pt as counter electrode (Figure 4.14b). The electrolyte solution was 0.4 M KCl and the scan speed was 0.1 V/s.

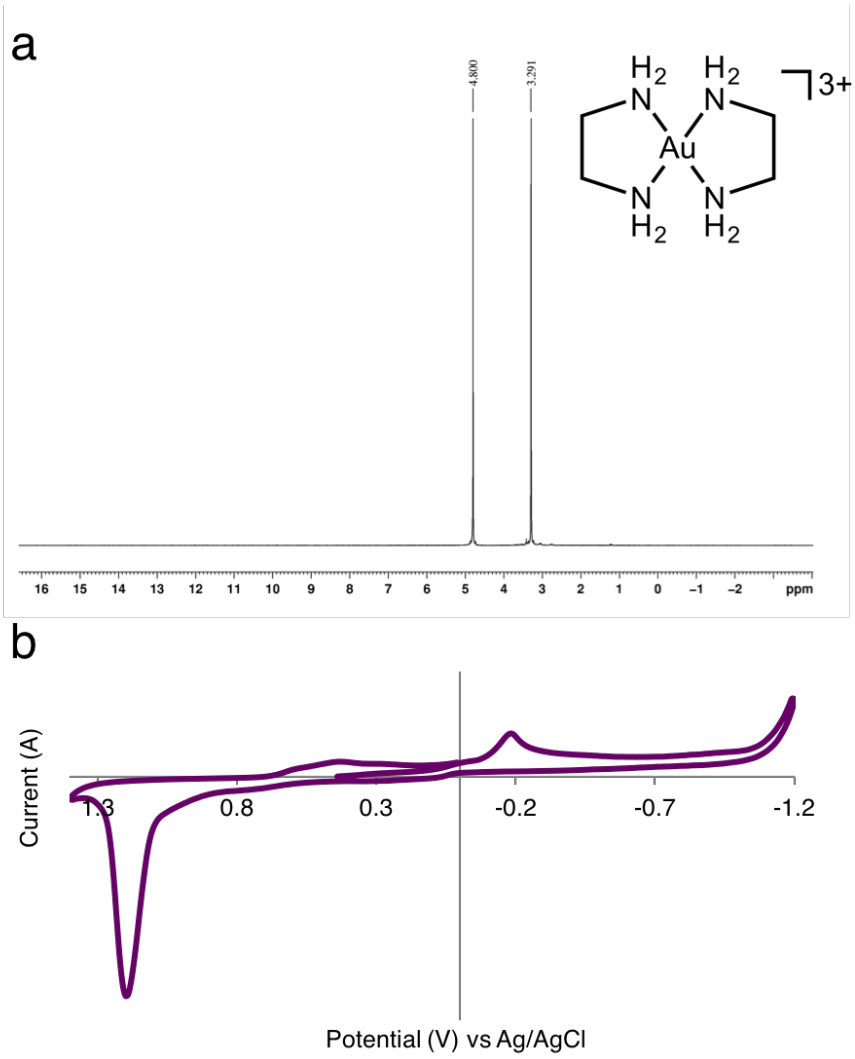

Figure 4.14. Characterization of $Au(en)_2Cl_3$. a) NMR spectrum of $Au(en)_2Cl_3$, taken in D_2O. Peak at 3.291 ppm corresponds to published NMR spectrum.[186] b) Cyclic voltammetry of $Au(en)_2Cl_3$, matching data previously by Zhu et al.[186].

Gold atom stoichiometry calculation. The theoretical number of gold atoms needed to grow particle size from 6 nm to 8 nm was based on the unit cell volume of gold. Gold crystallizes in fcc packing, resulting in 4 atoms per unit cell. The volume of a unit cell of gold is 0.0679 nm^3. Using $V = \frac{4}{3}\pi r^3$, the volume of a 6 nm AuNP is 113.097 nm^3 and the volume of an 8 nm AuNP is 268.083 nm^3; therefore, an additional volume of

154.985 nm^3 is needed. If there are 4 gold atoms for every 0.0679 nm^3, 9130 gold atoms will be needed to increase the particle size to 8 nm.

Seeded growth templating. AfFtn-AuNP sample (500 μL of 0.6 μM solution) was used for the templated growth. 10,000 eq of gold salt were added (from 0.1 M stock solution) and the sample was incubated at rt for 3 h. Excess gold ions were then removed using a 10DG gel filtration column (Bio-Rad), equilibrated with 20 mM phos pH 7.6 buffer. Four 1 mL fractions were collected and those containing protein and AuNP (as confirmed by UV-vis spectroscopy) were combined. Ascorbic acid (30,000 eq from 0.1 M freshly prepared stock) was added, and the sample incubated overnight at rt.

Seeded growth AuNP characterization. UV-vis spectra were collected on an Agilent 8453 UV-visible spectrometer. Samples for transmission electron microscopy (TEM) were prepared on carbon-coated copper grids (Electron Microscopy Sciences), unstained. Grids were imaged on a Tecnai T-12 microscope operating at 120 keV. Particle diameters were calculated after measuring particle area using the Analyze Particles function on ImageJ [111], with 5-infinity nm^2 as the size range and 0.5-1.0 as the circularity. At least 150 particles were analyzed per sample. Native agarose gels (0.7%) were run at 100 V, 20 min, rt. Circular dichroism spectroscopy was done using an Aviv 410 CD spectrometer with 1 mm quartz cuvettes, scanning 190-260 nm at 25 °C. Size exclusion chromatography was done on a Superdex200 Increase 10/300 GL column on an AKTA FPLC system, using 20 mM phos (pH 7.6) as the buffer. 200 μL of AfFtn-AuNP sample was injected onto the column and eluted at 0.9 mL/min.

4.5 Acknowledgments

This work was supported by NSF grant (PD 09-6885, CHE-1508318) to I.J.D. We thank the University of Pennsylvania Electron Microscopy Resource Laboratory for use of the TEM.

CHAPTER 5: THERMOPHILIC FERRITIN ENCAPSULATION OF SUPERCHARGED GFP

5.1 Introduction

Supramolecular host-guest complexes have wide-ranging applications including sensing,[187,188] catalysis,[189] separations,[190] and drug delivery.[191] Synthetic host-guest systems include cyclodextrin-adamantyl-functionalized molecules, which have been used in delivery of nucleic acids[191,192] and chemotherapeutics,[193] and cyclodextrin-azobenzene host-guest pairs, which have been used for glucose sensing.[188] Cucurbituril-guest interactions have been used in catalyzing 1,3-dipolar cycloadditions, and oxidation, hydrolysis, and photochemical reactions.[194] The affinity of calixarenes for many amino acids has been leveraged to make protein microarrays for biosensing.[195] In nature, host-guest complexes are often seen in the form of protein-protein interactions. Chaperone proteins are one example, where a host protein accepts a guest protein, helping it to fold or refold properly.[196] Likewise, in bacterial microcompartments polyhedral protein shells encapsulate an enzyme, preventing the release of toxic metabolic intermediates.[197] Several non-native protein-protein host-guest complexes have been reported using lumazine synthase from *Aquifex aeolicus*, encapsulin, or viral capsids such as MS2, cowpea chlorotic mottle virus (CCMV), and P22. These large (>25 nm diameter) protein cages have been shown to effectively encapsulate fluorescent protein variants,[10,11,198,199] HIV protease,[8] Cas9,[200] *E. coli* alkaline phosphatase,[198] and a variety of other enzymes with wide ranging structures and functions.[9] Encapsulation of a guest protein within a host protein has enabled kinetic studies of enzymes in confined spaces,[201,202] as well as the development of confined enzyme cascades.[203] Protein host-guest complexes have also been engineered to more easily crystallize a guest protein.[204]

Shown in Figure 5.1, we report a protein-based host-guest complex featuring thermophilic ferritin from *Archaeoglobus fulgidus* (AfFtn) and a supercharged variant of green fluorescent protein with a theoretical net charge of +36 (GFP(+36)).[205] AfFtn exists as dimers of four-helix bundles at low ionic strength (< 200 mM NaCl). Self-assembly of 12 dimers occurs in high ionic strength buffer to form a hollow, cage-like 24mer with tetrahedral symmetry and four large (4.5 nm), triangular pores.[49] Cargo smaller than the 24mer inner diameter (8 nm) can be encapsulated within the protein interior. We have demonstrated the encapsulation of 6-nm gold nanoparticles, where the particles nucleate assembly via their high surface charge.[50–52] We hypothesized that highly charged macromolecules of appropriate size could be encapsulated in a similar process. Here, we show that AfFtn and mutants with altered assembly properties can encapsulate GFP(+36) in a rapid, stoichiometric manner, maintaining the native characteristics of both proteins. An AfFtn mutant lacking the salt-dependent assembly and large triangular pores was able to encapsulate GFP(+36), indicating that cage dynamics play a role in assembly. Notably, wildtype GFP was not encapsulated by AfFtn, highlighting the important electrostatic nature of the interaction. Unlike prior protein-protein host-guest examples where extensive directed evolution,[8] addition of osmolyte,[198] change in pH,[201] or covalent attachment[199] was needed, our system requires no added reagents other than the proteins themselves and works well for wt AfFtn. We demonstrate the ability to tune AfFtn-GFP(+36) encapsulation efficiency using AfFtn mutants with different assembly characteristics.

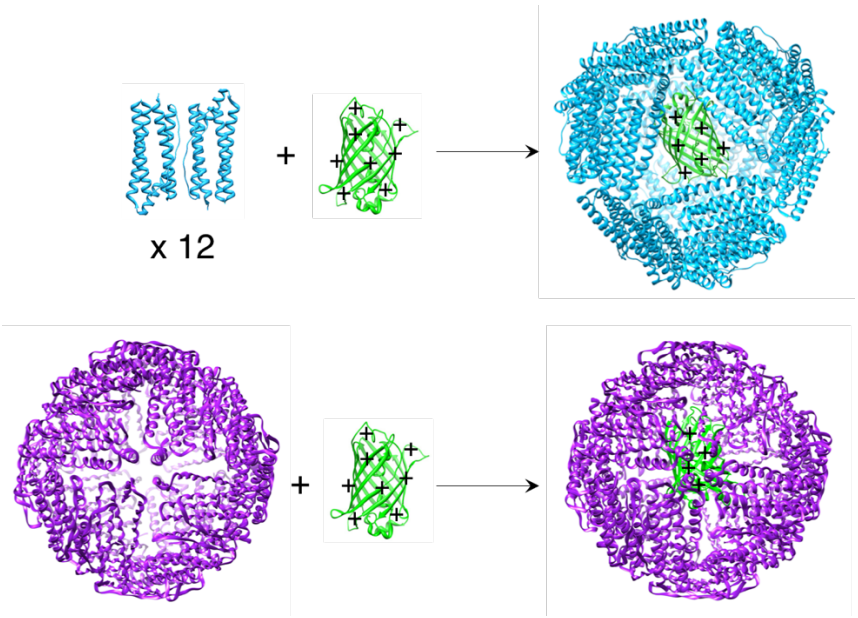

Figure 5.1. Encapsulation of GFP(+36) by wt-AfFtn (top) and E65R-AfFtn (bottom). For wt, 12 AfFtn dimers self-assemble around positively charged GFP(+36) to form a 1:1 AfFtn 24mer:GFP(+36) host-guest complex. E65R encapsulates a single GFP(+36) starting with a complete cage.

5.2 Results and Discussion

AfFtn and GFP(+36) were mixed in varying stoichiometries (AfFtn 24mer:GFP(+36)) ranging from 1:3 to 3:1 in low ionic strength buffer (20 mM phos, pH 7.6) and analyzed by native gel electrophoresis (Figure 5.2a). A single fluorescent green band can be seen running toward the positive gel terminal, corresponding to the AfFtn-GFP(+36) complex. With GFP(+36) in excess, a green band running toward the negative terminal appears as free GFP(+36). Size exclusion chromatography (SEC) was used to verify encapsulation (Figure 5.2b). A_{280} was monitored during chromatography, while GFP(+36) fluorescence was measured for each fraction afterward using a microplate reader. The main A_{280} peak corresponded to AfFtn 24mer elution volume and overlapped with the I_{509} GFP(+36) fluorescence peak, indicating encapsulation. The encapsulation product fractions were combined, concentrated, and analyzed by dynamic light scattering

(DLS) to verify AfFtn assembly (Figure 5.2c). The measured average particle diameter matched that of AfFtn 24mer at 13.9 nm, suggesting that GFP(+36) is inside AfFtn, rather than adsorbed to its surface, or forming a non-specific, unordered aggregate with multiple AfFtn dimers. GFP(+36) absorbance and emission spectra collected pre- and post-encapsulation were highly similar, indicating the protein remained folded (Figure 5.3).

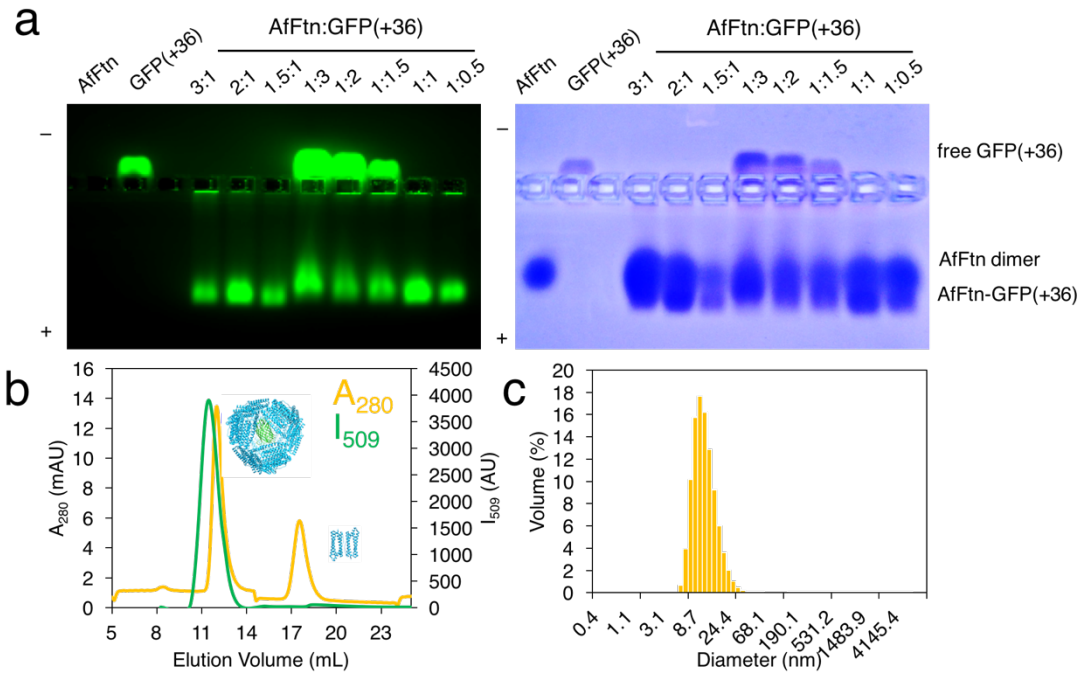

Figure 5.2. Encapsulation of GFP(+36) by AfFtn. a) Native gel electrophoresis varying stoichiometry AfFtn 24mer:GFP(+36). GFP(+36) forms a complex with AfFtn at a ratio of 1:1, with excess GFP(+36) running toward the negative gel terminal due to its higher positive charge. b) Size exclusion chromatography of AfFtn-GFP(+36) complex, monitored by absorbance at 280 nm (yellow) and fluorescence at 509 nm (green). Peak at 12.5 mL corresponds to AfFtn-GFP(+36), peak at 17.5 mL corresponds to AfFtn dimer. c) Dynamic light scattering volume size distribution of SEC peak at 12.5 mL. Average diameter is 13.9 nm with a PDI of 0.256.

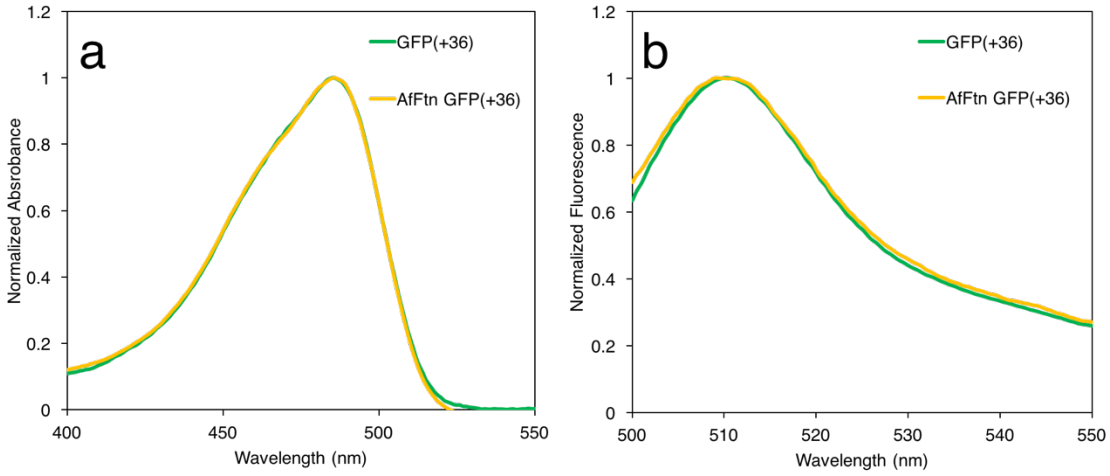

Figure 5.3. Optical properties of GFP(+36) pre- and post-encapsulation. a) Absorbance spectrum with and without AfFtn. b) Fluorescence spectrum with and without AfFtn.

As another confirmation of encapsulation, we incubated AfFtn-GFP(+36) with nickel nitrilotriacetic acid (Ni-NTA) agarose resin. GFP(+36) has a histidine-tag for purification purposes and will therefore bind strongly to the nickel-laced resin. Dissociation from the resin is triggered by addition of imidazole, which competes off the bound protein. If GFP(+36) is encapsulated within a ferritin cage, however, the His-tag should be less able to bind to the Ni-NTA resin. After incubating AfFtn with GFP(+36) overnight and purifying by SEC, we mixed the sample with a Ni-NTA slurry. As a control, we also incubated GFP(+36) alone with the resin. After an hour of binding time, we centrifuged the samples to separate the resin and removed the supernatant. We washed the resin with buffer three times, each time centrifuging the sample and removing the supernatant. We then added buffer with 250 mM imidazole to remove any bound protein and repeated the centrifuging/supernatant removal three times. We measured fluorescence at 509 nm for all supernatant samples (Figure 5.4). Significant GFP(+36) fluorescence is seen for the load AfFtn-containing sample, indicating that little GFP(+36) bound to the

resin. In contrast, low fluorescence was seen for the GFP(+36) load sample (no AfFtn) and significant fluorescence was seen for the first elution sample, indicating that the majority of the protein bound to the resin and was eluted using imidazole. Thus, the majority of GFP(+36) appears to be encapsulated within AfFtn.

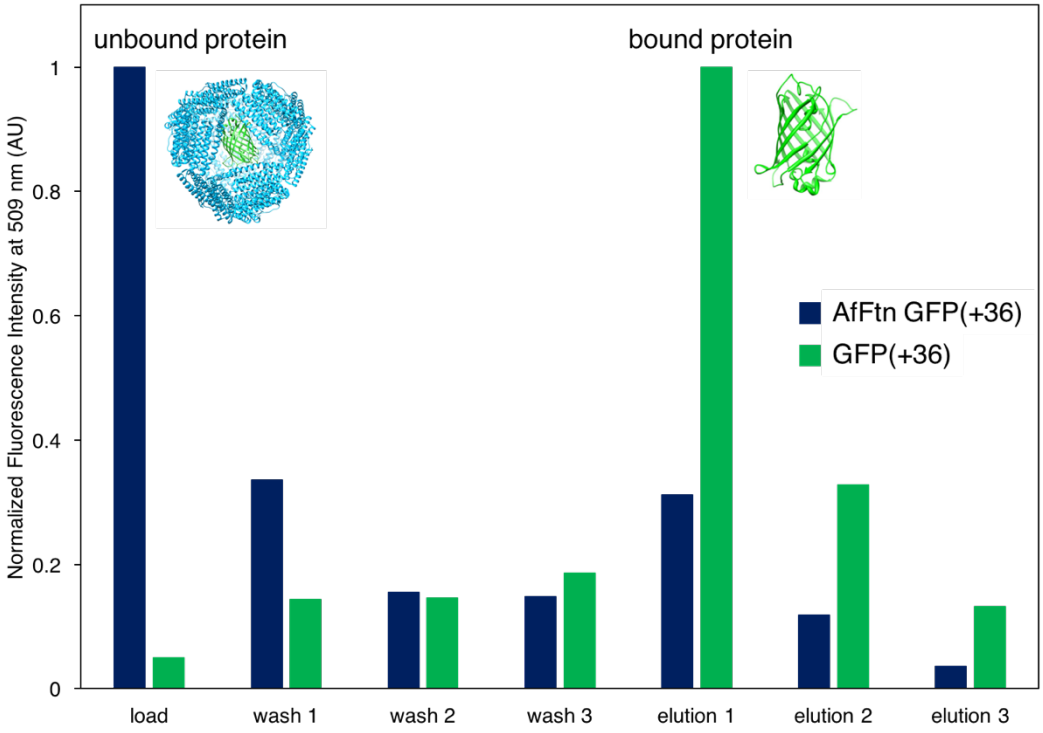

Figure 5.4. Ni-NTA assay shows lack of GFP(+36) binding to resin after encapsulation within AfFtn.

Having confirmed GFP(+36) encapsulation by AfFtn, we were interested in the kinetics of the encapsulation process. Shown in Figure 5.5, we used native gel electrophoresis and SEC to analyze 1:1 AfFtn 24mer:GFP(+36) samples incubated for varying time points. Based on both methods, encapsulation occurs almost immediately, with a fluorescent band corresponding to AfFtn-GFP(+36) at 0 h, and ~60% assembled AfFtn with GFP(+36) fluorescence at ~30 min (measurement time).

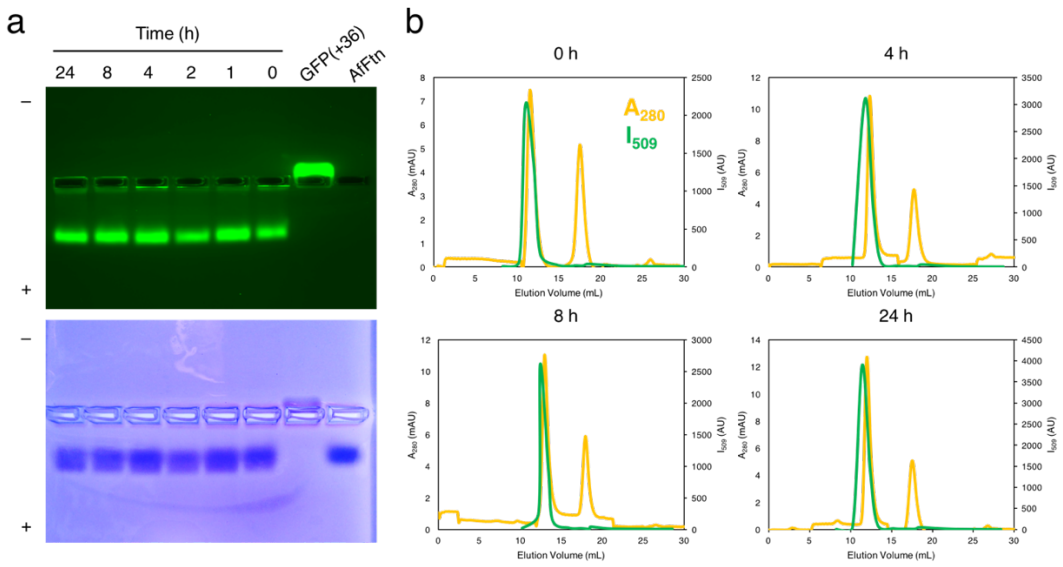

Figure 5.5. Kinetics of GFP(+36) encapsulation. a) Native gel time course for GFP(+36) encapsulation by AfFtn. Fluorescent band that appears within the analysis time corresponds to encapsulation product. b) Size exclusion chromatograms show fast overlap of GFP(+36) fluorescence (green) and A_{280} peak corresponding to AfFtn 24mer (yellow).

We previously reported three AfFtn mutants with varying self-assembly properties: A127R, D138K, and E65R (see Chapter 2). We were interested in exploring whether they could successfully encapsulate GFP(+36) in a similar fashion as wt. Shown in Figure 5.6, we see evidence of encapsulation for all AfFtn mutants by native gel. However, for A127R and D138K there are two clear AfFtn bands seen in the Coomassie-stained gels, one of which overlaps with GFP(+36) fluorescence. This is presumably the encapsulation product, while the second band appears to be unassembled AfFtn dimer, as it increases in intensity when AfFtn is in excess. At 1:1 AfFtn 24mer:GFP(+36), D138K has more encapsulation product compared to A127R, which is consistent with its more favorable assembly. It is striking that E65R is able to efficiently encapsulate GFP(+36), given its propensity to remain assembled, and to assemble in a closed-pore conformation. This also differs from previous experiments with gold nanoparticles (AuNPs), which demonstrated a lack of

encapsulation (see Chapter 2). Encapsulation of large protein cargo without disassembling into small subunits is not without precedent, however. Lumazine synthase from *Aquifex aeolicus* was found to encapsulate supercharged ferritin starting from assembled capsids or capsid subunits, albeit with lower yields for assembled capsids.[118] The cage dynamics are such that protein cargo significantly larger than the 4-nm pores[206] can still enter the cavity. Similar dynamics may be at play for E65R, enabling the GFP(+36) encapsulation observed. GFP(+36) is also smaller than a 6-nm AuNP and potentially more flexible, compared to the hard, inorganic AuNP surface. These factors may help facilitate entry into the E65R cavity for GFP(+36), compared to an AuNP.

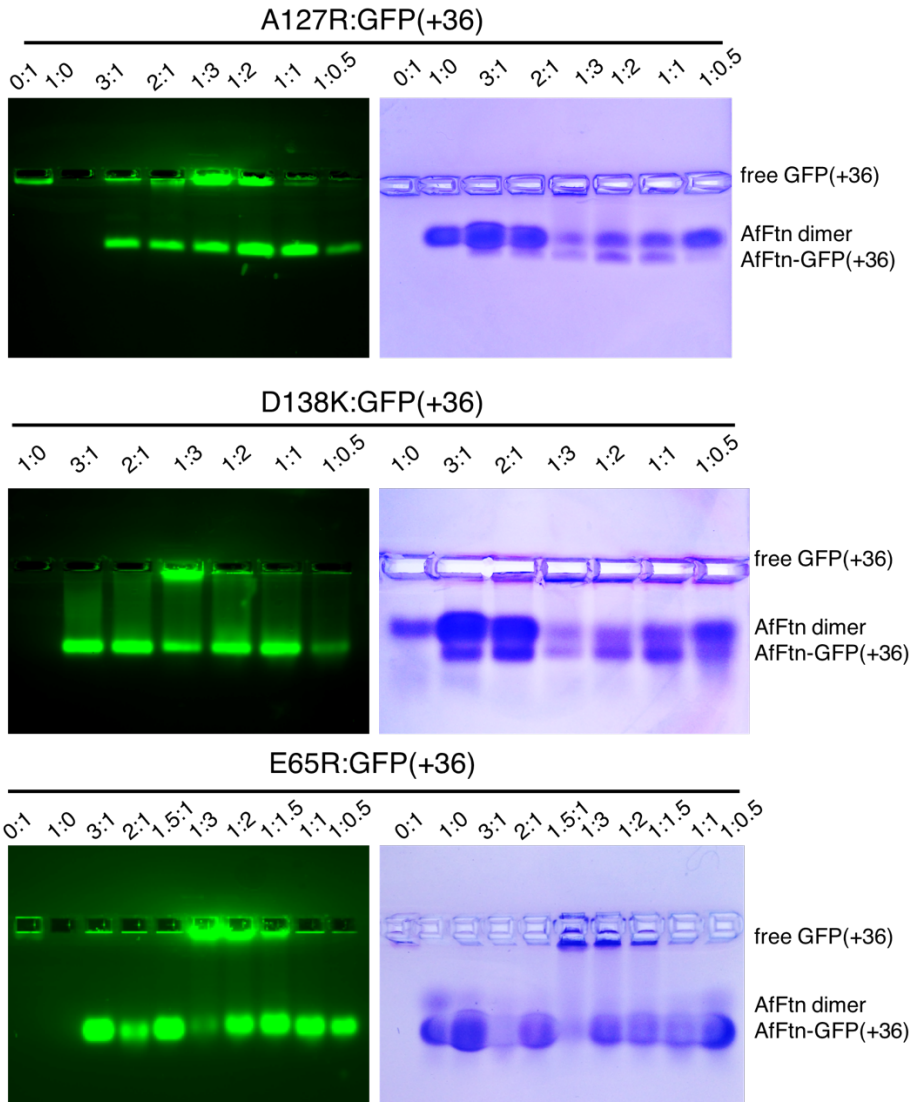

Figure 5.6. Native gel electrophoresis for mutant AfFtn-GFP(+36) samples with varying stoichiometries.

Mutant AfFtn-GFP(+36) samples were also analyzed by SEC and transmission electron microscopy (TEM). GFP(+36) fluorescence was observed mostly in SEC peaks corresponding to AfFtn 24mer, indicating successful encapsulation for all mutants (Figure 5.7), with varying assembly yields. A127R, which had previously been shown to disfavor assembly compared to wt (Chapter 2), had less AfFtn 24mer present compared to D138K and E65R (Table 5.1). These yields do not necessarily represent encapsulation yields, as

E65R and D138K will have some proportion of protein that runs as a 24mer, whether a cargo protein is present. The patterns previously observed in ferritin self-assembly are also seen for self-assembly in the presence of GFP(+36). SEC fractions containing the highest GFP(+36) fluorescence were further analyzed by TEM. As seen in Figure 5.8, ferritin donut-like shapes are observed for all samples including wt, further suggesting the AfFtn variants assembled with GFP(+36) inside.

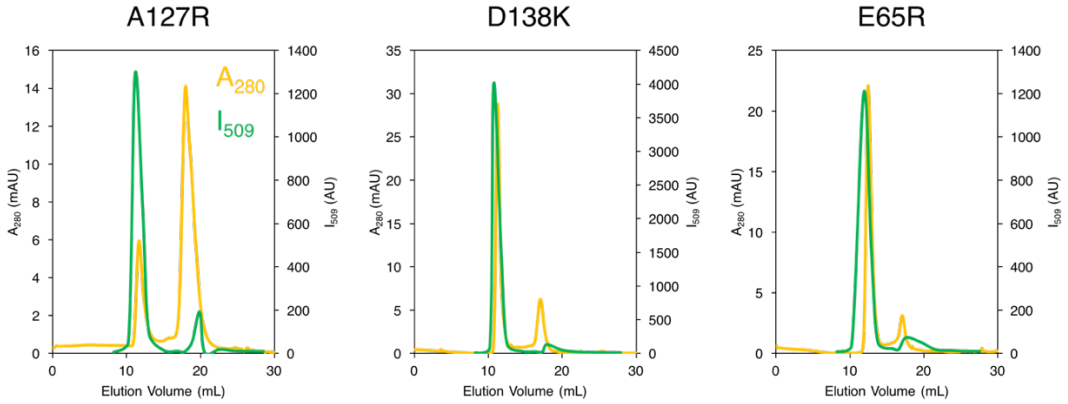

Figure 5.7. Size exclusion chromatography of mutant AfFtn-GFP(+36). Absorbance at 280 nm was measured during the experiment (yellow), and fluorescence intensity at 509 nm was measured post-SEC using a microplate reader (green).

Table 5.1. Size exclusion chromatography of AfFtn GFP(+36)

Sample	% 24mer
wt GFP(+36)	65.2
A127R GFP(+36)	19.9
D138K GFP(+36)	76.1
E65R GFP(+36)	87.9

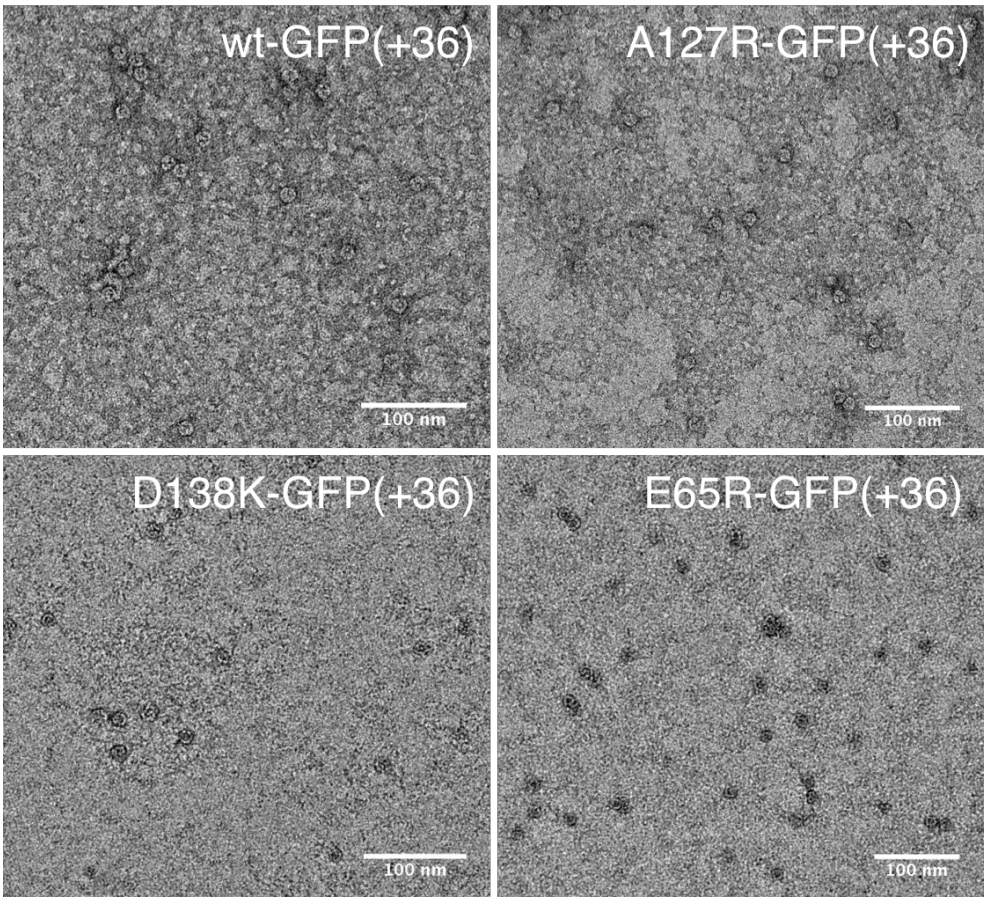

Figure 5.8. Transmission electron microscopy of 24mer fractions from SEC. Scale bars are 100 nm for all images.

By measuring UV-vis spectra, we were able to calculate the number of GFP(+36) per AfFtn 24mer. For AfFtn wt, there are an average of 1.8 GFP(+36) per 24mer. A127R had an average of 1.5, while D138K and E65R had 0.5. GFP loading levels of 0.5-1.8 fall in the expected range, considering the cavity volume of AfFtn is approximately 270 nm^3 based on an internal diameter of 8 nm, while the volume of a single cylindrical GFP(+36) molecule (3-nm diameter x 4-nm height)[118] is approximately 33 nm^3, giving a theoretical maximum of 8 GFP(+36) per 24mer. The high charge of GFP(+36) likely disfavors close packing within the AfFtn cage, leading to the observed ~12% loading. This loading

corresponds to a confinement molarity of ~12 mM (based on a cavity volume of 2.7 x 10^{-22} L), the highest reported for a protein-protein host-guest complex to date.[202] Our percent loading is also similar to that reported for teal fluorescent protein within CCMV capsids.[199] In loading lumazine synthase with GFP(+36), a small population of enlarged capsids was observed, suggesting it was more favorable to shift the assembly symmetry of the capsid to accommodate greater numbers of GFP(+36), rather than packing GFP(+36) more tightly in a smaller volume.[118] The AfFtn mutants that maintain greater assembly at low ionic strengths (D138K and E65R) had lower GFP(+36) loading than wt or A127R. This indicates that encapsulation of GFP(+36) is more favorable starting from AfFtn dimers than fully assembled cages. Attempting to increase the loading by adding higher amounts of GFP(+36) (1:2 or 1:3 AfFtn:GFP(+36)) was unsuccessful and led to significant protein precipitation (Figure 5.9).

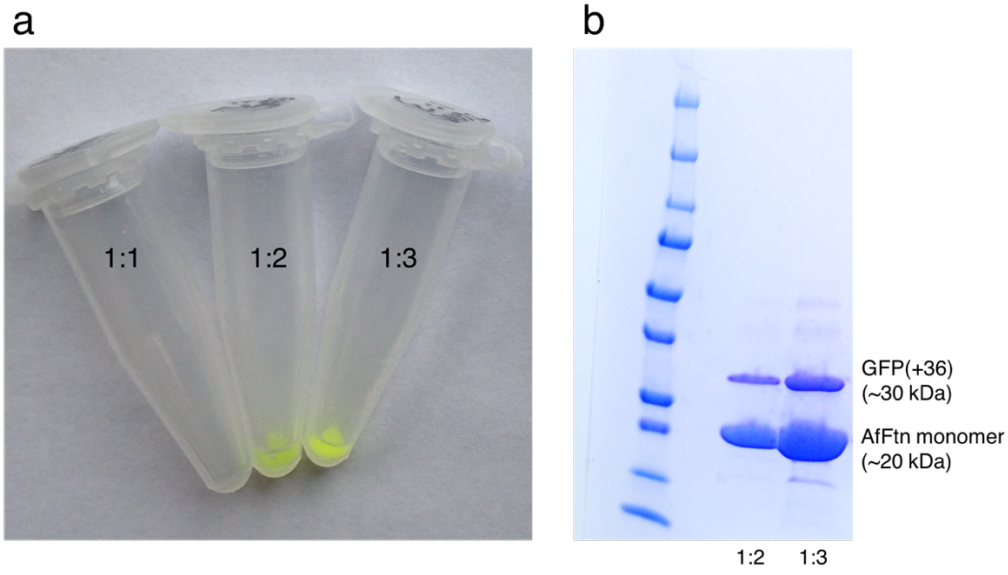

Figure 5.9. Excess GFP(+36) per AfFtn 24mer leads to precipitation of both AfFtn and GFP(+36). a) Green precipitate seen for 1:2 and 1:3 samples, but not 1:1. b) SDS-PAGE shows precipitate contains both AfFtn and GFP(+36).

We also repeated the Ni-NTA binding assay for the mutant AfFtn-GFP(+36) samples (Figure 5.10). Supporting encapsulation, the majority of GFP(+36) was seen to be unbound for all AfFtn-containing samples, with a small amount binding the resin for wt, A127R, and D138K. AfFtn features four large (4.5 nm) triangular pores, and it is possible that although GFP(+36) was inside AfFtn, the His-tag remained somewhat accessible to the resin. It is interesting that E65R has little fluorescence in the elution samples compared to the other AfFtn variants. We recently determined that E65R self-assembles in octahedral symmetry and lacks the large triangular pores (Chapter 2), which would suggest that once encapsulated, the GFP(+36) His-tag is less accessible to the Ni-NTA resin.

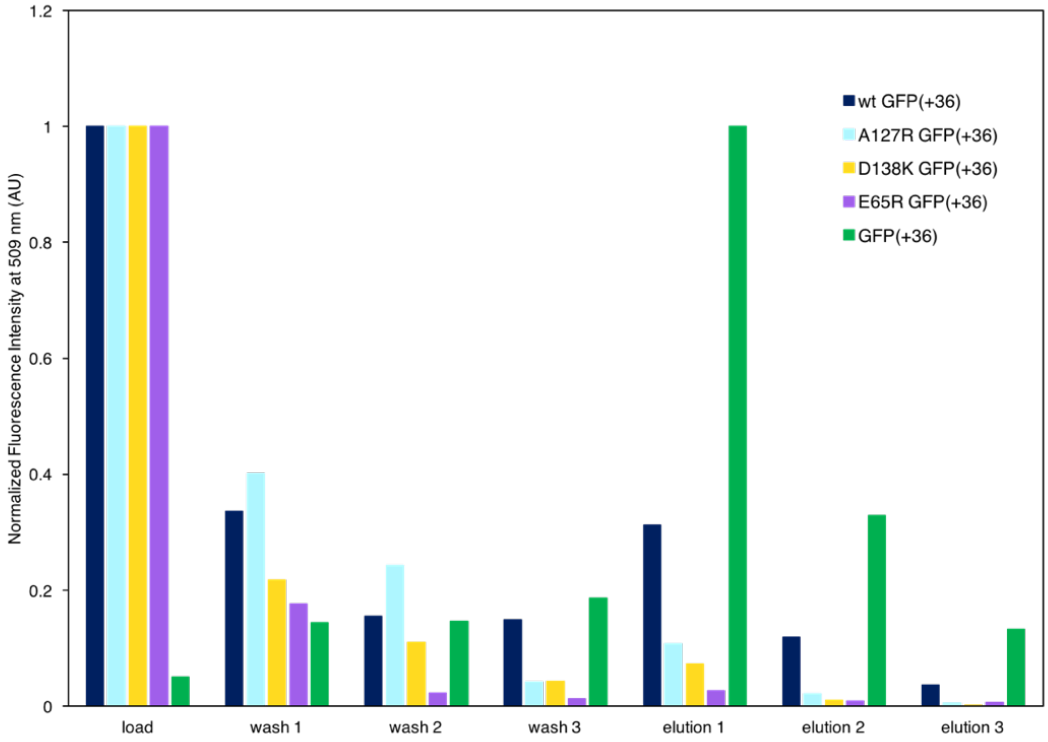

Figure 5.10. Ni-NTA assay shows lack of Histag binding for all AfFtn-containing samples compared to GFP(+36) alone.

To confirm that encapsulation is triggered by the high charge of GFP(+36), we repeated native gel and size exclusion experiments with enhanced GFP (eGFP), a non-supercharged variant with enhanced fluorescence.[207] eGFP has an estimated net charge of -6.4, based on individual amino acid pK_a values. As seen in Figure 5.11, we observed no overlapping eGFP-AfFtn bands by native gel, nor did we see AfFtn 24mer overlapping with GFP fluorescence by SEC. Thus, the encapsulation observed with GFP(+36) is dependent on its high charge.

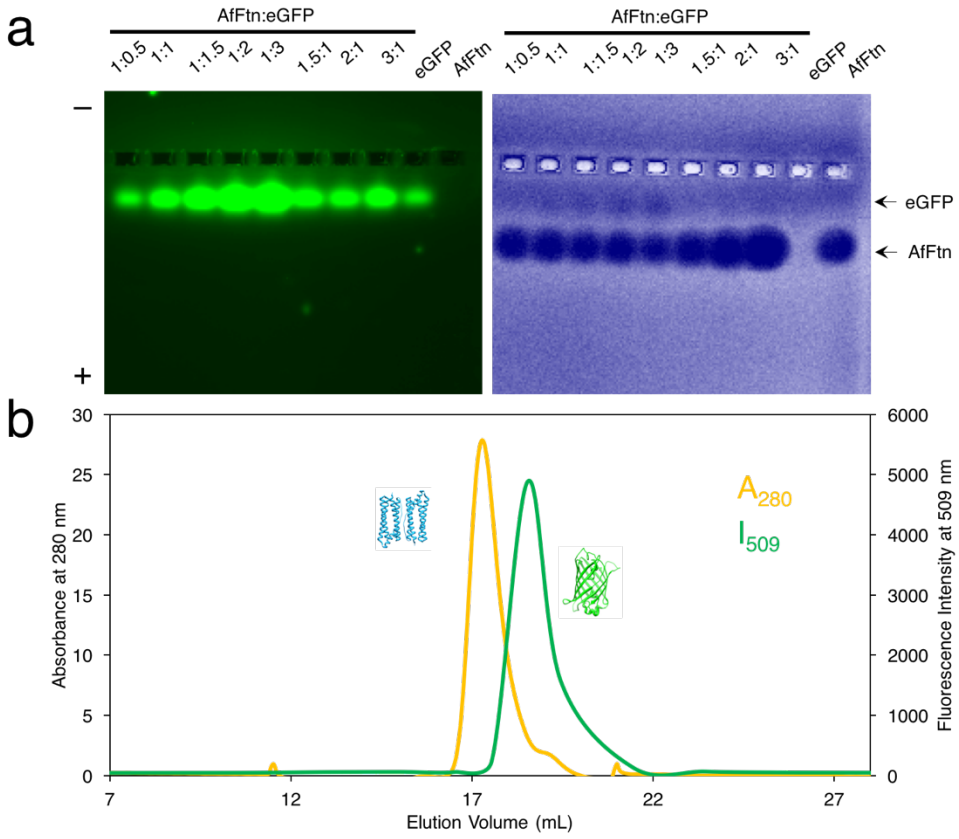

Figure 5.11. Lack of encapsulation for non-supercharged eGFP. a) Native gel showing lack of encapsulation. Fluorescent eGFP bands do not overlap with running position of AfFtn, therefore no encapsulation is observed. b) Size exclusion chromatography analysis of AfFtn-eGFP. No encapsulation is observed by SEC, as only AfFtn dimer is observed (~17 mL) and eGFP fluorescence does not overlap with AfFtn absorbance.

In addition, we investigated the effect of [NaCl] on encapsulation using E65R, to disentangle any effect of pre-assembled cages versus ionic strength. We mixed E65R and GFP(+36) in solutions of increasing [NaCl] and ran them on a native gel, shown in Figure 5.12. At increasing ionic strengths, the fluorescent band corresponding to encapsulated product grows dimmer, suggesting the encapsulation is dependent on electrostatic interactions.

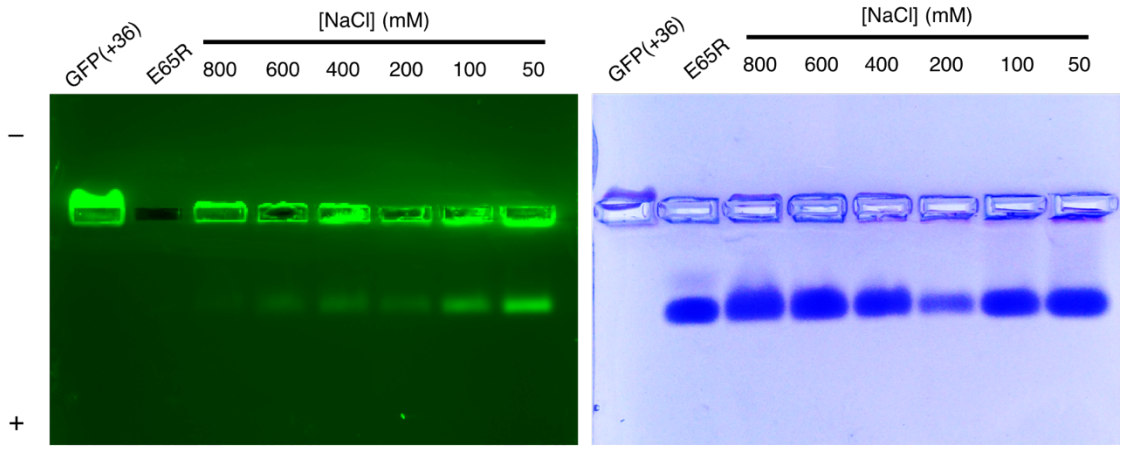

Figure 5.12. E65R-GFP(+36) native gel with increasing [NaCl]. At increasing ionic strengths less encapsulation is observed, as indicated by dimmer fluorescent band traveling towards the positive terminal.

However, once encapsulated, raising the ionic strength of the solution does not appear to completely dissociate the protein complex. After incubating wt AfFtn with GFP(+36) 1:1 overnight in no salt buffer (20 mM phos, pH 7.6), the salt concentration was increased to 400 mM. The sample was run on a size exclusion column equilibrated in high salt buffer (20 mM phos, 800 mM NaCl, pH 7.6), as seen in Figure 5.13. While a free GFP(+36) peak was observed, most GFP(+36) fluorescence overlapped with the AfFtn 24mer peak, indicating the majority remained encapsulated. High salt concentrations should stabilize AfFtn cages, and yet also disfavor electrostatic interaction between AfFtn

and GFP(+36). At the salt concentration used, cage stabilization must be great enough to prevent significant leakage of GFP(+36).

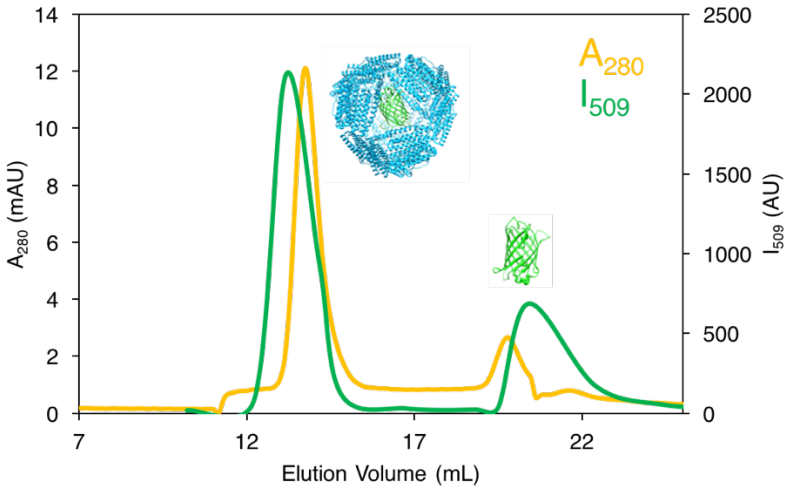

Figure 5.13. SEC of AfFtn-GFP(+36) at high ionic strength. Free GFP(+36) is observed, indicating that increasing ionic strength does partially disrupt the assembly. However, the majority remained encapsulated, suggesting that once encapsulated, the complex is fairly stable.

5.3 Conclusions

We have demonstrated successful formation of a non-native protein:protein host:guest complex using archaeal ferritin and supercharged GFP. The charge of GFP is important for encapsulation, as non-supercharged GFP was not encapsulated. We can also encapsulate GFP within a mutant AfFtn that does not disassemble, which we have recently shown to not encapsulate 6-nm AuNPs, unlike wt (Chapter 2). The cage dynamics perhaps allow for encapsulation of the smaller and more flexible GFP(+36). Encapsulating supercharged proteins within ferritin could be a useful delivery method, rendering the cargo less vulnerable to proteolysis and delivering to specific cells bearing one of several receptors with affinity for ferritin (Scara5[84] or TfR1[83]). The ferritin could also be redirected to a target of choice by conjugating antibodies[88] or targeting peptides to its surface.[89]

5.4 Experimental Procedures

Protein expression and purification. AfFtn and mutants were expressed and purified as described in Chapter 2. SDS-PAGE confirming purity is shown in Figure 5.14.

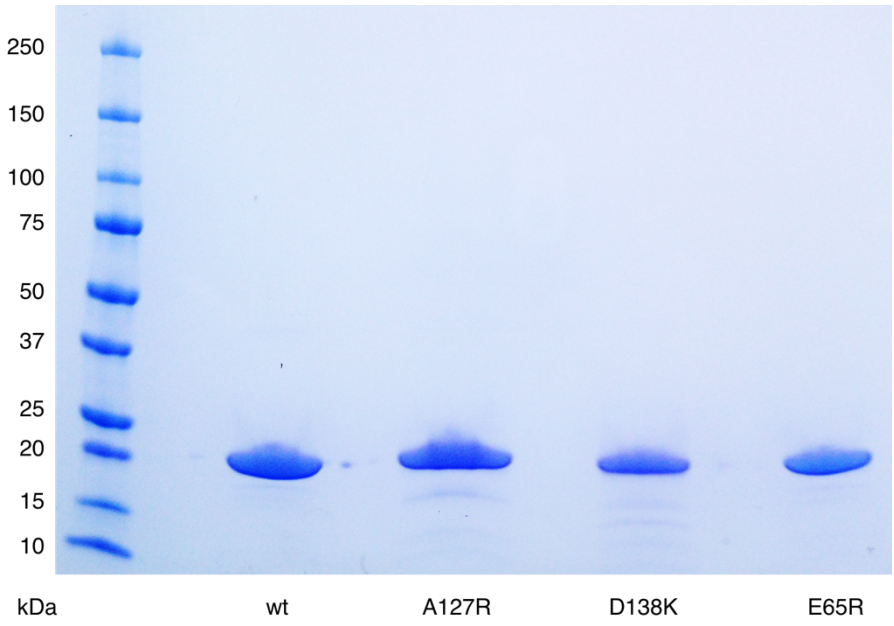

Figure 5.14. SDS-PAGE showing pure protein for AfFtn wt, A127R, D138K, and E65R used.

GFP(+36)-His_6 plasmid was purchased from DNA 2.0 (now ATUM), based on the sequence published by Lawrence et al.[205] Plasmid containing eGFP-His_6 (pUCBB-ntH6-eGFP) was a gift from Claudia Schmidt-dannert (Addgene plasmid #32557).[208] Plasmids were transformed in *E. coli* BL21CodonPlus(DE3)-RP cells. Cells were grown at 30 °C overnight in LB broth, transferred to 1 L LB, and grown at 37 °C until OD_{600} ~0.6. Induction was done with 1 mM IPTG for 4 h at 37 °C. Cells were harvested by centrifugation and stored at -20 °C. Cells were resuspended in lysis buffer (phosphate buffered saline with 2 M NaCl) and lysed by treatment with lysozyme (~1 mg/mL final concentration) and DNAse with stirring at 4 °C for 30 min, followed by sonication on ice

(amplitude of 30, 1 s on, 2 s off, 10 min processing time). Cellular debris were removed by centrifugation (16 krpm, 30 min, 4 °C). Initial purification was performed using Ni-NTA spin columns, washing three times with lysis buffer containing 20 mM imidazole, followed by elution with lysis buffer containing 250 mM imidazole. Green fractions were collected and buffer exchanged to PBS. Benzonase nuclease and $MgCl_2$ (2 mM final concentration) were added and the solution was incubated at rt for 15 min to further remove nucleic acids. Using a HiTrap SP HP column, cation exchange was performed by running a gradient 0-100% over 25 mL using lysis buffer. The sample was then concentrated and run on a HiLoad 16/60 size exclusion column equilibrated with lysis buffer at a flow rate of 0.7 mL/min. Green fractions were collected and concentrated. Purity was verified by SDS-PAGE (Figure 5.15) and concentration was determined using extinction coefficients at 488 nm: 8.33×10^4 M^{-1} cm^{-1} (GFP(+36))[209], 5.3×10^4 M^{-1} cm^{-1} (eGFP).[210]

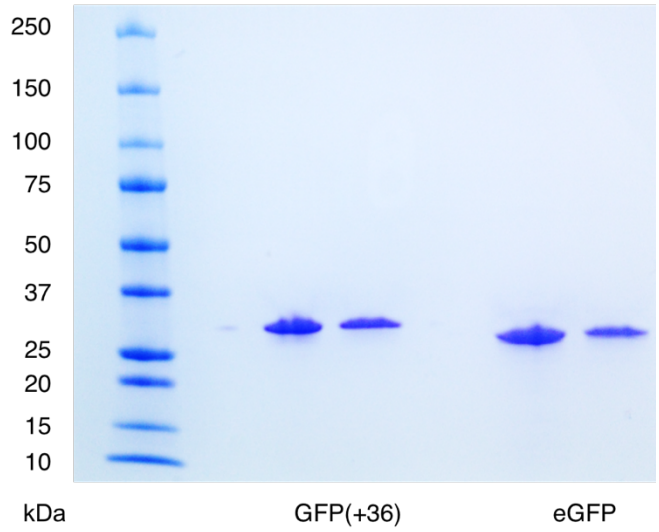

Figure 5.15. SDS-PAGE showing pure protein for GFP(+36), eGFP used.

AfFtn GFP(+36) complex formation. AfFtn-GFP(+36) complexes were formed by mixing AfFtn and GFP(+36) in a 1:1 ratio in no salt buffer (20 mM phos, pH 7.6) at a concentration of 0.6 μM and equilibrating overnight at 4 °C.

Native gel electrophoresis. Native gels (0.7% agarose) were prepared using 5 mM NaCl, 20 mM phos, pH 7.6. Samples were mixed with glycerol (final concentration 16% v/v). Gels were run at 100 V for 20 min on ice, covered with foil. Gels were imaged using a Typhoon FLA7000 imager using an excitation wavelength of 472 nm and PMT setting of 500 V. Following fluorescence imaging, gels were stained with Coomassie Brilliant Blue R-250.

Analytical size exclusion chromatography. Analytical size exclusion chromatography was done on an AKTA FPLC system using a Superdex200 Increase 10/300 GL column equilibrated with no salt buffer (20 mM phos, pH 7.6). Samples were prepared as above, but at a concentration of 6 μM for greater signal. 200 μL of sample was injected and A_{280} was monitored. Sample was eluted at 4 °C using a flow rate of 0.9 mL/min. Fluorescence of individual fractions was measured using a microplate reader as described below.

Dynamic light scattering. 100 μL of sample were pipetted into a disposable micro cuvette. DLS was performed on a Malvern ZetaSizer Nano ZS with a scattering angle of 173 ° at a temperature of 25 °C.

Fluorescence measurements. For GFP(+36) fluorescence spectrum, a Varian Cary Eclipse spectrophotometer was used, exciting at 488 nm and scanning 490-550 nm at 30 nm/min at 25 °C. For fluorescence analysis of size exclusion fractions and Ni-NTA assay

samples, a Tecan M1000 microplate reader was used. 100 μL of sample were pipetted into a black 96-well plate. Samples were excited at 488 nm and fluorescence was measured at 509 nm.

Ni-NTA assay. Fractions from SEC analysis containing encapsulation product were concentrated using a 10k centricon to a volume of ~100 μL. 100 μL of concentrated sample was mixed with 100 μL of Ni-NTA resin that had been pre-washed with no salt buffer (20 mM phos, pH 7.6). Samples were incubated for an hour at 4 °C on an end-over rocker, covered in foil. Post-incubation, samples were centrifuged for 2 min at 13.2 krpm to pellet the resin. The supernatant was moved to a clean tube for later analysis ("load"). The resin was resuspended in lysis buffer containing 20 mM imidazole, centrifuged, and again the supernatant was removed ("wash 1"). This was repeated twice more ("wash 2", "wash 3"). After washing, the resin was resuspended in lysis buffer containing 250 mM imidazole, centrifuged, and the supernatant was removed ("elution 1"). Again, this was repeated twice more ("elution 2", "elution 3"). The fluorescence of all supernatant samples was measured using a microplate reader as described above.

Transmission electron microscopy. Grids were prepared by floating a copper-coated carbon grid on 5 μL of sample and staining with 2% (w/v) uranyl acetate. Grids were imaged on a Tecnai T-12 microscope operating at 120 keV.

Determination of GFP(+36) loading. 1:1 AfFtn:GFP(+36) samples were purified by SEC, and the fraction containing the highest fluorescence intensity was selected for loading analysis. The UV-visible spectrum of the sample was measured using an Agilent 8453 UV-visible spectrometer. A_{280} and A_{488} were used to calculate the number of

GFP(+36) per AfFtn 24mer. The measured A_{280} has contributions from both AfFtn and GFP(+36), while A_{488} is only due to GFP(+36). An average ratio of A_{280}/A_{488} for GFP(+36) was determined to be 0.46. This was used to calculate the A_{280} that can be attributed to AfFtn:

$$A_{280,GFP(+36)} = A_{488} \times 0.46$$

$$A_{280,AfFtn} = A_{280,measured} - A_{280,GFP(+36)}$$

The concentration of AfFtn was then calculated using the extinction coefficient above, while the concentration of GFP(+36) was calculated based on A_{488} and the extinction coefficient listed above. The loading, [GFP(+36)] / [AfFtn], was then calculated.

Geometric analysis of AfFtn pores and GFP(+36). The pores of wt-AfFtn are ~4.5 nm from base to vertex, forming an approximately equilateral triangle with sides of ~5 nm. GFP(+36) can be simplified as a cylinder of length 4 nm and diameter 3 nm. To fit GFP(+36) lengthwise through the pore, its diameter must be smaller than the largest circle that can be inscribed in an equilateral triangle of side length s:

$$d = \frac{s}{\sqrt{3}}$$

For s = 5 nm, d = 2.9 nm, just smaller than the diameter of an idealized GFP(+36) cylinder. To fit GFP(+36) height-wise through the pore, its area if flattened to a rectangle must be smaller than 50% of the area of the triangle pore. This results in an area for a GFP(+36) rectangle of 12 nm^2, while the largest possible rectangle to fit through the pores has an area of 11.25 nm^2. Thus, GFP(+36) should be slightly too large to be encapsulated or escape only via movement through the pores.

5.5 Acknowledgments

This work was supported by NSF grant (PD 09-6885, CHE-1508318) to IJD. We thank Andrew Tsourkas for use of the DLS and the University of Pennsylvania Electron Microscopy Resource Center for use of the TEM.

CHAPTER 6: FUTURE DIRECTIONS AND CONCLUSIONS

The work in this thesis has demonstrated the utility of AfFtn for the encapsulation of useful cargo such as nanoparticles and proteins. We have tuned the self-assembly behaviour of AfFtn via computationally-guided mutagenesis, producing three mutant AfFtn with a gradient of assembly stability. One mutant, E65R, is remarkably more stable with respect to both temperature and ionic strength compared to wt. This mutant may be useful for high temperature templated nanomaterial synthesis or targeted delivery in physiological conditions, where wt AfFtn would disassemble. Probing the bio-nano interface remains non-trivial, but using our graphene-based microelectrode, we have demonstrated that AfFtn maintains its native quaternary structure upon encapsulation of an AuNP. This device could find additional use in probing charge transfer in other protein-nanomaterial systems. We have also developed seeded growth AuNP templating with AfFtn and explored the effect of the gold salt chosen and the AfFtn pore size. Our results demonstrate the advantage of the unique porous structure of AfFtn in achieving high templating efficiency. Finally, we have expanded AfFtn encapsulation beyond nanoparticles to protein cargo using supercharged GFP.

There are many applications that can be realized using the AfFtn-cargo complexes developed herein, such as increasing catalytic specificity of NPs by encapsulating them within AfFtn, delivering therapeutic proteins using antibody-conjugated AfFtn, and templating NP growth. However, potential cargo for encapsulation remains limited by the internal diameter of AfFtn. Only cargo smaller than 8 nm in all dimensions can fit within the cavity, eliminating many NPs whose exotic shapes or larger sizes give them interesting catalytic, therapeutic, or optical properties. Cubic nanoparticles could potentially fit inside AfFtn by positioning the corners in the large triangular pores of the assembled protein.

Platinum nanocubes have been shown to more effectively catalyse oxygen reduction[211] and methanol and ethanol electrooxidation[212] compared to Pt spheres of comparable size. Gold nanorods have significant NIR absorbance and are highly effective photothermal therapy agents for cancer treatment,[59] but the rod width is typically more than 10 nm, and the length is 15-70 nm.[213] Irregularly faceted iron oxide nanoparticles with larger sizes (up to 18 nm) have greater relaxivity and therefore higher contrast for magnetic resonance imaging.[214] Particles with "spiky" surfaces such as spiky gold nanoshells[215] or gold nanostars[216] can be used for surface enhanced Raman scattering. To encapsulate NPs such as these, more extensive engineering of the AfFtn cage is needed.

To increase the versatility of AfFtn for encapsulation, we aim to prepare AfFtns of various sizes, as guided by computation. By inserting additional amino acids into the middle of all four helices, we expect to create AfFtn with larger inner and outer diameters (Figure 6.1).

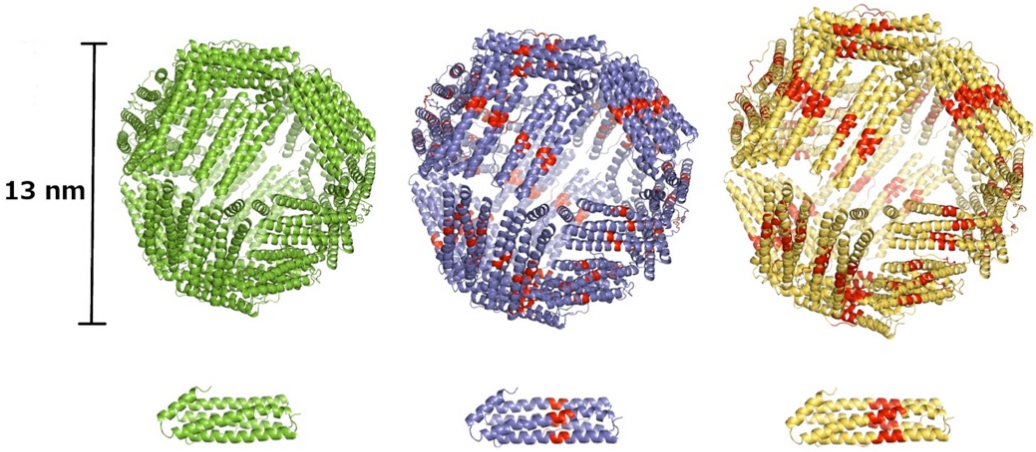

Figure 6.1 Computationally designed ferritins with enlarged cavities will be designed by inserting additional residues into each helix. Figure from Jose Villegas.

Recent work has shown that the ferritin cage is amenable to size manipulation. Mutagenesis studies have led to the formation of non-native ferritin assemblies, with more

or less than the canonical 24 subunits. Somewhat counterintuitively, Zhang et al.[217] created an enlarged 48mer ferritin (17 nm outer diameter) by deleting six amino acids within helix D of human H ferritin. This large ferritin was stable only in the solid phase, while a smaller, disc-like, 8mer ferritin (10 nm outer diameter) was the stable species in solution. By inserting seven amino acids in helix D of human H ferritin, a 16mer ferritin cage was also produced.[218] These studies show that manipulating the ferritin cage is possible, but not always intuitive or predictable. Thus, we plan to carefully redesign helix interfaces to allow for insertion of additional amino acids, while also maintaining the important inter-subunit contacts that promote self-assembly.

In addition to engineering AfFtn, NP surface chemistry will need to be optimized to encapsulate NPs of different compositions and sizes. As the Appendix demonstrates, AfFtn encapsulation is highly dependent on surface ligand, as BSPP and citrate-coated AuNPs were preferentially encapsulated compared to AuNPs coated with GSH. Further studies are needed to understand the specific ligand properties that enable encapsulation and work may be needed to incorporate those properties into a ligand that is compatible with a specific NP surface.

Further development is needed in the encapsulation of supercharged proteins. Our results indicate that GFP(+36) can be encapsulated but non-supercharged eGFP cannot. We are interested in understanding exactly what features are required to nucleate encapsulation; e.g. is a charge of +36 a magic number, or are there other highly charged GFPs that can also be encapsulated? Will a –36 GFP be encapsulated, or is the positive charge important? Based on what we learn using GFP as a model protein, we are interested in encapsulating therapeutically relevant proteins, either by tagging them with a

supercharged protein[14] or a highly charged amino acid tail,[11] or by redesigning the protein surface itself to be intrinsically more charged.[219] We are also interested in exploring what advantages encapsulation within AfFtn might afford a protein, such as enhanced thermal stability or protease resistance. In addition, the confined environment of the AfFtn cavity could be used to mimic cellular crowding for studies of enzyme behavior.

In summary, we have shown AfFtn to be a versatile nanocontainer capable of encapsulating diverse cargo, including metallic and semiconducting NPs and supercharged protein. Our studies demonstrate enhanced control over nanoscale self-assembly, and the resulting AfFtn-cargo conjugates could find future application in catalysis (AfFtn-AuNP), nanomaterials synthesis (AfFtn-AuNP), targeted drug delivery (AfFtn-supercharged therapeutic protein), fundamental enzyme studies (AfFtn-supercharged protein), and bioimaging (AfFtn-QD).

APPENDIX: FERRITIN ENCAPSULATION OF QUANTUM DOTS

A.1 Introduction

Quantum dots (QDs) are semiconducting nanoparticles with unique optical properties that make them highly useful in biological imaging,[220] sensing,[221] and diagnostic applications.[222] Due to quantum confinement, QDs have bright, narrow emission in the visible range.[223] The emission wavelength is dependent on size, with larger particles emitting in the red, and smaller particles emitting in the blue to UV. Their quantum yields and stability against photobleaching are both superior to most organic dyes, making them attractive alternatives for imaging biological samples.[135]

In order for QDs to be widely used in biological applications, greater understanding of their interactions with biomolecules is needed. A number of studies have examined the effects of proteins on QDs, particularly on their optical properties. Surface ligand was found to play a significant role in encapsulating CdSe/ZnS QDs within brome mosaic virus capsid protein assemblies.[7] Only HS-PEG-COOH-coated QDs were encapsulated and remained stable in solution, while dihydrolipoic acid, streptavidin-biotin-DNA, and lipid micelles were all unsuccessful ligands. Upon encapsulation, the PEG-QDs had a slight 3-5 nm red shift in emission and the appearance of a broad shoulder, which was attributed to coupling between multiple QDs encapsulated in the same capsid. A slight blue shift in QD emission was observed for PbS QDs in the presence of HSAF,[224] as well as for CdTe QDs in the presence of denatured BSA[225] and for CdSe QDs with metallothionein metal binding domain peptide.[226] Proteins can also enhance or quench QD fluorescence intensity. CdSe/ZnS QDs in the presence of IgG[227] or maltose binding protein[228] were reported to have increased fluorescence, attributed to fewer surface defects present after protein adsorption. CdSe with maltose binding protein-metallothionein fusion[229] or

metallothionein metal binding domain peptide[226] and CdTe with denatured BSA[225] were also reported to increase in fluorescence intensity. A decrease in fluorescence intensity was reported for CdSe/ZnS in the presence of various peptides.[230]

To generalize the encapsulation of AuNPs to NPs of other compositions, we have attempted to encapsulate CdSe/ZnS/CdS core/shell/shell QDs. CdSe/ZnS QDs have excellent fluorescence properties, while the CdS layer allows greater synthetic control tuning overall particle diameter. In this chapter we discuss our work exploring the interaction between QDs and AfFtn.

A.2 Results and Discussion

Using the same encapsulation process as had been previously used with AuNPs,[51] we mixed AfFtn with CdSe/ZnS/CdS QDs capped with glutathione (GSH). QD surface chemistry is different from that of AuNPs, and initial attempts to stabilize QDs using the same ligand that had shown successful encapsulation previously (BSPP) were not successful. We therefore used GSH instead, which had previously worked in encapsulating 10 nm AuNPs using a thermocycling process.[50] Ferritin secondary structure was essentially unchanged, demonstrating no perturbation to the protein (Figure A.1).

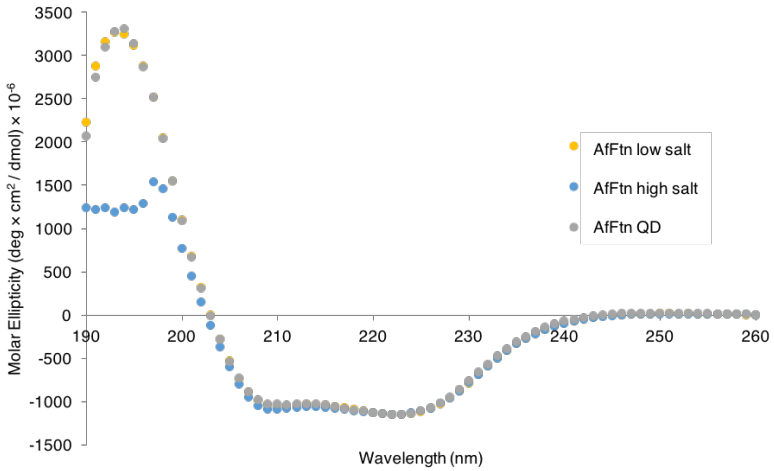

Figure A.1. Circular dichroism spectroscopy of thermophilic ferritin and thermophilic ferritin quantum dot samples.

Using steady state fluorescence spectroscopy, we saw a significant decrease in QD fluorescence in the presence of AfFtn. This decrease continued over time as shown in Figure A.2.

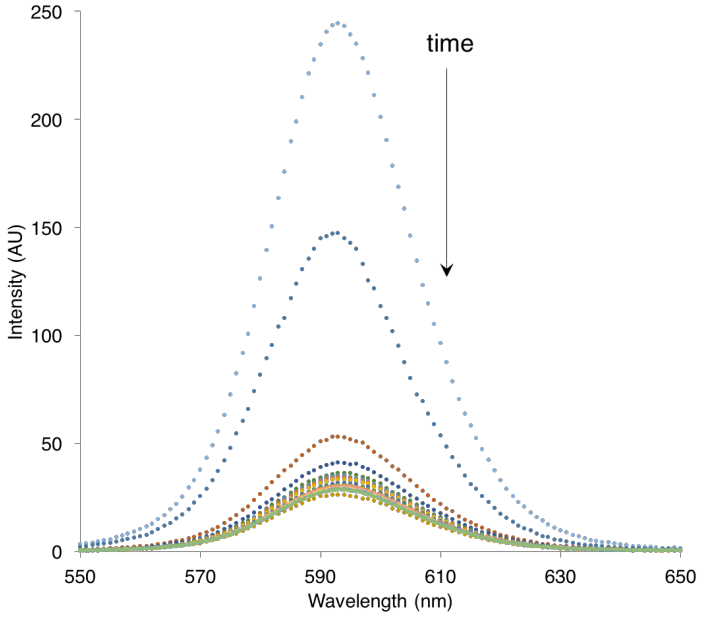

Figure A.2. Steady-state fluorescence data over time showing decrease in QD fluorescence intensity after addition of AfFtn, 0-24 h.

To determine whether this decrease in fluorescence was specific to AfFtn or a phenomenon general to protein adsorption under the encapsulation conditions used, we incubated several other proteins with QDs and measured their fluorescence. The proteins used were bovine gamma globulin (BGG), bovine serum albumin (BSA), conalbumin (con), enhanced green fluorescent protein (eGFP), horse spleen ferritin (HSF), horse spleen apoferritin (HSAF), and fibrinogen (fib).

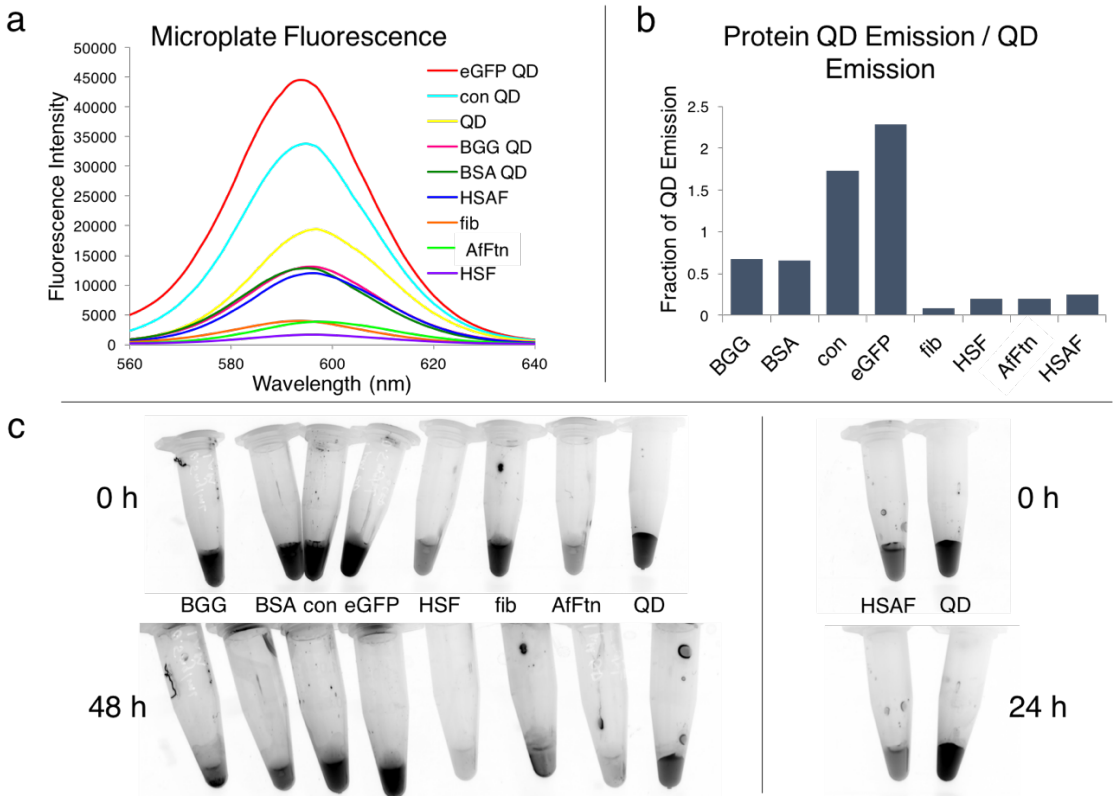

Figure A.3. QD fluorescence in the presence of various proteins. a) Fluorescence of protein QD samples measured on microplate reader. b) Fluorescence intensity of protein QD samples divided by QD fluorescence intensity. c) Samples illuminated by UV lamp showing changes in fluorescence over time for protein QD samples.

BGG and BSA showed slight decreases in fluorescence intensity, con and eGFP showed enhancements in fluorescence (though eGFP has natural fluorescence emission similar in

wavelength to that of the QD), and HSF, HSAF, and fib showed significant decreases in fluorescence intensity. The fib QD sample had obvious precipitation, leading to decreased fluorescence. Fibrinogen is prone to polymerization and likely adsorbed to the QD surface and aggregated with neighboring fib-QDs, also decreasing fluorescence. HSF has an iron core, and metal ions have been shown to quench QD fluorescence.[231] HSAF does not have an iron core and should be metal-free, similar to tF. We confirmed the absence of iron in AfFtn by ICP-OES; thus, metal ions should not be quenching QD fluorescence. Although not obvious by eye, particle destabilization/precipitation could also have contributed to quenching. To test this, we centrifuged a QD and an AfFtn QD sample for several minutes at high speed (>10k rcf) and measured their UV-vis spectra. As shown in Figure A.4, the UV-vis spectra are very similar, indicating that little precipitation occurred. Thus, the decrease in QD fluorescence cannot be explained by particle destabilization by AfFtn and must be occurring through another mechanism. An increase in surface defects leads to decreased QD fluorescence. AfFtn and HSAF could be inducing defects by stripping Cd^{2+} from the QD surface, as ferritins have been shown to bind Cd^{2+} ions.[232]

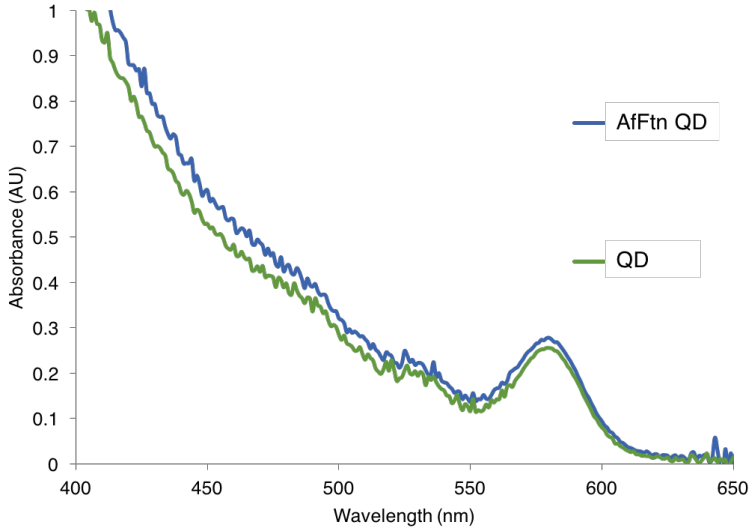

Figure A.4. UV-visible spectra of QD and AfFtn QD samples post-centrifugation. The samples look nearly identical, demonstrating a lack of precipitation.

Based on the changes in QD optical properties, AfFtn was clearly interacting with the QDs in some way. We were interested in exploring whether the QDs were encapsulated by AfFtn. As shown in Figure A.5a, after incubation for 48 h, size exclusion chromatography shows three distinct peaks corresponding to bare QDs, AfFtn 24mer, and AfFtn dimer. This indicated that some encapsulation was occurring. By native agarose gel (Figure A.5b), we also saw some overlap of QD and AfFtn bands after 48 h, though the overlap was not complete. Increasing the concentration of both AfFtn and QD at a 1:1 ratio did not improve encapsulation yield, nor did increasing the amount of AfFtn added (Figure A.6).

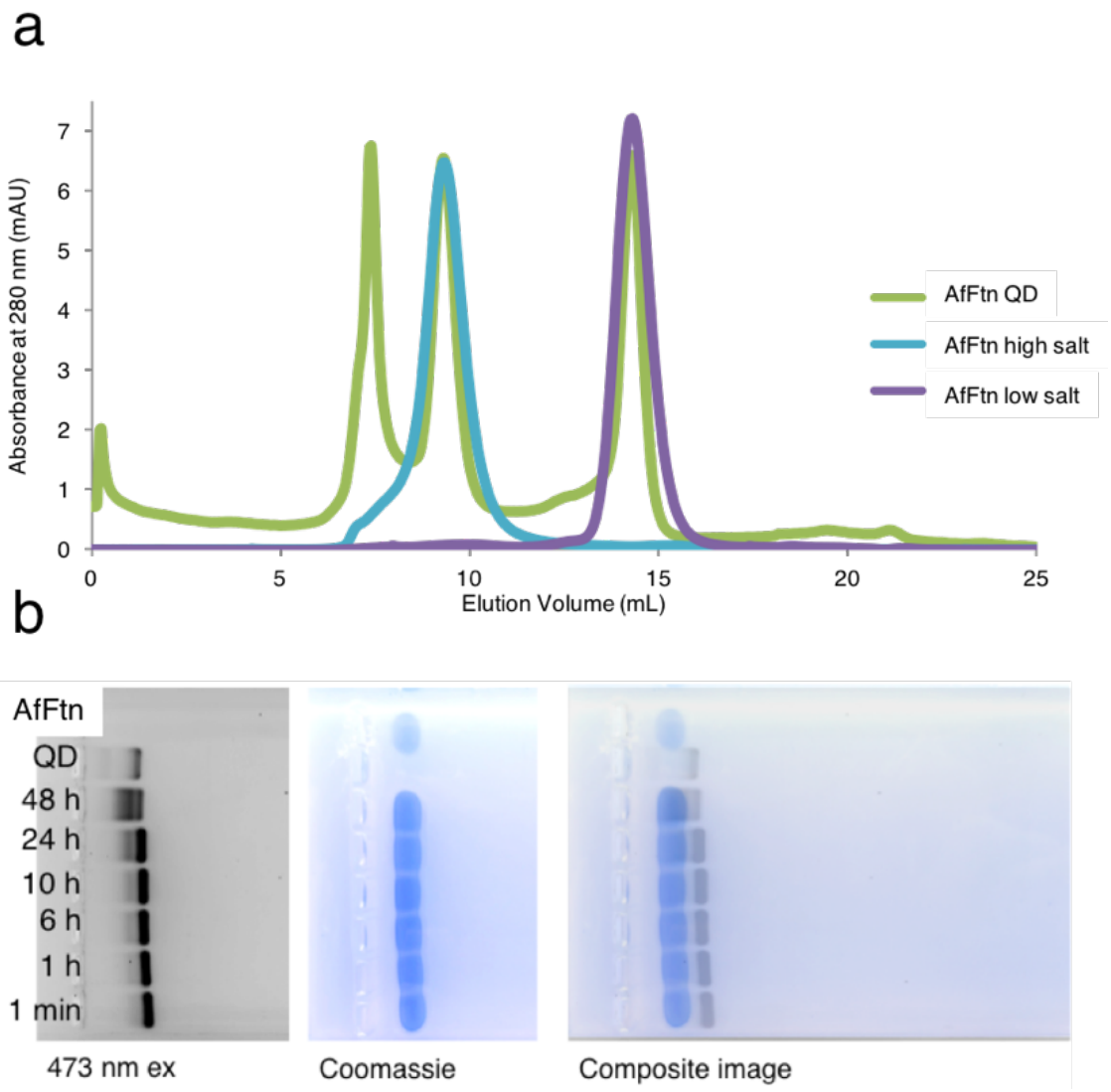

Figure A.5. Exploring encapsulation of QDs by AfFtn. a) Size exclusion chromatography shows three peaks, corresponding to QD alone, AfFtn 24mer, and AfFtn dimer. b) Native gel electrophoresis shows some overlap between AfFtn and QD bands after 48 h, but the overlap is incomplete.

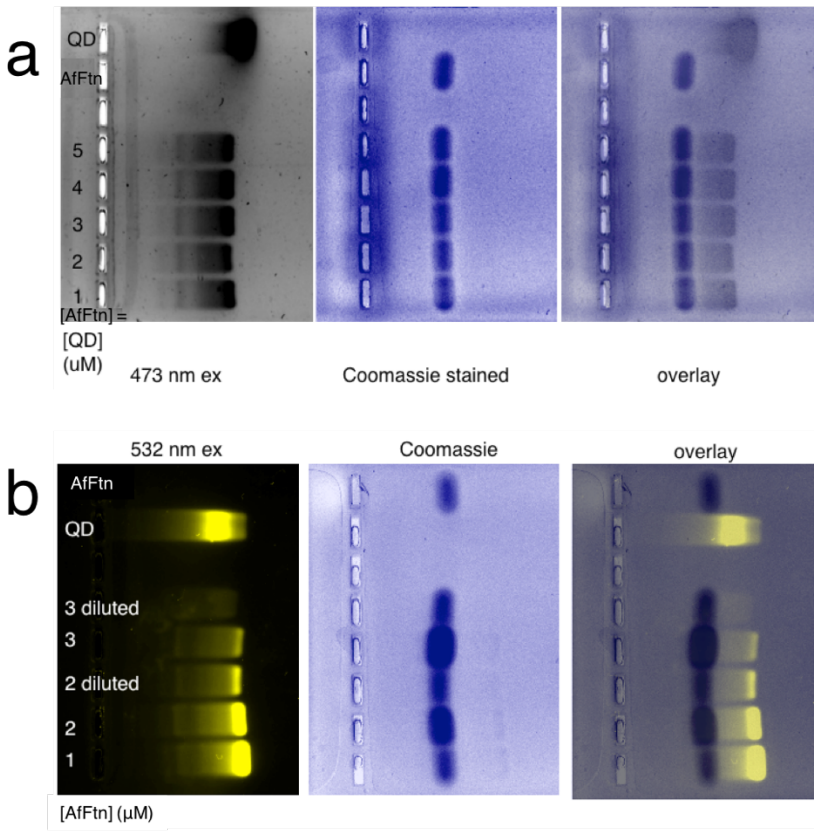

Figure A.6. Native gels varying encapsulation conditions. a) Native gel showing lack of change in encapsulation yield with increasing protein and QD concentration. b) Native gel showing lack of increased encapsulation yield with increasing AfFtn:QD.

In an attempt to improve encapsulation, we used a mutant AfFtn, containing one interior-facing cysteine per monomer ($AfFtn_{1iC}$, E131C mutation). Because sulfur has an affinity for QD surfaces, we hypothesized that $AfFtn_{1iC}$ would interact more strongly with the QD surface and nucleate encapsulation better than wt. We also used different QD ligands, including positively-charged cysteamine (which could interact more favorably with the negatively charged interior of AfFtn), and 4-mercapobenzoic acid (4-MBA, which has more structural similarity to BSPP). To $AfFtn_{1iC}$-containing samples, β-mercaptoethanol (βME) was added to avoid disulfide bond formation, which would link two dimers and potentially prevent proper 24mer assembly. Although initial experiments

suggested encapsulation for cysteamine-coated QDs (Figure A.7a), it was determined that βME was facilitating any movement of the QDs on the gel, and overlap of QD and $AfFtn_{1iC}$ bands was coincidental (Figure A.7b). βME has a free thiol that could be interacting with the QD surface and giving it greater aqueous stability. To verify that its reducing activity was not what was leading to the "encapsulated" band, we used a second reducing agent without a free thiol, tris(2-carboxyethyl)phosphine (TCEP). By native gel, we did not see any apparent encapsulation for $AfFtn_{1iC}$ samples in the presence of TCEP (Figure A.8).

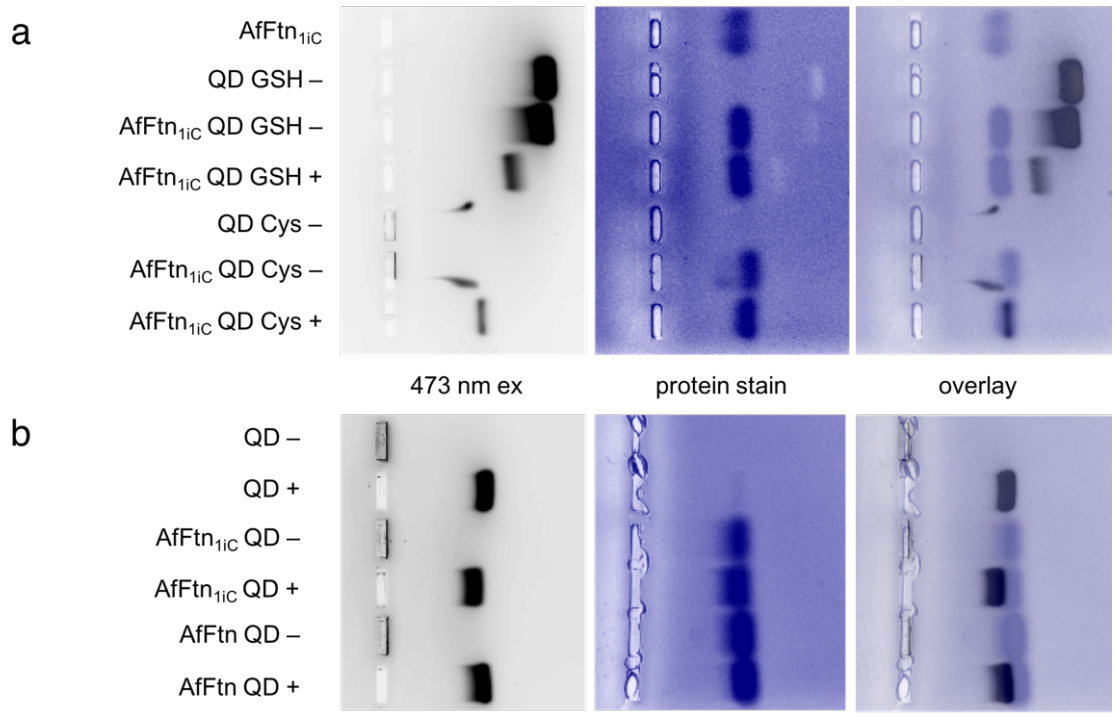

Figure A.7. Native gels in the presence (+) or absence (–) of 1 mM β-mercaptoethanol. a) Apparent encapsulation is seen for AfFtn1ic QD coated with cysteamine in the presence of βME. b) Apparent encapsulation for cysteamine-capped QDs is shown to be coincidental, not unique to $AfFtn_{1iC}$, and dependent on βME.

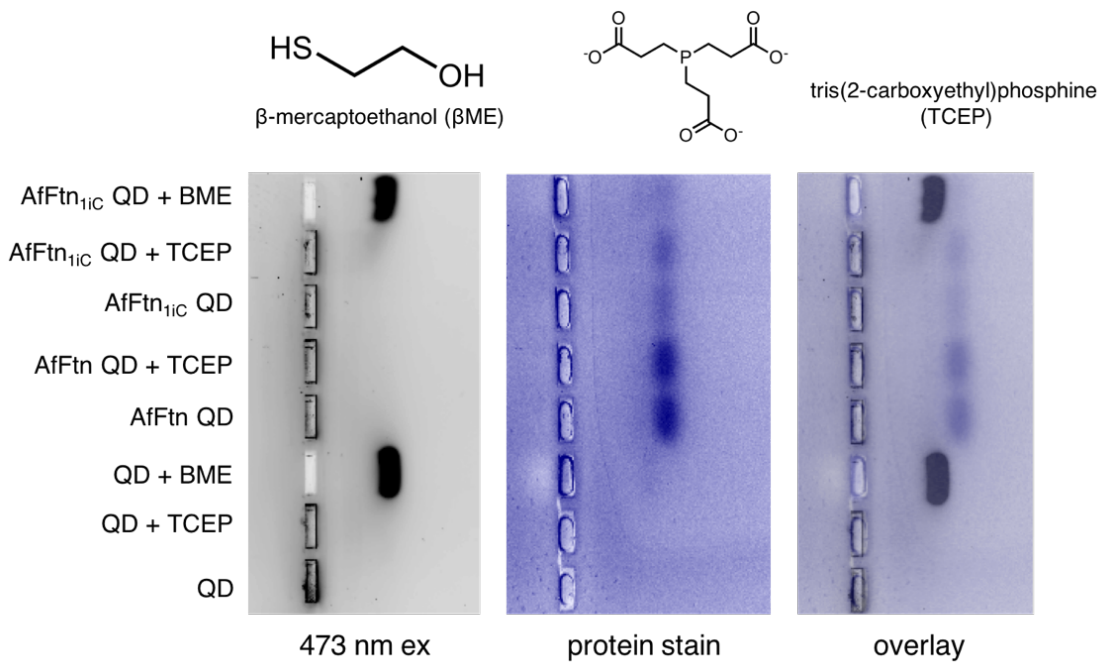

Figure A.8. Native gel comparing βME vs TCEP reducing agents and AfFtn vs $AfFtn_{1iC}$. TCEP-containing ferritin QD samples did not show overlapping ferritin and QD bands, confirming apparent "encapsulation" observed for βME is not due to its reducing capabilities.

To more definitively rule out GSH as a ligand, we tested encapsulation of AuNPs capped with GSH. Native gel showed clearly non-encapsulated AuNP-GSH with our gentle, RT encapsulation method (Figure A.9a), so other QD ligands were attempted. We attempted to use "BSPP-like" ligands that featured an aromatic ring with charged groups, but contained a thiol for conjugation to the QD surface. 4-MBA was used with some success, as the protein and QD bands appeared to overlap by native gel (Figure A.9b). However, ligand exchange with 4-MBA was only partly successful, as the QD fluorescence was significantly diminished post-exchange, and diminished further in the presence of AfFtn.

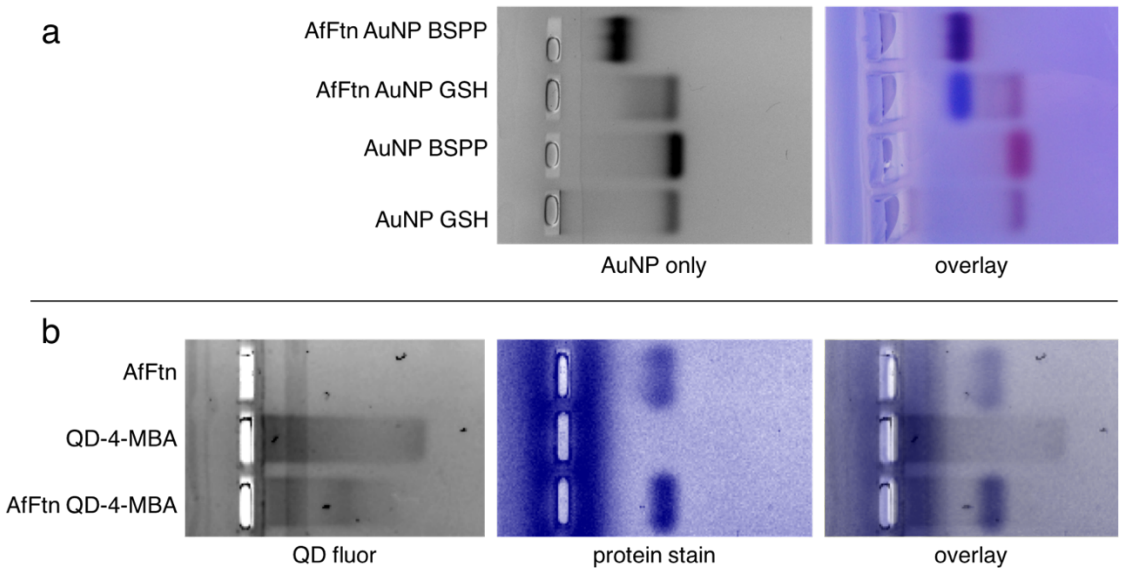

Figure A.9. Native gels varying NP ligand. a) Native gel showing lack of encapsulation for AuNP capped with glutathione (GSH) (red rectangle), compared to AuNPs capped with bis(*p*-sulfonatophenyl)phenylphosphine. b) Native gel showing possible encapsulation for 4-MBA-capped QDs, though QD fluorescence is significantly diminished by this ligand.

A.3 Conclusions

The presence of QDs does not perturb AfFtn structure, though AfFtn does appear to partially quench QD fluorescence. While complete encapsulation is not observed, some interaction between the QDs and AfFtn is occurring, with changes seen in native gel running position, QD fluorescence, and the appearance of AfFtn 24mer by FPLC. Surface ligand has a significant effect on NP interaction with AfFtn as seen by native gel, with AuNP-BSPP showing complete encapsulation and AuNP-GSH showing none. Further work remains to find a ligand that is compatible both with QD surface chemistry and the AfFtn interior.

A.4 Experimental Procedures

AfFtn Expression and Purification. AfFtn was expressed in BL21(DE3)CodonPlus-RP cells cultured in terrific broth medium growing at 37 °C, until

OD ~ 0.6. The bacteria were induced with 1 mM IPTG for 4 h at 37 °C. Cells were lysed by sonication and cellular debris was pelleted by centrifuging at 6 krpm, 4 °C, 30 min. The supernatant was heat shocked for 10 min at 80 °C and centrifuged again, 9 krpm, 4 °C, 90 min. The supernatant was applied to an anion exchange column and fractions containing tF were collected, concentrated, and buffer exchanged into assembly buffer (2 M NaCl, 2 mM EDTA, 20 mM phos, pH 7.6) and incubated overnight at 4 °C. The sample was then concentrated and injected onto a size exclusion Superdex200 10/300 GL column equilibrated with high salt buffer (800 mM NaCl, 20 mM phos, pH 7.6). Fractions containing 24mer were combined and concentrated. Protein purity was assessed using SDS-PAGE and concentration was determined using the Bradford assay.

QD Synthesis and Characterization. QDs were synthesized as previously published[233] and were generously provided by Dr. Matteo Cargnello. Briefly, oleic acid-protected CdSe QDs were prepared using cadmium oleate (0.5 M in 1-octadecene, 1 mmol) and elemental selenium (0.5 mmol) as precursors. After reaction at 240 °C for 30 minutes, $ZnEt_2$ and $(TMS)_2S$ (1 mmol each) dissolved in 6 mL trioctylphosphine were injected using a syringe pump at 0.1 mL min^{-1}. The outer CdS shell was added using $Cd(olac)_2$ (0.5 M in 1-octadecene) and $(TMS)_2S$ (2 mmol each), dissolved into 12 mL of trioctylphosphine and injected at 0.1 mL min^{-1}. The mixture was cooled to RT and QDs isolated and purified by centrifugation using isopropanol and methanol as anti-solvents. For ligand exchange into aqueous solutions, isopropanol and ethanol were used to precipitate 1 mL of QD solution. The solution was centrifuged (8 krcf, 5 min) and resuspended in chloroform. A fresh solution of aqueous ligand (containing 100 mg KOH) was added to the resuspended QDs

and stirred at RT for 1 h. The now aqueous QDs were washed with acetone and water three times and finally stored in water. QDs were characterized by TEM for particle size and UV-vis spectroscopy to monitor ligand effect on QD optical properties (Figure A.10).

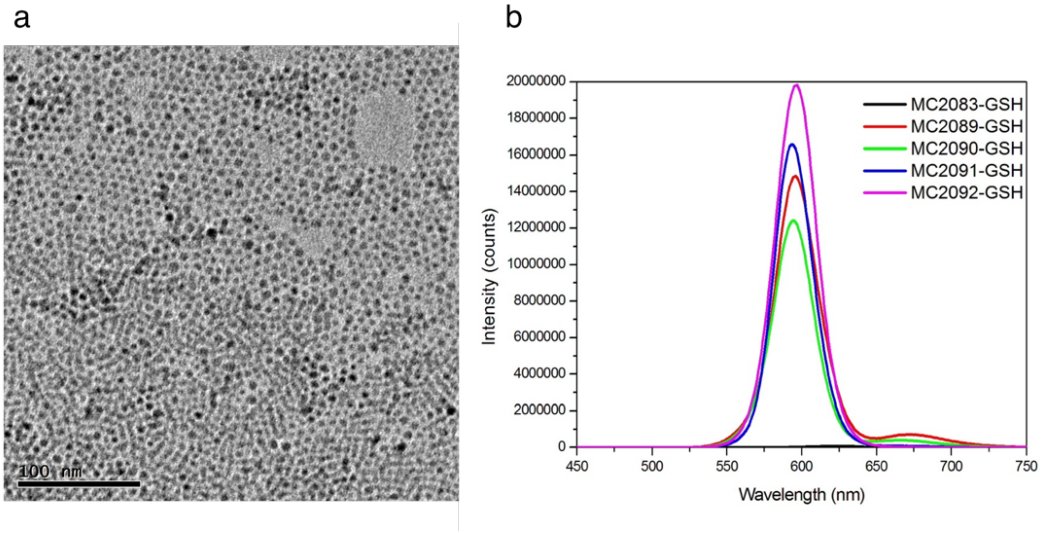

Figure A.10. QD characterization. a) TEM micrograph showing monodisperse particles of 6 nm average diameter. b) Fluorescence spectrum post-ligand exchange to GSH showing emission peak at 590 nm.

AfFtn QD Encapsulation. AfFtn and QDs were mixed at a ratio of 1:1 AfFtn 24mer:QD at a concentration of 1 μM, in low salt buffer (20 mM phos, 20 mM NaCl, pH 7.6), covered in foil, and incubated at RT on a gel rocker for 48 h.

AfFtn QD Characterization. CD data were obtained using an Aviv 410 CD spectrometer (Aviv Biomedical; Lakewood, NJ) with a 1 mm quartz cuvette (Hellma USA). Samples were 0.25 μM in low salt buffer, scanned 190-260 nm, with a 15 s averaging time, at T = 25 °C. Native agarose gels (0.7%) were run at 100 V for 20 min at room temperature, with 5 mM NaCl, 20 mM phos (pH 7.6) as the running buffer. Gels were imaged using a Typhoon FLA7000 Imager exciting at 473 nm to image QD bands and staining with Coomassie dye to visualize AfFtn. Steady-state fluorescence spectra were

collected on a Varian Cary Eclipse fluorescence spectrophotometer (Cary Eclipse software, 2003) using a 100 μL quartz cuvette (Starna Cells). Samples were prepared at 0.6 μM. Samples were excited at 350 nm, scanned 500-700 nm at 30 nm/min, with a PMT voltage of 500 V, at 20 °C. Microplate fluorescence measurements were done on an Infinite M1000 microplate reader (Tecan) using top detection, exciting at 350 nm, scanning 550-650 nm. Analytical size exclusion chromatography was done on a Superdex200 10/300 GL column, equilibrated with low salt buffer (20 mM NaCl, 20 mM phos, pH 7.6). Samples were injected after 48 h incubation at rt with gentle agitation, at a volume of 100 μL. UV-visible absorbance spectra were measured over the range 200–1100 nm at 25 °C using an Agilent 8453 UV-visible spectrometer.

BIBLIOGRAPHY

(1) Dragnea, B.; Chen, C.; Kwak, E.-S.; Stein, B.; Kao, C. C. *J. Am. Chem. Soc.* **2003**, *125* (21), 6374–6375.

(2) Sun, J.; DuFort, C.; Daniel, M.-C.; Murali, A.; Chen, C.; Gopinath, K.; Stein, B.; De, M.; Rotello, V. M.; Holzenburg, A.; Kao, C. C.; Dragnea, B. *Proc. Natl. Acad. Sci. U. S. A.* **2007**, *104* (4), 1354–1359.

(3) Daniel, M. C.; Tsvetkova, I. B.; Quinkert, Z. T.; Murali, A.; De, M.; Rotello, V. M.; Kao, C. C.; Dragnea, B. *ACS Nano* **2010**, *4* (7), 3853–3860.

(4) Aniagyei, S. E.; Kennedy, C. J.; Stein, B.; Willits, D. A.; Douglas, T.; Young, M. J.; De, M.; Rotello, V. M.; Srisathiyanarayanan, D.; Kao, C. C.; Dragnea, B. *Nano Lett.* **2009**, *9* (1), 393–398.

(5) Capehart, S. L.; Coyle, M. P.; Glasgow, J. E.; Francis, M. B. *J. Am. Chem. Soc.* **2013**, *135*, 3011–3016.

(6) Huang, X.; Bronstein, L. M.; Retrum, J.; Dufort, C.; Tsvetkova, I.; Aniagyei, S.; Stein, B.; Stucky, G.; McKenna, B.; Remmes, N.; Baxter, D.; Kao, C. C.; Dragnea, B. *Nano Lett.* **2007**, *7* (8), 2407–2416.

(7) Dixit, S. K.; Goicochea, N. L.; Daniel, M.-C.; Murali, A.; Bronstein, L.; De, M.; Stein, B.; Rotello, V. M.; Kao, C. C.; Dragnea, B. *Nano Lett.* **2006**, *6* (9), 1993–1999.

(8) Worsdorfer, B.; Woycechowsky, K. J.; Hilvert, D. *Science* **2011**, *331*, 589–592.

(9) Azuma, Y.; Zschoche, R.; Tinzl, M.; Hilvert, D. *Angew. Chem. Int. Ed.* **2015**, *55*, 1531–1534.

(10) Zschoche, R.; Hilvert, D. *J. Am. Chem. Soc.* **2015**, *137* (51), 16121–16132.

(11) Seebeck, F. P.; Woycechowsky, K. J.; Zhuang, W.; Rabe, J. P.; Hilvert, D. *J. Am. Chem. Soc.* **2006**, *128* (14), 4516–4517.

(12) Frey, R.; Mantri, S.; Rocca, M.; Hilvert, D. *J. Am. Chem. Soc.* **2016**, *138*, 10072−10075.

(13) Beck, T.; Tetter, S.; Künzle, M.; Hilvert, D. *Angew. Chem. Int. Ed.* **2015**, *127*, 951–954.

(14) Azuma, Y.; Zschoche, R.; Tinzl, M.; Hilvert, D. *Angew. Chem. Int. Ed.* **2016**, *55* (4), 1531–1534.

(15) Webb, B.; Frame, J.; Zhao, Z.; Lee, M. L.; Watt, G. D. *Arch. Biochem. Biophys.* **1994**, *309* (1), 178–183.

(16) Kuruppu, A. I.; Zhang, L.; Collins, H.; Turyanska, L.; Thomas, N. R.; Bradshaw, T. D. *Adv. Healthc. Mater.* **2015**, *4* (18), 2816–2821.

(17) Yan, F.; Zhang, Y.; Kim, K. S.; Yuan, H.-K.; Vo-Dinh, T. *Photochem. Photobiol.* **2010**, *86* (3), 662–666.

(18) Yan, F.; Zhang, Y.; Yuan, H.; Gregas, M. K.; Vo-Dinh, T. *Chem. Commun.* **2008**, 4579–4581.

(19) Huang, P.; Rong, P. F.; Jin, A.; Yan, X. F.; Zhang, M. G.; Lin, J.; Hu, H.; Wang, Z.; Yue, X. Y.; Li, W. W.; Niu, G.; Zeng, W. B.; Wang, W.; Zhou, K. C.; Chen, X. Y. *Adv. Mater.* **2014**, *26* (37), 6401–6408.

(20) Liu, X.; Theil, E. C. *Acc. Chem. Res.* **2005**, *38* (3), 167–175.

(21) Otsuka, S.; Urushizakig, I. *J. Biol. Chem.* **1980**, *255* (12), 6234–6237.

(22) Theil, E. C.; Matzapetakis, M.; Liu, X. *J. Biol. Inorg. Chem.* **2006**, *11* (7), 803–810.

(23) Bevers, L. E.; Theil, E. C. *Prog. Mol. Subcell. Biol.* **2011**, *52*, 29–47.

(24) Theil, E. C. *Annu. Rev. Biochem.* **1987**, *56* (1), 289–315.

(25) Tatur, J.; Hagedoorn, P. L.; Overeijnder, M. L.; Hagen, W. R. *Extremophiles* **2006**, *10* (2), 139–148.

(26) Matias, P. M.; Tatur, J.; Carrondo, M. A.; Hagen, W. R. *Acta Crystallogr. Sect. F Struct. Biol. Cryst. Commun.* **2005**, *61* (5), 503–506.

(27) Tatur, J.; Hagen, W. R.; Matias, P. M. *J. Biol. Inorg. Chem.* **2007**, *12* (5), 615–630.

(28) Zhao, G.; Ceci, P.; Ilari, A.; Giangiacomo, L.; Laue, T. M.; Chiancone, E.; Dennis Chasteen, N. *J. Biol. Chem.* **2002**, *277* (31), 27689–27696.

(29) Grant, R. A.; Filman, D. J.; Finkel, S. E.; Kolter, R.; Hogle, J. M. *Nat. Struct. Biol.* **1998**, *5*, 294–303.

(30) Wolf, S. G.; Frenkiel, D.; Arad, T.; Finkel, S. E.; Kolter, R.; Minsky, A. *Nature* **1999**, *400*, 83–85.

(31) Almiron, M.; Link, A. J.; Furlong, D.; Kolter, R. *Genes Dev.* **1992**, *6*, 2646–2654.

(32) Gerl, M.; Jaenicke, R. *Eur. Biophys. J.* **1987**, *15*, 103–109.

(33) Gerl, M.; Jaenicke, R.; Smith, J. M.; Harrison, P. M. *Biochemistry* **1988**, *27* (11), 4089–4096.

(34) Sato, D.; Ohtomo, H.; Yamada, Y.; Hikima, T.; Kurobe, A.; Fujiwara, K.; Ikeguchi, M. *Biochemistry* **2016**, *55*, 287–293.

(35) Zlotnick, A.; Johnson, J. M.; Wingfield, P. W.; Stahl, S. J.; Endres, D. *Biochemistry* **1999**, *38* (44), 14644–14652.

(36) Tuma, R.; Tsuruta, H.; French, K. H.; Prevelige, P. E. *J. Mol. Biol.* **2008**, *381* (5), 1395–1406.

(37) Zhang, Y.; Fu, J.; Chee, S. Y.; Ang, E. X. W.; Orner, B. P. *Protein Sci.* **2011**, *20* (11), 1907–1917.

(38) Zhang, Y.; Wang, L.; Ardejani, M. S.; Aris, N. F.; Li, X.; Orner, B. P.; Wang, F. *J. Biochem.* **2015**, *158* (6), 505–512.

(39) Ardejani, M. S.; Chok, X. L.; Foo, C. J.; Orner, B. P. *Chem. Commun.* **2013**, *49*, 3528–3530.

(40) Ardejani, M. S.; Li, N. X.; Orner, B. P. *Biochemistry* **2011**, *50*, 4029–4037.

(41) Zhang, Y.; Raudah, S.; Teo, H.; Teo, G. W. S.; Fan, R.; Sun, X.; Orner, B. P. *J. Biol. Chem.* **2010**, *285* (16), 12078–12086.

(42) Ohtomo, H.; Ohtomo, M.; Sato, D.; Kurobe, A.; Sunato, A.; Matsumura, Y.; Kihara, H.; Fujiwara, K.; Ikeguchi, M. *Biochemistry* **2015**, *54*, 6243–6251.

(43) Bernacchioni, C.; Ghini, V.; Pozzi, C.; Di Pisa, F.; Theil, E. C.; Turano, P. *ACS Chem. Biol.* **2014**, *9* (11), 2517–2525.

(44) Chen, H.; Zhang, S.; Xu, C.; Zhao, G. *Chem. Commun.* **2016**, *52*, 7402–7405.

(45) Kim, M.; Rho, Y.; Jin, K. S.; Ahn, B.; Jung, S.; Kim, H.; Ree, M. *Biomacromolecules* **2011**, *12* (5), 1629–1640.

(46) Chiaraluce, R.; Consalvi, V.; Cavallo, S.; Ilari, A.; Stefanini, S.; Chiancone, E. *Eur. J. Biochem.* **2000**, *267* (18), 5733–5741.

(47) Ceci, P.; Ilari, A.; Falvo, E.; Giangiacomo, L.; Chiancone, E. *J. Biol. Chem.* **2005**, *280* (41), 34776–34785.

(48) Huard, D. J. E.; Kane, K. M.; Tezcan, F. A. *Nat. Chem. Biol.* **2013**, *9* (3), 169–176.

(49) Johnson, E.; Cascio, D.; Sawaya, M. R.; Gingery, M.; Schröder, I. *Structure* **2005**, *13* (4), 637–648.

(50) Swift, J.; Butts, C. A.; Cheung-Lau, J.; Yerubandi, V.; Dmochowski, I. J. *Langmuir* **2009**, *25* (9), 5219–5225.

(51) Cheung-Lau, J. C.; Liu, D.; Pulsipher, K. W.; Liu, W.; Dmochowski, I. J. *J. Inorg. Biochem.* **2014**, *130*, 59–68.

(52) Pulsipher, K. W.; Dmochowski, I. J. In *Methods in Molecular Biology*; Orner, B.

P., Ed.; Springer New York: New York, New York, 2014; pp 27–37.

(53) Freestone, I.; Meeks, N.; Sax, M.; Higgitt, C. *Gold Bull.* **2007**, *40*, 270–277.

(54) Faraday, M. *Philos. Trans. R. Soc. London* **1857**, *147* (1857), 145–181.

(55) Kelly, K. L.; Coronado, E.; Zhao, L. L.; Schatz, G. C. *J. Phys. Chem. B* **2003**, *107* (3), 668–677.

(56) Nie, S.; Emory, S. R. *Science* **1997**, *275*, 1102–1106.

(57) Anker, J. N.; Hall, W. P.; Lyandres, O.; Shah, N. C.; Zhao, J.; Van Duyne, R. P. *Nat. Mater.* **2008**, *7* (6), 442–453.

(58) Cao, Y. C.; Jin, R.; Mirkin, C. A. *Science* **2002**, *297*, 1536–1540.

(59) Huang, X. H.; El-Sayed, I. H.; Qian, W.; El-Sayed, M. A. *J. Am. Chem. Soc.* **2006**, *128*, 2115–2120.

(60) Huang, X.; Jain, P. K.; El-Sayed, I. H.; El-Sayed, M. A. *Lasers Med. Sci.* **2008**, *23*, 217–228.

(61) Louie, A. *Chem. Rev.* **2010**, *110* (5), 3146–3195.

(62) Kelkar, S. S.; Reineke, T. M. *Bioconjugate Chem.* **2011**, *22* (10), 1879–1903.

(63) Petros, R. A.; DeSimone, J. M. *Nat. Rev. Drug Discov.* **2010**, *9* (8), 615–627.

(64) Cedervall, T.; Lynch, I.; Lindman, S.; Berggård, T.; Thulin, E.; Nilsson, H.; Dawson, K. A.; Linse, S. *Proc. Natl. Acad. Sci. U. S. A.* **2007**, *104* (7), 2050–2055.

(65) Walkey, C. D.; Chan, W. C. W. *Chem. Soc. Rev.* **2012**, *41* (7), 2780–2799.

(66) Lesniak, A.; Fenaroli, F.; Monopoli, M. P.; Aberg, C.; Dawson, K. A.; Salvati, A. *ACS Nano* **2012**, *6* (7), 5845–5857.

(67) Cukalevski, R.; Lundqvist, M.; Oslakovic, C.; Dahlbäck, B.; Linse, S.; Cedervall, T. *Langmuir* **2011**, *27* (23), 14360–14369.

(68) De, M.; Rotello, V. M. *Chem. Commun.* **2008**, 3504–3506.

(69) Zhang, D.; Neumann, O.; Wang, H.; Yuwono, V. M.; Barhoumi, A.; Perham, M.; Hartgerink, J. D.; Wittung-stafshede, P.; Halas, N. J. *Nano Lett.* **2009**, *9* (2), 666–671.

(70) Deng, Z. J.; Liang, M.; Monteiro, M.; Toth, I.; Minchin, R. F. *Nat. Nanotechnol.* **2011**, *6* (1), 39–44.

(71) Koutsopoulos, S.; Patzscly, K.; Bosker, W. T. E.; Norde, W. *Langmuir* **2007**, *23* (4), 2000–2006.

(72) Canaveras, F.; Madueno, R.; Sevilla, J. M.; Blazquez, M.; Pineda, T. *J. Phys. Chem. C* **2012**, *116*, 10430–10437.

(73) Gebauer, J. S.; Malissek, M.; Simon, S.; Knauer, S. K.; Maskos, M.; Stauber, R. H.; Peukert, W.; Treuel, L. *Langmuir* **2012**, *28* (25), 9673–9679.

(74) Lundqvist, M.; Sethson, I.; Jonsson, B. H. *Langmuir* **2004**, *20* (24), 10639–10647.

(75) Daniel, M.-C.; Tsvetkova, I. B.; Quinkert, Z. T.; Murali, A.; De, M.; Rotello, V. M.; Kao, C. C.; Dragnea, B. *ACS Nano* **2010**, *4* (7), 3853–3860.

(76) Chiu, C.-Y.; Li, Y.; Ruan, L.; Ye, X.; Murray, C. B.; Huang, Y. *Nat. Chem.* **2011**, *3* (5), 393–399.

(77) Chaudhary, A.; Gupta, A.; Khan, S.; Nandi, C. K. *Phys. Chem. Chem. Phys.* **2014**, *16* (38), 20471–20482.

(78) Dominguez-Medina, S.; McDonough, S.; Swanglap, P.; Landes, C. F.; Link, S. *Langmuir* **2012**, *28* (24), 9131–9139.

(79) Pelaz, B.; Maffre, P.; Hartmann, R.; Gallego, M.; de la Fuente, J. M.; Nienhaus, G. U.; Parak, W. J.; Rivera-Fernandez, S. *ACS Nano* **2015**, *9* (7), 6996–7008.

(80) Walkey, C. D.; Olsen, J. B.; Guo, H.; Emili, A.; Chan, W. C. W. *J. Am. Chem. Soc.* **2012**, *134* (4), 2139–2147.

(81) Liu, X.; Wei, W.; Yuan, Q.; Zhang, X.; Li, N.; Du, Y.; Ma, G.; Yan, C.; Ma, D. *Chem. Commun.* **2012**, *48* (26), 3155–3157.

(82) Yang, M.; Fan, Q.; Zhang, R.; Cheng, K.; Yan, J.; Pan, D.; Ma, X.; Lu, A.; Cheng, Z. *Biomaterials* **2015**, *69*, 30–37.

(83) Li, L.; Fang, C. J.; Ryan, J. C.; Niemi, E. C.; Lebrón, J. A.; Björkman, P. J.; Arase, H.; Torti, F. M.; Torti, S. V; Nakamura, M. C.; Seaman, W. E. *Proc. Natl. Acad. Sci. U. S. A.* **2010**, *107* (8), 3505–3510.

(84) Li, J. Y.; Paragas, N.; Ned, R. M.; Qiu, A.; Viltard, M.; Leete, T.; Drexler, I. R.; Chen, X.; Sanna-Cherchi, S.; Mohammed, F.; Williams, D.; Lin, C. S.; Schmidt-Ott, K. M.; Andrews, N. C.; Barasch, J. *Dev. Cell* **2009**, *16* (1), 35–46.

(85) Kalgaonkar, S.; Lönnerdal, B. *J. Nutr. Biochem.* **2009**, *20* (4), 304–311.

(86) Lei, Y.; Hamada, Y.; Li, J.; Cong, L.; Wang, N.; Li, Y.; Zheng, W.; Jiang, X. *J. Control. Release* **2016**, *232*, 131–142.

(87) Zhang, L.; Laug, L.; Münchgesang, W.; Pippel, E.; Gösele, U.; Brandsch, M.; Knez, M. *Nano Lett.* **2010**, *10* (1), 219–223.

(88) Khoshnejad, M.; Shuvaev, V. V.; Pulsipher, K. W.; Dai, C.; Hood, E. D.; Arguiri,

E.; Christofidou-Solomidou, M.; Dmochowski, I. J.; Greineder, C. F.; Muzykantov, V. R. *Bioconjugate Chem.* **2016**, *27*, 628–637.

(89) Uchida, M.; Flenniken, M. L.; Allen, M.; Willits, D. a; Crowley, B. E.; Brumfield, S.; Willis, A. F.; Jackiw, L.; Jutila, M.; Young, M. J.; Douglas, T. *J. Am. Chem. Soc.* **2006**, *128* (51), 16626–16633.

(90) Jeon, J. O.; Kim, S.; Choi, E.; Shin, K.; Cha, K.; So, I.-S.; Kim, S.-J.; Jun, E.; Kim, D.; Ahn, H. J.; Lee, B.-H.; Lee, S.-H.; Kim, I.-S. *ACS Nano* **2013**, *7* (9), 7462–7471.

(91) Kim, S.; Kim, G. S.; Seo, J.; Gowri Rangaswamy, G.; So, I.-S.; Park, R.-W.; Lee, B.-H.; Kim, I.-S. *Biomacromolecules* **2016**, *17* (1), 12–19.

(92) Zhen, Z.; Tang, W.; Guo, C.; Chen, H.; Lin, X.; Liu, G.; Fei, B.; Chen, X.; Xu, B.; Xie, J. *ACS Nano* **2013**, *7* (8), 6988–6996.

(93) Zhen, Z.; Tang, W.; Chen, H.; Lin, X.; Todd, T.; Wang, G.; Cowger, T.; Chen, X.; Xie, J. *ACS Nano* **2013**, *7* (6), 4830–4837.

(94) Fantechi, E.; Innocenti, C.; Zanardelli, M.; Fittipaldi, M.; Falvo, E.; Carbo, M.; Shullani, V.; Di, L.; Mannelli, C.; Ghelardini, C.; Ferretti, A. M.; Ponti, A.; Sangregorio, C.; Ceci, P. *ACS Nano* **2014**, *8* (5), 4705–4719.

(95) Rajendran, P.; Rengarajan, T.; Thangavel, J.; Nishigaki, Y.; Sakthisekaran, D.; Sethi, G.; Nishigaki, I. *Int. J. Biol. Sci.* **2013**, *9* (10), 1057–1069.

(96) Brenner, J. S.; Greineder, C.; Shuvaev, V.; Muzykantov, V. *Expert Opin. Drug Deliv.* **2015**, *12* (2), 239–261.

(97) Kolhar, P.; Anselmo, A. C.; Gupta, V.; Pant, K.; Prabhakarpandian, B.; Ruoslahti, E.; Mitragotri, S. *Proc. Natl. Acad. Sci.* **2013**, *110* (26), 10753–10758.

(98) Zern, B. J.; Chacko, A. M.; Liu, J.; Greineder, C. F.; Blankemeyer, E. R.; Radhakrishnan, R.; Muzykantov, V. *ACS Nano* **2013**, *7* (3), 2461–2469.

(99) Howard, M. D.; Greineder, C. F.; Hood, E. D.; Muzykantov, V. R. *J. Control. Release* **2014**, *177* (1), 34–41.

(100) Yamashita, I.; Kirimura, H.; Okuda, M.; Nishio, K.; Sano, K. I.; Shiba, K.; Hayashi, T.; Hara, M.; Mishima, Y. *Small* **2006**, *2* (10), 1148–1152.

(101) Yang, Z.; Wang, X.; Diao, H.; Zhang, J.; Li, H.; Sun, H.; Guo, Z. *Chem. Commun.* **2007**, *7345* (33), 3453–3455.

(102) Abe, S.; Hirata, K.; Ueno, T.; Morino, K.; Shimizu, N.; Yamamoto, M.; Takata, M.; Yashima, E.; Watanabe, Y. *J. Am. Chem. Soc.* **2009**, *131* (20), 6958–6960.

(103) Ueno, T.; Suzuki, M.; Goto, T.; Matsumoto, T.; Nagayama, K.; Watanabe, Y.

Angew. Chem. Int. Ed. **2004**, *43* (19), 2527–2530.

(104) Meng, F.; Sana, B.; Li, Y.; Liu, Y.; Lim, S.; Chen, X. *Small* **2014**, *10* (2), 277–283.

(105) Kim, M.; Rho, Y.; Jin, K. S.; Ahn, B.; Jung, S.; Kim, H.; Ree, M. *Biomacromolecules* **2011**, *12* (5), 1629–1640.

(106) Zhang, Y.; Orner, B. P. *Int. J. Mol. Sci.* **2011**, *12* (8), 5406–5421.

(107) Sato, D.; Takebe, S.; Kurobe, A.; Ohtomo, H.; Fujiwara, K.; Ikeguchi, M. *Biochemistry* **2016**, *55*, 482–488.

(108) Butts, C. A.; Swift, J.; Kang, S.-G.; Di Costanzo, L.; Christianson, D. W.; Saven, J. G.; Dmochowski, I. J. *Biochemistry* **2008**, *47* (48), 12729–12739.

(109) Swift, J.; Wehbi, W. A.; Kelly, B. D.; Stowell, X. F.; Saven, J. G.; Dmochowski, I. J. *J. Am. Chem. Soc.* **2006**, *128* (22), 6611–6619.

(110) Le Duc, G.; Miladi, I.; Alric, C.; Mowat, P.; Bräuer-Krisch, E.; Bouchet, A.; Khalil, E.; Billotey, C.; Janier, M.; Lux, F.; Epicier, T.; Perriat, P.; Roux, S.; Tillement, O. *ACS Nano* **2011**, *5* (12), 9566–9574.

(111) Schindelin, J.; Rueden, C. T.; Hiner, M. C.; Eliceiri, K. W. *Mol. Reprod. Dev.* **2015**, *82* (7–8), 518–529.

(112) Bakkers, G. R.; Boyerg, R. F. *J. Biol. Chem.* **1986**, *261* (28), 13182–13185.

(113) Voss, N. R.; Gerstein, M. *Nucleic Acids Res.* **2010**, *38*, 555–562.

(114) Pfeiffer, C.; Rehbock, C.; Hühn, D.; Carrillo-Carrion, C.; de Aberasturi, D. J.; Merk, V.; Barcikowski, S.; Parak, W. J. *J. R. Soc. Interface* **2014**, *11* (96), 20130931.

(115) Khare, G.; Nangpal, P.; Tyagi, A. K. *Biochemistry* **2013**, *52* (10), 1694–1704.

(116) Sana, B.; Johnson, E.; Magueres, P. Le; Criswell, A.; Cascio, D.; Lim, S. *J. Biol. Chem.* **2013**, *288* (45), 32663–32672.

(117) Brewer, S. H.; Glomm, W. R.; Johnson, M. C.; Knag, M. K.; Franzen, S. *Langmuir* **2005**, *21* (20), 9303–9307.

(118) Wörsdörfer, B.; Pianowski, Z.; Hilvert, D. *J. Am. Chem. Soc.* **2012**, *134* (2), 909–911.

(119) MacKerell, A. D.; Bashford, D.; Bellott, M.; Dunbrack, R. L.; Evanseck, J. D.; Field, M. J.; Fischer, S.; Gao, J.; Guo, H.; Ha, S.; Joseph-McCarthy, D.; Kuchnir, L.; Kuczera, K.; Lau, F. T.; Mattos, C.; Michnick, S.; Ngo, T.; Nguyen, D. T.; Prodhom, B.; Reiher, W. E.; Roux, B.; Schlenkrich, M.; Smith, J. C.; Stote, R.;

Straub, J.; Watanabe, M.; Wiorkiewicz-Kuczera, J.; Yin, D.; Karplus, M. *J. Phys. Chem. B* **1998**, *102* (18), 3586–3616.

(120) Dunbrack Jr., R. L. *Curr. Opin. Struct. Biol.* **2002**, *12* (4), 431–440.

(121) Kono, H.; Saven, J. G. *J. Mol. Biol.* **2001**, *306* (3), 607–628.

(122) Bender, G. M.; Lehmann, A.; Zou, H.; Cheng, H.; Fry, H. C.; Engel, D.; Therien, M. J.; Blasie, J. K.; Roder, H.; Saven, J. G.; DeGrado, W. F. *J. Am. Chem. Soc.* **2007**, *129* (35), 10732–10740.

(123) Calhoun, J. R.; Kono, H.; Lahr, S.; Wang, W.; DeGrado, W. F.; Saven, J. G. *J. Mol. Biol.* **2003**, *334* (5), 1101–1115.

(124) Fry, H. C.; Lehmann, A.; Sinks, L. E.; Asselberghs, I.; Tronin, A.; Krishnan, V.; Blasie, J. K.; Clays, K.; DeGrado, W. F.; Saven, J. G.; Therien, M. J. *J. Am. Chem. Soc.* **2013**, *135* (37), 13914–13926.

(125) Battye, T. G. G.; Kontogiannis, L.; Johnson, O.; Powell, H. R.; Leslie, A. G. W. *Acta Crystallogr. D. Biol. Crystallogr.* **2011**, *67*, 271–281.

(126) Evans, P. R. *Acta Crystallogr. D. Biol. Crystallogr.* **2011**, *67*, 282–292.

(127) Winn, M. D.; Ballard, C.; Cowtan, K. D.; Dodson, E. J.; Emsley, P.; Evans, P. R.; Keegan, R. M.; Krissinel, E. B.; Leslie, A. G. W.; McCoy, A.; McNicholas, S. J.; Murshudov, G. N.; Pannu, N. S.; Potterton, E. A.; Powell, H. R.; Read, R. J.; Vagin, A.; Wilson, K. S. *Acta Crystallogr. D. Biol. Crystallogr.* **2011**, *67*, 235–242.

(128) Adams, P. D.; Afonine, P. V; Bunkóczi, G.; Chen, V. B.; Davis, I. W.; Echols, N.; Headd, J. J.; Hung, L.-W.; Kapral, G. J.; Grosse-Kunstleve, R. W.; McCoy, A. J.; Moriarty, N. W.; Oeffner, R.; Read, R. J.; Richardson, D. C.; Richardson, J. S.; Terwilliger, T. C.; Zwart, P. H. *Acta Crystallogr. D. Biol. Crystallogr.* **2010**, *66*, 213–221.

(129) McCoy, A. J.; Grosse-Kunstleve, R. W.; Adams, P. D.; Winn, M. D.; Storoni, L. C.; Read, R. J. J. *Appl. Crystallogr.* **2007**, *40*, 658–674.

(130) Afonine, P. V; Grosse-Kunstleve, R. W.; Echols, N.; Headd, J. J.; Moriarty, N. W.; Mustyakimov, M.; Terwilliger, T. C.; Urzhumtsev, A.; Zwart, P. H.; Adams, P. D. *Acta Crystallogr. D. Biol. Crystallogr.* **2012**, *68*, 352–367.

(131) Emsley, P.; Lohkamp, B.; Scott, W. G.; Cowtan, K. *Acta Crystallogr. Sect. D Biol. Crystallogr.* **2010**, *66*, 486–501.

(132) Chen, V. B.; Arendall, W. B.; Headd, J. J.; Keedy, D. A.; Immormino, R. M.; Kapral, G. J.; Murray, L. W.; Richardson, J. S.; Richardson, D. C. *Acta Crystallogr. D. Biol. Crystallogr.* **2010**, *66*, 12–21.

(133) Schrodinger, LLC.

(134) Kumar, S.; Aaron, J.; Sokolov, K. **2008**.

(135) Medintz, I. L.; Uyeda, H. T.; Goldman, E. R.; Mattoussi, H. *Nat. Mater.* **2005**, *4* (6), 435–446.

(136) Rana, S.; Le, N. D. B.; Mout, R.; Saha, K.; Tonga, G. Y.; Bain, R. E. S.; Miranda, O. R.; Rotello, C. M.; Rotello, V. M. *Nat. Nanotechnol.* **2014**, *10* (1), 65–69.

(137) Suzuki, Y.; Cardone, G.; Restrepo, D.; Zavattieri, P. D.; Baker, T. S.; Tezcan, F. A. *Nature* **2016**, *533*, 369–373.

(138) Nel, A. E.; Mädler, L.; Velegol, D.; Xia, T.; Hoek, E. M. V; Somasundaran, P.; Klaessig, F.; Castranova, V.; Thompson, M. *Nat. Mater.* **2009**, *8* (7), 543–557.

(139) Lundqvist, M.; Stigler, J.; Elia, G.; Lynch, I.; Cedervall, T.; Dawson, K. A. *Proc. Natl. Acad. Sci. U. S. A.* **2008**, *105* (38), 14265–14270.

(140) Theil, E. C.; Tosha, T.; Behera, R. K. *Acc. Chem. Res.* **2016**, *49* (5), 784–791.

(141) Uchida, M.; Kang, S.; Reichhardt, C.; Harlen, K.; Douglas, T. *Biochim. Biophys. Acta* **2010**, *1800* (8), 834–845.

(142) Ping, J.; Johnson, A. T. C. *Appl. Phys. Lett.* **2016**, *109* (1), 13103.

(143) Qi, Z. J.; Rodriguez-Manzo, J. A.; Botello-Mendez, A. R.; Hong, S. J.; Stach, E. A.; Park, Y. W.; Charlier, J.-C.; Drndic, M.; Johnson, A. T. C. *Nano Lett.* **2014**, *14* (8), 4238–4244.

(144) Luo, Y.; Ergenekan, C. E.; Fischer, J. T.; Tan, M.-L.; Ichiye, T. *Biophys. J.* **2010**, *98* (4), 560–568.

(145) Israelachvili, J. *Intermolecular and Surface Forces: Revised Third Edition*; Academic Press, 2011.

(146) Wang, C.; Yang, C.; Song, Y.; Gao, W.; Xia, X. *Adv. Funct. Mater.* **2005**, *15* (8), 1267–1275.

(147) Kim, B. S.; Hayes, R. A.; Ralston, J. *Carbon N. Y.* **1995**, *33* (1), 25–34.

(148) Ping, J.; Xi, J.; Saven, J. G.; Liu, R.; Johnson, A. T. C. *Biosens. Bioelectron.* **2017**, *89*, 689–692.

(149) Park, J.; Choi, S.; Kim, T.-I.; Kim, Y. *Analyst* **2012**, *137* (19), 4411–4414.

(150) Esumi, K.; Miyamoto, K.; Yoshimura, T. *J. Colloid Interface Sci.* **2002**, *254*, 402–405.

(151) Zuber, A.; Purdey, M.; Schartner, E.; Forbes, C.; Van Der Hoek, B.; Giles, D.;

Abell, A.; Monro, T.; Ebendorff-Heidepriem, H. *Sensors Actuators, B Chem.* **2016**, *227*, 117–127.

(152) Zhen, Z.; Tang, W.; Chuang, Y. J.; Todd, T.; Zhang, W.; Lin, X.; Niu, G.; Liu, G.; Wang, L.; Pan, Z.; Chen, X.; Xie, J. *ACS Nano* **2014**, *8* (6), 6004–6013.

(153) Aime, S.; Frullano, L.; Crich, S. G. *Angew. Chem. Int. Ed.* **2002**, *41* (6), 1017–1019.

(154) Sun, C.; Yang, H.; Yuan, Y.; Tian, X.; Wang, L.; Guo, Y.; Xu, L.; Lei, J.; Gao, N.; Anderson, G. J.; Liang, X.-J.; Chen, C.; Zhao, Y.; Nie, G. *J. Am. Chem. Soc.* **2011**, *133* (22), 8617–8624.

(155) Kasyutich, O.; Ilari, A.; Fiohllo, A.; Tatchev, D.; Hoell, A.; Ceci, P. *J. Am. Chem. Soc.* **2010**, *132* (10), 3621–3627.

(156) Fujita, K.; Tanaka, Y.; Sho, T.; Ozeki, S.; Abe, S.; Hikage, T.; Kuchimaru, T.; Kizaka-Kondoh, S.; Ueno, T. *J. Am. Chem. Soc.* **2014**, *136*, 16902–16908.

(157) Meldrum, F. C.; Wade, V. J.; Nimmo, D. L.; Heywood, B. R.; Mann, S. *Nature* **1991**, *349*, 684–687.

(158) Iwahori, K.; Yoshizawa, K.; Muraoka, M.; Yamashita, I. *Inorg. Chem.* **2005**, *44* (18), 6393–6400.

(159) Iwahori, K.; Enomoto, T.; Furusho, H.; Miura, A.; Nishio, K.; Mishima, Y.; Yamashita, I. *Chem. Mater.* **2007**, *19* (13), 3105–3111.

(160) Okuda, M.; Suzumoto, Y.; Iwahori, K.; Kang, S.; Uchida, M.; Douglas, T.; Yamashita, I. *Chem. Commun.* **2010**, *46*, 8797–8799.

(161) Okuda, M.; Suzumoto, Y.; Yamashita, I. *Cryst. Growth Des.* **2011**, *11* (6), 2540–2545.

(162) Suzuki, M.; Abe, M.; Ueno, T.; Abe, S.; Goto, T.; Toda, Y.; Akita, T.; Yamada, Y.; Watanabe, Y. *Chem. Commun.* **2009**, 4871–4873.

(163) Zhang, L.; Swift, J.; Butts, C. A.; Yerubandi, V.; Dmochowski, I. J. *J. Inorg. Biochem.* **2007**, *101*, 1719–1729.

(164) Dominguez-Vera, J. M.; Galvez, N.; Sanchez, P.; Mota, A. J.; Trasobares, S.; Hernandez, J. C.; Calvino, J. J. *Eur. J. Inorg. Chem.* **2007**, 4823–4826.

(165) Galvez, N.; Sanchez, P.; Dominguez-Vera, J. M.; Soriano-Portillo, A.; Clemente-Leon, M.; Coronado, E. *J. Mater. Chem.* **2006**, *16* (26), 2757–2761.

(166) Meldrum, F. C.; Heywood, B. R.; Mann, S. *Science* **1992**, *257* (5069), 522–523.

(167) Wong, K. K. W.; Douglas, T.; Gider, S.; Awschalom, D. D.; Mann, S. *Chem.*

Mater. **1998**, *10*, 279–285.

(168) Cao, C.; Tian, L.; Liu, Q.; Liu, W.; Chen, G.; Pan, Y. *J. Geophys. Res. Solid Earth* **2010**, *115*, 1–10.

(169) Fan, R.; Chew, S. W.; Cheong, V. V.; Orner, B. P. *Small* **2010**, *6* (14), 1483–1487.

(170) Usher, A.; McPhail, D. C.; Brugger, J. *Geochim. Cosmochim. Acta* **2009**, *73* (11), 3359–3380.

(171) Clark, E. S.; Templeton, D. H.; MacGillavry, C. H. *Acta Crystallogr.* **1958**, *11* (4), 284–288.

(172) Lemke, K. H. *Phys. Chem. Chem. Phys.* **2014**, *16* (17), 7813–7822.

(173) Zhu, S.; Gorski, W.; Powell, D. R.; Walmsley, J. A. *Inorg. Chem.* **2006**, *45* (6), 2688–2694.

(174) Kreyling, W. G.; Fertsch-Gapp, S.; Schaffler, M.; Johnston, B. D.; Haberl, N.; Pfeiffer, C.; Diendorf, J.; Schleh, C.; Hirn, S.; Semmler-Behnke, M.; Epple, M.; Parak, W. J. *Beilstein J. Nanotechnol.* **2014**, *5* (1), 1699–1711.

(175) Focsan, M.; Gabudean, A. M.; Canpean, V.; Maniu, D.; Astilean, S. *Mater. Chem. Phys.* **2011**, *129*, 939–942.

(176) Singh, A. V.; Bandgar, B. M.; Kasture, M.; Prasad, B. L. V.; Sastry, M. *J. Mater. Chem.* **2005**, *15*, 5115–5121.

(177) Murawala, P.; Phadnis, S. M.; Bhonde, R. R.; Prasad, B. L. V. *Colloids Surf., B* **2009**, *73*, 224–228.

(178) Pourbaix, M. *Atlas of Electrochemical Equilibra in Aqueous Solutions*; Pergamon: New York, New York, 1966.

(179) Latimer, W. M. *The Oxidation States of the Elements and Their Potentials in Aqueous Solutions*; Prentice-Hall: Englewood Cliffs, New Jersey, 1985.

(180) Purdie, N.; Swallows, K. A. *J. Agric. Food Chem.* **1991**, *39*, 2171–2175.

(181) Maeland, A.; Flanagan, T. B. *Can. J. Phys.* **1964**, *42*, 2364–2366.

(182) Calisti, L.; Benni, I.; Cardoso, M.; Baiocco, P.; Ruzicka, B.; Boffi, A.; Falvo, E.; Malatesta, F.; Bonamore, A. *Biochim. Biophys. Acta* **2017**, *1861*, 450–456.

(183) Keyes, J. D.; Hilton, R. J.; Farrer, J.; Watt, R. K. *J. Nanoparticle Res.* **2011**, *13* (6), 2563–2575.

(184) Maity, B.; Abe, S.; Ueno, T. *Nat. Commun.* **2017**, *8*, 14820.

(185) Tan, Y. N.; Lee, J. Y.; Wang, D. I. C. *J. Am. Chem. Soc.* **2010**, *132* (16), 5677–

5686.

(186) Zhu, S.; Gorski, W.; Powell, D. R.; Walmsley, J. A. *Inorg. Chem.* **2006**, *45* (6), 2688–2694.

(187) Biros, S. M.; Rebek, J. *Chem. Soc. Rev.* **2007**, *36* (1), 93–104.

(188) Sun, X.; James, T. D. *Chem. Rev.* **2015**, *115* (15), 8001–8037.

(189) Wang, Z. J.; Clary, K. N.; Bergman, R. G.; Raymond, K. N.; Toste, F. D. *Nat. Chem.* **2013**, *5* (2), 100–103.

(190) Harada, A.; Hashidzume, A.; Yamaguchi, H.; Takashima, Y. *Chem. Rev.* **2009**, *109*, 5974–6023.

(191) Hu, Q. Da; Tang, G. P.; Chu, P. K. *Acc. Chem. Res.* **2014**, *47* (7), 2017–2025.

(192) Hu, Y.; Yuan, W.; Zhao, N. N.; Ma, J.; Yang, W. T.; Xu, F. J. *Biomaterials* **2013**, *34* (21), 5411–5422.

(193) Hu, Q.; Li, W.; Hu, X.; Hu, Q.; Shen, J.; Jin, X.; Zhou, J.; Tang, G.; Chu, P. K. *Biomaterials* **2012**, *33* (27), 6580–6591.

(194) Assaf, K. I.; Nau, W. M. *Chem. Soc. Rev.* **2015**, *44* (2), 394–418.

(195) Nimse, S. B.; Kim, T. *Chem. Soc. Rev.* **2013**, *42*, 366–386.

(196) Hendrick, J. P.; Hartl, F.-U. *FASEB J.* **1995**, *9* (15), 1559–1569.

(197) Corchero, J. L.; Cedano, J. *Microb. Cell Fact.* **2011**, *10* (1), 92.

(198) Glasgow, J. E.; Capehart, S. L.; Francis, M. B.; Tullman-Ercek, D. *ACS Nano* **2012**, *6* (10), 8658–8664.

(199) Rurup, W. F.; Verbij, F.; Koay, M. S. T.; Blum, C.; Subramaniam, V.; Cornelissen, J. J. L. M. *Biomacromolecules* **2014**, *15* (2), 558–563.

(200) Qazi, S.; Miettinen, H. M.; Wilkinson, R. A.; McCoy, K.; Douglas, T.; Wiedenheft, B. *Mol. Pharm.* **2016**, *13* (3), 1191–1196.

(201) Comellas-Aragonès, M.; Engelkamp, H.; Claessen, V. I.; Sommerdijk, N. A. J. M.; Rowan, A. E.; Christianen, P. C. M.; Maan, J. C.; Verduin, B. J. M.; Cornelissen, J. J. L. M.; Nolte, R. J. M. *Nat. Nanotechnol.* **2007**, *2* (10), 635–639.

(202) Patterson, D. P.; Prevelige, P. E.; Douglas, T. *ACS Nano* **2012**, *6* (6), 5000–5009.

(203) Patterson, D. P.; Schwarz, B.; Waters, R. S.; Gedeon, T.; Douglas, T. *ACS Chem. Biol.* **2014**, *9* (2), 359–365.

(204) Ni, T. W.; Tezcan, F. A. *Angew. Chem. Int. Ed.* **2010**, *49*, 1–6.

(205) Lawrence, M. S.; Phillips, K. J.; Liu, D. R. *J. Am. Chem. Soc.* **2007**, *129* (33), 10110–10112.

(206) Sasaki, E.; Böhringer, D.; van de Waterbeemd, M.; Leibundgut, M.; Zschoche, R.; Heck, A. J. R.; Ban, N.; Hilvert, D. *Nat. Commun.* **2017**, *8*, 14663.

(207) Zhang, G.; Gurtu, V.; Kain, S. R. *Biochem. Biophys. Res. Commun.* **1996**, *227*, 707–711.

(208) Vick, J. E.; Johnson, E. T.; Choudhary, S.; Bloch, S. E.; Lopez-Gallego, F.; Srivastava, P.; Tikh, I. B.; Wawrzyn, G. T.; Schmidt-Dannert, C. *Appl. Microbiol. Biotechnol.* **2011**, *92* (6), 1275–1286.

(209) McNaughton, B. R.; Cronican, J. J.; Thompson, D. B.; Liu, D. R. *Proc. Natl. Acad. Sci. U. S. A.* **2009**, *106* (15), 6111–6116.

(210) Patterson, G. H.; Knobel, S. M.; Sharif, W. D.; Kain, S. R.; Piston, D. W. *Biophys. J.* **1997**, *73* (5), 2782–2790.

(211) Wang, C.; Daimon, H.; Lee, Y.; Kim, J.; Sun, S. *J. Am. Chem. Soc.* **2007**, *129* (22), 6974–6975.

(212) Han, S. B.; Song, Y. J.; Lee, J. M.; Kim, J. Y.; Park, K. W. *Electrochem. commun.* **2008**, *10* (7), 1044–1047.

(213) Ye, X.; Jin, L.; Caglayan, H.; Chen, J.; Xing, G.; Zheng, C. *ACS Nano* **2012**, *6*, 2804–2817.

(214) Smolensky, E. D.; Park, H. E.; Zhou, Y.; Rolla, G. A.; Marjańska, M.; Botta, M.; Pierre, V. C. *J. Mater. Chem. B* **2013**, *1* (22), 2818–2828.

(215) Sanchez-Gaytan, B. L.; Swanglap, P.; Lamkin, T. J.; Hickey, R. J.; Fakhraai, Z.; Link, S.; Park, S. J. *J. Phys. Chem. C* **2012**, *116* (18), 10318–10324.

(216) Guerrero-Martínez, A.; Barbosa, S.; Pastoriza-Santos, I.; Liz-Marzán, L. M. *Curr. Opin. Colloid Interface Sci.* **2011**, *16* (2), 118–127.

(217) Zhang, S.; Zang, J.; Zhang, X.; Chen, H.; Mikami, B.; Zhao, G. *ACS Nano* **2016**, *10*, 10382–10388.

(218) Zhang, S.; Zang, J.; Wang, W.; Chen, H.; Zhang, X.; Wang, F.; Wang, H.; Zhao, G. *Angew. Chem. Int. Ed.* **2016**, 1–8.

(219) Thompson, D. B.; Cronican, J. J.; Liu, D. R. In *Methods in Enzymology*; Elsevier Inc., 2012; Vol. 503, pp 293–319.

(220) Ballou, B.; Lagerholm, B. C.; Ernst, L. A.; Bruchez, M. P.; Waggoner, A. S. *Bioconjugate Chem.* **2004**, *15* (1), 79–86.

(221) Xia, Y. S.; Zhu, C. Q. *Talanta* **2008**, *75* (1), 215–221.

(222) Pisanic, T. R.; Zhang, Y.; Wang, T. H. *Analyst* **2014**, *139*, 2968–2981.

(223) Murray, C. B.; Kagan, C. R.; Bawendi, M. G. *Annu. Rev. Mater. Sci.* **2000**, *30*, 545–610.

(224) Hennequin, B.; Turyanska, L.; Ben, T.; Beltrán, A. M.; Molina, S. I.; Li, M.; Mann, S.; Patanè, A.; Thomas, N. R. *Adv. Mater.* **2008**, *20* (19), 3592–3596.

(225) Wang, Q.; Kuo, Y.; Wang, Y.; Shin, G.; Ruengruglikit, C.; Huang, Q. *J. Phys. Chem. B* **2006**, *110* (34), 16860–16866.

(226) Aryal, B. P.; Neupane, K. P.; Sandros, M. G.; Benson, D. E. *Small* **2006**, *2* (10), 1159–1163.

(227) Zhang, Y.; Tu, L.; Zeng, Q.; Kong, X. *Chinese Sci. Bull.* **2013**, *58* (21), 2616–2621.

(228) Mattoussi, H.; Mauro, J. M.; Goldman, E. R.; Anderson, G. P.; Sundar, V. C.; Mikulec, F. V; Bawendi, M. G. *J. Am. Chem. Soc.* **2000**, *122* (49), 12142–12150.

(229) Sandros, M. G.; Gao, D.; Gokdemir, C.; Benson, D. E. *Chem. Commun.* **2005**, 2832–2834.

(230) Pinaud, F.; King, D.; Moore, H.-P.; Weiss, S. *J. Am. Chem. Soc.* **2004**, *126* (19), 6115–6123.

(231) Zeng, T.; Hu, Y.; Wang, N.; Xia, C.; Li, S.; Zu, Y.; Liu, L.; Yao, Z.; Zhao, Y.; Wu, H.-C. *Phys. Chem. Chem. Phys.* **2013**, *15* (42), 18710–18715.

(232) Wardeska, J. G.; Viglione, B.; Chasteen, N. D. *J. Biol. Chem.* **1986**, *261*, 6677–6683.

(233) Cargnello, M.; Diroll, B. T.; Gaulding, E. A.; Murray, C. B. *Adv. Mater.* **2014**, *26* (15), 2419–2423.